

MICROTECHNOLOGIES FOR DISCHARGE-BASED SENSORS

by

Xin Luo

A dissertation submitted in partial fulfillment
of the requirements for the degree of
Doctor of Philosophy
(Mechanical Engineering)
in the University of Michigan

2015

Doctoral Committee:

Professor Yogesh B. Gianchandani, Chair
Professor Katsuo Kurabayashi
Professor Mark Kushner
Assistant Research Scientist Tao Li

© Xin Luo 2015

ACKNOWLEDGEMENTS

First of all, I would like to thank my family. My father Shilin Luo and my mother Liuyan Tian, they have supported me throughout my life and always believed in me. With full freedom given by them, I can always make important decisions by myself. I hope they are proud of me. My older sister, Xuan Luo, has influenced me in many ways. I have learned so much from her. I am eternally grateful to them for love and support.

I would like to thank and express my deepest gratitude to my research advisor, professor Yogesh B. Gianchandani. He has dedicated countless hours to guiding our research. His expertise and vision have always made my research efficient. I have benefited a lot from his professionalism, leadership and patience. I would also like to thank my committee members, Prof. Mark Kushner, Prof. Katsuo Kurabayashi, and Dr. Tao Li, for their guidance and important feedback.

I would like to thank my collaborators Dr. Christine Eun, Dr. Jun-Chieh (Jerry) Wang and Dr. Zhongmin Xiong. Christine collaborated with me a in the study of the first generation of microdischarge-based pressure sensors. Jerry and Dr. Xiong collaborated with me on the plasma modeling.

Next, I acknowledge LNF facilities and staff. Without great equipment and organized management, I would not complete my thesis work on time. LNF staff have trained me a lot and provided precious suggestions during my work in cleanroom.

I would also like to thank all my group members, lab mates, and office mates at the University of Michigan, and all my friends in Ann Arbor. They have helped me on my research and made my time at Michigan enjoyable. Erwin brought me to a healthy lifestyle and made me enjoy workout. Jun Tang, my close friend, accompanied me to the gym almost everyday and shared many happy moments in the past few years. Seow Yuen introduced me many new friends, great places to eat and exciting activities to try. I have enjoyed all our time together.

I am grateful to all of you.

TABLE OF CONTENTS

ACKNOWLEDGEMENTS	ii
LIST OF FIGURES	vi
LIST OF TABLES	xii
LIST OF APPENDICES	xiii
ABSTRACT	xiv
CHAPTER 1: Introduction	1
1.1. Motivation	1
1.2. Background	3
1.2.1. Gas Discharge	3
1.2.2. Microdischarges	6
1.2.3. Modified Paschen's Curve	7
1.2.4. Microdischarge-Based Sensors	10
1.3. Microdischarge-Based Pressure Sensors	11
1.4. Microfabricated High Voltage Generator for Microdischarge Initiation	15
1.4.1. Energy Scavenging Using Piezoelectric Materials	15
1.4.2. Nonlinear Piezoelectric Effect	18
1.5. Focus of This Work	20
1.6. Organization of Thesis	22
CHAPTER 2: First Generation Microdischarge-Based Pressure Sensor: Two-Wafer Process with Through-Glass Lead Transfer	24
2.1. Concept and Design	25
2.2. Fabrication	29
2.2.1. Glass Processing	31
2.2.2. Silicon Processing	34
2.2.3. Eutectic Bonding	35
2.3. Experimental Results	36
2.4. Discussion	40
2.5. Conclusions	40
CHAPTER 3: Second Generation Microdischarge-Based Pressure Sensor: Single Wafer, Surface Micromachined Process with Through-Silicon Lead Transfer	42

3.1. Concept and Design	43
3.2. Fabrication	47
3.3. Experimental Results	52
3.4. Discussion	57
3.5. Conclusions	58
CHAPTER 4: A Pulsed High Voltage Generator for Microdischarge Initiation	59
4.1. Design Modeling and Fabrication	60
4.1.1. Design and Configuration	60
4.1.2. Theory and Modeling	62
4.1.3. Fabrication and Assembly	66
4.2. Experimental Results	67
4.2.1. Experimental Setup	67
4.2.2. Experiments on HV Generator	69
4.2.3. Non-Linearity of the Effective Piezoelectric Coefficient	71
4.2.4. Demonstration of Microdischarge Initiation	73
4.3. Discussion	74
4.4. Conclusions	76
CHAPTER 5: Conclusions and Future Work	77
5.1. Summary	77
5.1.1. Microdischarge-Based Pressure Sensor	77
5.1.2. Pulsed High Voltage Generator	80
5.1.3. Microdischarge-Based Chemical Sensor in Gas Chromatography	81
5.1.4. A 100- μm Diameter Capacitive Pressure Sensor	81
5.2. Contributions	82
5.3. Future Work	83
APPENDICES	87
REFERENCES	149

LIST OF FIGURES

- Figure 1.1: Paschen's curves for various fill-gases, which illustrate the relationship between operating voltage and $p \cdot d$ product, where p is the pressure and d is the interelectrode spacing. Discharge electrodes are Ni. The original data in this plot were reported in [Lie05]. 5
- Figure 1.2: Glow discharge at low pressure [Wik09]. 6
- Figure 1.3: Breakdown voltage results in air at atmospheric pressure against interelectrode spacing for Ni electrodes [Dha00]. CIGRE (International Conference on Large High Voltage Electric Systems) data were extrapolated in the region with small spacings based on traditional Paschen's curve. [Dha00] data were from experiments, indicating a modified Paschen's curve with four regions. Deviations from Paschen's curve are shown in Regions A, B and C, with the interelectrode spacings below $\approx 10 \mu\text{m}$. 9
- Figure 1.4: Comparison of active sensing area, readout complexity and temperature dependence of different pressure sensing approaches. 12
- Figure 1.5: Schematic of (a) a bulk foil sensor with electrodes above a quartz chip, illustrating placement, and the microdischarge chamber during operation, and (b) a planar sensor with microdischarge [Wri09a]. 14
- Figure 1.6: (a) Schematic of device contained within a commercial Kyocera package. (b) Diagram of a microdischarge between a single anode and two cathodes [Wri13]. 15
- Figure 1.7: Examples of past work on increasing output voltage for (a) sensing accelerometer [Kob10] and (b) energy scavenging devices [Zha12], by connecting individual PZT element in-series. 17
- Figure 1.8: Comparison of output voltage and voltage density of different energy scavenging devices. 18
- Figure 1.9: The longitudinal piezoelectric d_{33} coefficient and the amplitude of charge density Q_0 as a function of the amplitude of ac pressure for the PZT (63/37) sample doped with 4% at Nb. The dc bias pressure is 15 MPa [Dam97b]. 19
- Figure 2.1: Concept of the microdischarge based pressure sensor. (a) 3D model of the pressure sensor. (b) S-S₀ view of the structure. I_1 and I_2 are discharge currents from two discharge paths. 26
- Figure 2.2: Simulation results of diaphragm deflection at cathode 2 and maximum induced stress for a 2 μm , 5 μm , and 10 μm thick Si diaphragms. 28

Figure 2.3: Process sequence for the glass wafer. 1) Through-holes are laser drilled. 2) Glass wafer is attached to a dummy Si wafer by eutectic bonding. A 4–6 μm thick electroplated indium layer on the dummy wafer serves as the seed layer for Cu electroplating. 3) Through-holes are filled by Cu electroplating. 4) A lapping step removes excess Cu and the dummy wafer. 5) The contact pads are deposited and patterned on the exterior of the glass wafer. 6) The bond ring and *K2* contact are defined on the interior side of the glass wafer. The In bond ring is covered with 50 nm Au for protection. 7) Electrodes are deposited on the interior of the glass wafer. 30

Figure 2.4: Process sequence for the Si wafer. 1) Silicon dioxide layer is grown and patterned on SOI for diaphragm insulation, and *K2* contact is then defined. 2) Au bond ring and *K2* contact on the interior of SOI wafer are electroplated. *K2* electrode is deposited by a lift-off process. 3) Eutectic bonding is performed between glass and silicon wafers. 4) Handle wafer is released by a backside dry etching. 31

Figure 2.5: Optical photos of fabricated glass chip. (a) Laser drilled TGVs, out-chamber side. (b) TGVs are electroplated with copper; bond ring and *K2* contact are patterned with indium and Au protection. (c) Zoom-in view of the microdischarge chamber. (d) Anode and cathode *I* are patterned with Ti/Ni as electrodes by a lift-off process. 33

Figure 2.6: Chip level eutectic bonding of Au-In bond rings. (a) Glass and silicon chips, before and (b) after bonding, against a U.S. penny ($\text{\O}19.05$ mm). (c) Zoom-in view of one bonded ring, viewed through glass. (d) SEM image of the cross-section of the Au-In bond ring. (e) SEM details of the bond structure. (f) Electron dispersive spectroscopy shows the diffusion of the Au and In components and the resulting Au and In intermetallic compounds that have formed. 35

Figure 2.7: Photograph of the final assembly of the glass and silicon chips, viewed from the exterior of the glass. 37

Figure 2.8: Test setup for the glass and Si chip assembly. A micromanipulator applies force at the center of the 100 μm -thick Si diaphragm to deflect the Si chip and change the *AK2* spacing. 37

Figure 2.9: Representative waveforms of the microdischarges collected at the cathodes obtained from an oscilloscope during the tests. 38

Figure 2.10: Differential currents from test results versus estimated equivalent pressure and inter-electrode gap from simulation results based on a 5 μm thick Si diaphragm. *I1* and *I2* are peak values of envelope curves for *AK1* and *AK2* discharge waveforms, respectively. Tests are in Ar with the microdischarge chamber interior pressure between 650 Torr and 770 Torr. Applied voltage pulses are 480 V to 580 V. Ballast resistors are 10 M Ω and 20 M Ω . Every point is the average of 5–8 measurements. Error bars indicate one standard error. 38

Figure 3.1: Schematics of the microdischarge-base pressure sensor. (a) A 3-D view with dimensions labeled. (b) A cross section view illustrating two plasma current paths inside the cavity, the configuration of multiple anodes and single cathode, and through-wafer isolated bulk-silicon lead transfer (TWIST) with backside contacts. (c) A top view showing the plasma localization feature. 44

Figure 3.2: Finite element analysis of diaphragm deflection and maximum von Mises stress with selected dimensions in response to external pressure. In this simplified FEA, contact pressure for a 3 μm cavity height is ≈ 2.7 MPa. 47

Figure 3.3: Fabrication process. (a) Heavily doped silicon wafer is etched by DRIE to define individual isolated region. (b) Etched trenches are filled by thermal oxidation and TEOS deposition. (c) Wafer is double-side lapped and polished, followed by PEDVD oxide on both sides. (d) Metal contact vias are patterned on PECVD oxide layers by RIE, followed by metal deposition using sputtering and liftoff. (e) Amorphous silicon is deposited and patterned as a cavity sacrificial layer, followed by another metal layer deposition and the first diaphragm layer oxide/nitride/oxide (ONO) deposition. (f) Amorphous silicon is etched by gaseous XeF_2 . (g) Etchant access slots are sealed by a PECVD silicon nitride layer and an atomic layer deposition (ALD) Al_2O_3 layer. 48

Figure 3.4: Selected fabrication results: (a) Top view of a device after bottom Ti/Ni electrode deposition. (b) Top view of a device after pattern of α -Si sacrificial layer and top Ni/Al electrode. (c) Back view of a final device with Ti/Al contact pads. (d) Top view of a final device. 49

Figure 3.5: SEM images of (a) fully filled silicon trenches with details of trench top and (b) bottom, (c) cross section of a fabricated device and (d) enlarged details, (e) a sealed etchant access slot, (f) a fabricated device. 51

Figure 3.6: Schematic of the Ar sealing strategy. After the microfabrication, the narrow Ar filling channel is opened, and then the device is placed in a pressure controlled chamber. The chamber is first pumped to vacuum, followed by filling with Ar at ≈ 700 Torr. A micromanipulator is used to control the probe to apply epoxy at the channel opening. 52

Figure 3.7: Experimental setup. (a) Device under test (DUT) is surface mounted to a prototype board, which is soldered on a connector. The connector is inserted in a customized stainless steel pressure chamber, which is connected to a gas tank with a reference gauge. (b) Test circuit. Negative voltage pulses (3 ms) are applied on the device through a ballast resistor. Microdischarge current I_1 and I_2 are read out through pick up resistor R_1 and R_2 using oscilloscope probes. 53

Figure 3.8: Typical profiles of microdischarges (a) at low pressure (1 atm) with DC-like discharge current, and (b) at high pressure (5 atm) with pulsed discharge current. Breakdown voltages were 250 V. The red line denotes applied voltage, yellow is I_1 and violet is I_2 . 54

Figure 3.9: Pressure response of the DUT: normalized differential current and the corresponding calculated plasma impedance against the external pressure from 1 to 8 atm. Breakdown voltages were 250 ± 50 V. Every data point was an average of 10–20 microdischarge readings. Errors bar indicate one standard deviation. 55

Figure 3.10: Typical profile of the low intensity steady current I_2 at high pressure, while I_1 was zero. Voltage pulses (3 ms) at 250 V were applied. The red line denotes applied voltage, yellow is I_1 and violet is I_2 . 56

- Figure 3.11: Low intensity steady current I_2 and calculated plasma impedance with external pressure from 5 to 8 atm. Voltage pulses (3 ms) at 250 V were applied. 56
- Figure 4.1: Schematic diagram of the HV generator and its circuit model, including a monolithic PZT disk with three series-connected electrode pairs through a flexible polyimide cable. The HV generator is analyzed using a series-connected capacitor model. 61
- Figure 4.2: Simulation in COMSOL Multiphysics[®] 4.3. (a) Uniform pressure of 5 MPa is applied on a $\varnothing 5$ mm, 740 μm thick PZT disk. Series-connected electrodes are set as equipotential. (b) Electric potential distribution. 62
- Figure 4.3: Schematic illustration of two cases of fringe capacitance. Electrodes 2 and 2' are shorted together. The arrows indicate electric fields in charged fringe capacitors. 65
- Figure 4.4: Illustration of two types of fringe capacitance that exist in the HV generator. 65
- Figure 4.5: Fabrication and assembly process. Both sides of PZT51 disks are patterned with Cr/Au electrodes. The patterned PZT disks are then sandwiched by customized flexible polyimide cables, and bonded using both superglue and silver epoxy. 66
- Figure 4.6: The assembled HV generator against a U.S. penny of 19.05 mm diameter. 67
- Figure 4.7: Experimental setup. (a) Transient load is applied by dropping a stainless steel ball (OD 6.8 mm) guided by a glass tube. (b) Resistor divider readout circuits. C_d and C_p are the capacitance of the HV generator and the oscilloscope probe, respectively. 68
- Figure 4.8: Simulation in NI Multisim[™] of the ratio of the measured voltage to the real value as a function of the voltage division. 69
- Figure 4.9: Experimental results of the measured output voltage as a function of the applied mechanical stress from single-electrode pair device and three-electrode pair device. Voltage amplification provided by the output voltage ratio of the three-electrode pair to single-electrode pair devices determined by equations fitted to experimental data. 70
- Figure 4.10: Effective piezoelectric coefficient, d'_{33} , for the single-electrode pair device and the three-electrode pair device. Data points are calculated based on experimental results shown in Figure 4.9 and Eq. (4.2). Linear fittings are based on Eq. (4.6)–(4.8). 72
- Figure 4.11: Demonstration experiment setup and results. (a) Experimental setup for testing the HV generator on a microdischarge based chemical vapor sensor. (b) Electrodes details of the microdischarge chemical vapor sensor, before discharge. (c) Discharge moment of the chemical vapor sensor. 74
- Figure 4.12: Measured transient voltage response across a 19.8 k Ω resistor during the discharge. 74
- Figure 5.1: Parametric study for dimensional selection using finite element analysis. 84

Figure 5.2: Maximum stress and diaphragm deflection under applied external pressure for selected parameters. Different safety margins are highlighted.	85
Figure 5.3: Schematic of the proposed design with further reduction in device volume, targeting a pressure range up to 50 MPa.	85
Figure A.1: One example of the optical emission spectroscopy from microdischarges for chemical vapor sensing using pulsed DC microdischarge. (a) Schematic of the sensor and experimental setup. (b) A typical spectrum obtained in an acetone environment, readout from the spectrometer [Mit08b].	89
Figure A.2: The assembled chemical detector with a glass lid and inlet/outlet capillary tubes, against with a U.S. penny.	91
Figure A.3: Schematic of the sensing system.	92
Figure A.4: A typical spectrum obtained when the acetone passed by the detector.	93
Figure A.5: Chromatograms obtained from the microdischarge response, and compared with the results from reference FID.	93
Figure B.1: A schematic of the capacitive pressure sensor. (a) 3-D view of the sensor, with dimensions labeled. (b) A cross section view of the sensor.	100
Figure B.2: Schematic diagrams of the FEA model, dimensions are not to scale. (a) Initial state. (b) With external pressure P applied, the diaphragm contacts the substrate, and a distributed contact force is added to simulate contact-mode operation.	102
Figure B.3: Modeling results of $C100t3$: Impacts of individual parameter variation on capacitive response to external pressure from finite element analysis in COMSOL. (a) Impact of diaphragm thickness variation. (b) Impact of diaphragm diameter variation. (c) Impact of cavity height variation. (d) Impact of diaphragm Young's modulus variation.	103
Figure B.4: Modeling results of $C100t5$: Impacts of individual parameter variation on capacitive response to external pressure from finite element analysis in COMSOL. (a) Impact of diaphragm thickness variation. (b) Impact of diaphragm diameter variation. (c) Impact of cavity height variation. (d) Impact of diaphragm Young's modulus variation.	104
Figure B.5: Impacts of residual stress of nitride diaphragm on capacitive response and maximum von Mises stress under 20 MPa external pressure from finite element analysis of $C100t3$.	105
Figure B.6: Simulated impact of coupled parameter variations on capacitance change for 20 MPa applied pressure on $C100t3$. Contours indicate discrete values of capacitance change obtained	85

from changes of (a) diaphragm diameter and diaphragm thickness, and (b) Young's modulus of diaphragm material and diaphragm thickness. 106

Figure B.7: Fabrication process. (a) Heavily doped silicon wafer is etched by DRIE to define individual isolated region. (b) Etched trenches are filled by thermal oxidation and TEOS deposition. (c) Wafer is double-side lapped and polished, followed by PECVD oxide on both sides. (d) Metal contact vias are patterned on PECVD oxide layers by RIE, followed by metal deposition using sputtering and liftoff. (e) Amorphous silicon is deposited and patterned as a cavity sacrificial layer, followed by another metal layer deposition and the first diaphragm layer oxide/nitride/oxide (ONO) deposition. (f) Amorphous silicon is etched by gaseous XeF_2 , followed by atomic layer deposition (ALD) of Al_2O_3 . (g) Etchant access slots are sealed by a PECVD silicon nitride layer and another ALD Al_2O_3 layer. 108

Figure B.8: Selected fabrication results: (a) Top view of a device after bottom Ti/Ni electrode deposition. (b) Top view of a test structure utilized to monitor the XeF_2 etch, since the top electrode of real devices blocks the view of etching process. (c) Top (front) view of a final device. (d) Back view of a final device with Ti/Al contact pads. 109

Figure B.9: SEM images of (a) fully filled silicon trenches, (b) details of the *C100t5* cross section, (c) a sealed etchant access slot and (d) a fabricated *C100t5* device. 110

Figure B.10: Experimental setup. The device under test (DUT) and a thermocouple are soldered to a connector, which is inserted into a customized stainless steel pressure chamber. The chamber can be heated using an external heating tape. Pressure is applied by a manual hydraulic pump and measured by a reference pressure gauge. The DUT is read by an LCR meter. 111

Figure B.11: Typical pressure responses measured at room temperature (25°C) for (a) *C100t3* devices and (b) *C100t5* devices. The total capacitance changes are about 140 fF for *C100t3* at 20 MPa, and 110 fF at 50 MPa for *C100t5*. Each data point represents an average of ≈ 30 readings taken over three pressure cycles. Error bars are not visible at this scale. 113

Figure B.12: Typical pressure responses for *C100t3* devices in the non-contact region over temperature. 114

Figure D.1: Process characterization of the residual stress in PECVD α -Si. 141

Figure D.2: Sidewall profiles of α -Si layer after RIE. (a) Initial profile with an anisotropic etching by Pegasus. (b) A more isotropic profile, using the customized RIE. 142

Figure D.3: Residual stress of PECVD nitride film against the flow rate ratio of SiH_4 to NH_3 . Data points with no error bars indicate only one experiment was performed. The other data points are averaged values from ≈ 5 experiments. The deposition temperature was 380°C unless noted otherwise. 144

Figure D.4: (a) Undercut at one side, and (b) PR sidewall angle and width of $3\ \mu\text{m}$ open features with increasing the does of first exposure. 148

LIST OF TABLES

Table 4.1: Comparison of different circuit models considering fringe capacitance.	65
Table 5.1: Further FEA parametric study results, selected dimensional design is highlighted.	85
Table B.1: Parameters used in the simulation. Nominal values are used unless noted otherwise.	102
Table B.2: Impact of selected diaphragm thickness variation on sensitivity for <i>C100t3</i> and <i>C100t5</i> based on FEA results.	105
Table B.3: Sensitivities for <i>C100t3</i> and <i>C100t5</i> in non-contact and contact regions from experimental data.	112
Table B.4: Thermal expansion coefficients of materials used in the device.	116
Table C.1: A brief summary of the process steps for the second generation microdischarge-based pressure sensor.	122
Table C.2: Table of parameters ramping in customized recipe 1 for DRIE.	125
Table D.1: Experiments in characterization of PECVD nitride film stress.	145
Table D.2: Process steps of IR lithography characterization.	146
Table D.3: Characterization results of IR lithography from grating features with dimensions from 1 μm to 3 μm .	147

LIST OF APPENDICES

Appendix A: An Application of A Microdischarge-Based Chemical Sensor in Gas Chromatography	88
Appendix B: A 100- μm Diameter Capacitive Pressure Sensor with 50 MPa Dynamic Range	95
Appendix C: Run Sheet of the Second Generation Microdischarge-Based Pressure Sensors	122
Appendix D: Process Characterization	140

ABSTRACT

Microdischarge-based sensors are known to offer advantages such as the ability to operate at temperature extremes and to provide large output signals that do not require local amplification. This work is primarily directed at the design and microfabrication of pressure sensors that use differential microdischarge currents. Two approaches are evaluated. The first uses a common anode and reference cathode located on a glass substrate, whereas a sensing cathode is located on an opposing silicon diaphragm that is deflected by applied pressure. Leads are transferred by electroplated through-glass vias. The second uses a common cathode and reference anode located on a silicon substrate, whereas a sensing anode is located on a thin film diaphragm that deflects under applied pressure. Leads are transferred by through-wafer isolated bulk-silicon lead transfer (TWIST). Fabricated sensors with 200- μm diameter have footprints as small as $300 \times 300 \mu\text{m}^2$, and volume of $\approx 0.01 \text{ mm}^3$, which is $150\times$ smaller than prior work. The fractional differential current $(I_1 - I_2)/(I_1 + I_2)$ increases monotonically from -0.7 to 0.2 as external pressure increases from 1 atm to 8 atm.

The TWIST process can also be used to fabricate ultra-miniature capacitive pressure sensors with backside contacts that minimize the form factor and allow stacking of the sensor on interface electronics. A sensor with a 100- μm diameter diaphragm measures $150 \times 150 \mu\text{m}^2$ in size. Fabricated sensors with thicknesses of 3 μm (*C100t3*) and 5 μm (*C100t5*) have dynamic ranges of 20 MPa and 50 MPa, respectively. Pressure responses in the non-contact mode and the

contact mode are 3.1 fF/MPa, 5.3 fF/MPa for *C100t3*, and 1.6 fF/MPa, 1.6 fF/Ma for *C100t5*, respectively.

This thesis also describes a preliminary exploration of options to initiate microdischarges using scavenged energy – in this case from mechanical impact. A miniature high voltage generator is formed by connecting multiple electrode pairs in series on a single PZT element. This strategy amplifies voltage roughly in proportion to the electrode pair count; a three electrode-pair device is used to successfully initiate microdischarges with peak voltages exceeding 1.35 kV.

CHAPTER 1:

Introduction

1.1. Motivation

The sensing of environmental variables such as pressure, temperature, and chemical content in a variety of harsh environments is both necessary and challenging. For example, in borehole environment during the extraction of petroleum or natural gas, the temperature could be hundreds of degree Celsius and the pressure during the hydraulic fracturing could reach as high as 50–100 MPa [Hua11, Shi11]. Moreover, rock fracturing induced shock, both temperature and pressure fluctuation bring more challenges for the sensor operation. Conventional sensing methods are limited by form factor, temperature coefficients, dynamic range, and the need for local electronics. Consequently, there is a strong motivation to investigate new alternatives.

Whereas a number of microsensors utilize piezoresistive, capacitive, and other well-established transduction approaches, in recent years there has been rising interest in using electrical microdischarges (such as microplasmas and microarcs) to generate the sensor output. Sensors incorporating microdischarges are well suited for high temperature operation as electron temperatures are typically many eV ($1 \text{ eV} = 11,600 \text{ K}$) and so are not significantly perturbed by a high ambient temperature [Wil03, Kus05]. Further, the inherent signals of microdischarges, including both electrical current and optical emission, are relatively large compared to other sensing principles. Thus, microdischarge-based sensors have good capabilities of volume

scaling to meet increasing requirements of smaller sensor dimensions, such as fitting in cracks of oil wells with feature size of a few millimeters.

In order to effectively utilize microdischarges, however, a number of challenges must be addressed, ranging from device and package design, to the interface circuits, and the power supply.

While recognizing that microdischarges can be used in a variety of sensing applications, this thesis focuses primarily on pressure sensing. This is because microfabricated pressure sensors are widely used in automotive systems, healthcare, consumer applications, and petrochemical and oil industry. With sales worth of \$2.1 billion, microfabricated pressure sensors represent one of the largest segments of the entire industry of microelectromechanical systems (MEMS) with a total sales of \$12 billion in 2013 [Yol14]. The investigation of microdischarge-based pressure sensors will expand the understanding and enhance the performance of pressure sensing in harsh environments.

The thesis also describes a preliminary exploration of options to initiate microdischarges using scavenged energy – in this case from mechanical impact. This is motivated by the high-voltage requirements of microdischarge-based sensors and the possible problems of battery usage in harsh environments. In fact, there is ample mechanical energy that could potentially be utilized in harsh environments, such as high pressure, high fluctuation and high flow fracturing liquid, acoustic vibration during the rock fracturing and so on.

Motivated by those needs, this work will explore two aspects of microtechnologies for discharge-based sensors: (i) device design and microfabrication options for microdischarge-based pressure sensors, and (ii) voltage boosting options for initiating microdischarges using scavenged energy.

1.2. Background

1.2.1. Gas Discharge

Gas discharge describes the flow of electric current through a gaseous medium. It is required that gas particles are ionized by applying high electric field. In this dissertation, ionized gas particles are generated by electrical discharge with high electric field between metal electrodes. Normally, the gas ionization process is described by Townsend discharge or Townsend avalanche. The avalanche is a cascade reaction involving electrons in a gaseous medium with high electric field. When an initial ionization occurs, positive ions drift to the cathode and negative electrons drift toward the anode driven by the electric field. If the electric field is strong enough, electrons gain sufficient energy and liberate more electrons from neutral gas molecules due to collisions. Original electrons together with newly generated electrons keep drifting and gaining energy from electrical field, and then the next collision and ionization will occur again. This process is effectively a chain reaction of electron generation, which leads to an avalanche.

In the steady state, DC gas discharges are classified in three categories according to the current they carry [How76]:

- (i) The Townsend or dark discharge, with current density up to 10^{-6} A/cm².
- (ii) The glow discharge, with current density from 10^{-6} to 10^{-1} A/cm².
- (iii) The arc discharge, with current density larger than 10^{-1} A/cm².

The Townsend discharge has very limited current so that there is no visible emission light from the discharge. In fact, no “breakdown” really happens in the gaseous medium, although the current flow can be measured. The Townsend discharge is not self-sustaining and it requires

external sources to supply electrons either in the gas or from the cathode. The external agencies include ultraviolet light, X-rays or cosmic rays.

Increasing the voltage applied across the discharge electrodes, the Townsend discharge current will increase correspondingly. When the voltage reaches “breakdown” point, the current sharply increases by several orders of magnitude. After breakdown, the discharge becomes self-sustaining and takes the form of a glow or an arc discharge, depending on the gas and external circuit conditions. For both cases, the discharge is luminous and can be used for lighting and emission spectroscopy applications that will be discussed later. In a glow discharge, the discharge is sustained mainly by the electrons from secondary emission caused by the bombardment of the cathode by positive ions. In an arc discharge, the large current is maintained from sources including thermionic emission from the cathodes.

The breakdown voltage is related to multiple factors, including the type of gases, electrode materials, gas pressure, interelectrode spacing, etc. For plane-parallel electrodes, the breakdown voltage is given by the Paschen’s curve (Figure 1.1) [Lie05]:

$$V_b = \frac{Bpd}{\ln Apd - \ln[\ln(1 + 1/\gamma_{se})]} \quad (1.1)$$

Here p is the fill-gas pressure; d is the effective length of the breakdown path, approximated by the spacing between the electrodes. A ($\text{cm}^{-1}\text{Torr}^{-1}$) and B ($\text{V}\cdot\text{cm}^{-1}\text{Torr}^{-1}$) are parameters obtained by fitting the first Townsend coefficient, α (cm^{-1}) as a function of E/p (Electric field/gas pressure), $\alpha=A\cdot p\cdot\exp(-(E/p)/B\cdot p)$. The first Townsend coefficient expresses the number of ion pairs generated per unit length by a negative ion moving from cathode to anode. A and B depend on the type of gas but not on the metal of the electrodes. The parameter γ_{se} is the secondary electron emission coefficient by ion bombardment, which depends on the metal selected for the

electrodes and the gas. A larger γ_{se} lowers the breakdown voltage. For each choice of fill-gas in the microdischarge chamber, there is a $p \cdot d$ product that corresponds to a minimum voltage for discharge initiation. Operating the device near the minimum of Paschen's curve also has the additional benefit that the energy dissipated by the discharge is reduced. This assumes that the ballast resistor does not change.

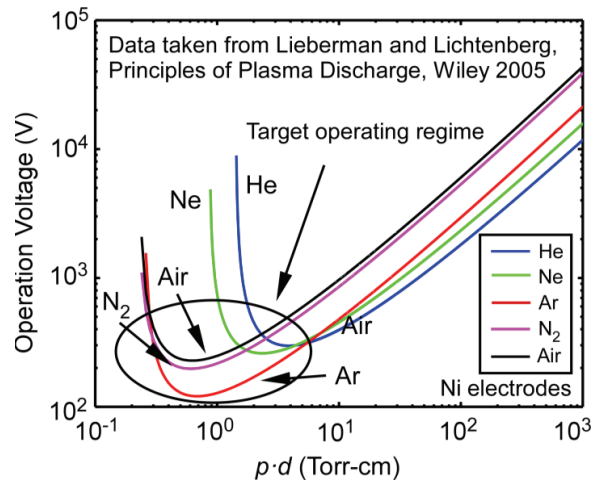


Figure 1.1: Paschen's curves for various fill-gases, which illustrate the relationship between operating voltage and $p \cdot d$ product, where p is the pressure and d is the interelectrode spacing. Discharge electrodes are Ni. The original data in this plot were reported in [Lie05].

When the pressure is low, less than a few Torr, a glow discharge more likely happens once breakdown has occurred. Afterwards, the gas emits a diffuse glow of characteristic color with several distinct regions (Figure 1.2). The flow current is about a few milliamps and the potential difference does not change a lot compared to the point at which the breakdown takes places. However, when the pressure is increased to atmospheric level, and if the resistance of the external circuit is comparatively low, the discharge will preferentially take the form of an arc discharge. The large current is determined by the external circuit, and the voltage across the discharge is relatively low, around tens of volts. In this sense, the self-sustained discharge is

unstable at higher pressures around atmospheric pressure, and tends to become an arc form, which limits their practical utility.

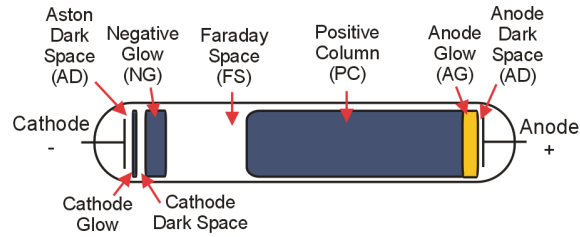


Figure 1.2: Glow discharge at low pressure [Wik09].

1.2.2. Microdischarges

For a long time, it was believed that stable discharges could only exist in low pressure gases. Nowadays, people also find stable discharges in high pressure conditions, although the volume of discharges is restricted. An attractive form for discharges stays stable in high pressure is “microdischarge”. Microdischarge is a miniaturized discharge or plasma that has different characteristics from macroscopic discharges due to its small feature size (electrodes spacing is less than 1 mm) [Kus05, Foe06]. The microdischarge current is sustained by secondary electron emission from the cathode mainly due to ion bombardment, and the plasma-surface interactions become increasingly important due to the increase of surface to volume ratio. The large surface to volume ratio leads to high losses of charge carriers to surrounding walls, which in turn contributes to plasma stability at higher pressures. Microdischarges can operate as glow discharges on a continuous basis at pressures approaching and exceeding atmospheric pressure even with large current density and power deposition. Due to the large current density and power deposition, gas heating and flow dynamics are important considerations for microdischarge-based devices. For example, these dynamics can affect the visible and UV

emission characteristics of microdischarge, which is the basis of microdischarge-based chemical sensors using optical emission spectroscopy [Wil02, Kar04, Mit08a]. The term “discharge” and “plasma” are often interchangeable in the low temperature plasma community, because electrical discharges are the most widely used way to generate low-temperature, non-equilibrium plasmas [Foe 06].

From the Paschen’s curve in Figure 1.1, when the pressure is around atmospheric pressure, the breakdown voltage is required at tens of thousands of volts for macroscopic discharge devices whose interelectrode spacing is typically from several centimeters to tens of centimeters. With such a high voltage applied, once the breakdown occurs, the current will be sharply increased and make the discharge process unstable. However, for a microdischarge, due to the small feature size, the $p \cdot d$ product can be tuned at where the breakdown voltage is much reduced or at its minimal region. The lower breakdown voltage not only makes the discharges happen easily, but also ensures that the discharge is stable with a small current after breakdown. Devices using microdischarge, instead of its macroscopic counterpart, also benefit from lower power consumption, smaller volume, and easy integration for portable systems.

1.2.3. Modified Paschen’s Curve

The traditional Paschen’s curve is derived based on the Townsend electron avalanche theory described in Section 1.2.1. The charge generation processes include electron impact ionization (the α process) and secondary electron emission from the cathode (the γ process) which is primarily due to ion bombardment; other bombardment processes may also exist [Tow15, Go10]. However, this simplified explanation fails to describe the situation with

extremely large or small $p \cdot d$ products [Nas71, Go10], especially for very small interelectrode spacings ($<10 \mu\text{m}$) in air at atmospheric pressure.

Many recent studies, including experimental, theoretical, and computational investigations, show that the breakdown voltage deviates from the traditional Paschen's curve and follows the so-called *modified Paschen's curve* when the interelectrode spacing is smaller than about $10 \mu\text{m}$ [Dha00, Sla02, Wal03, Hou06, Go10]. The modified Paschen's curve indicates that the breakdown voltage continues to decrease nearly linearly with the decreasing interelectrode spacing at atmospheric pressure in air (Figure 1.3). In Figure 1.3, deviations from Paschen's curve occur in the regions of $A-C$, while Paschen's curve still holds in the region D . Breakdown voltage rapidly falls off in region A and B , when the interelectrode gap reduces. The electrical fields range from $5 \times 10^7 \text{ V/m}$ to 10^8 V/m . With high electric fields ($\sim 10^8 \text{ V/m}$), electrons can tunnel through the potential barrier at the cathode surface, which is called field emission. In the modified regions, the electron field emission plays a critical role in the electric breakdown. An exact linear relation was measured in region A ($<1.5 \mu\text{m}$), which was explained quantitatively by considering the quantum tunneling of an electron from the electrode surface [Dha00]. Near-linear behavior in region B ($1.5-4 \mu\text{m}$) was also experimentally observed. A plateau in region C ($4-10 \mu\text{m}$), as many other researchers also have observed, indicates air breakdown at $\approx 400 \text{ V}$ occurs over a path longer than the interelectrode gap [Ger59]. This is probably because the number of ions is insufficient for avalanche phenomena and the electric field strength is moderate at such electrode spacing.

The electron field emission can be increased in two ways, geometric surface enhancement and ion-enhancement. The geometric surface enhancement is primarily related to the electrode geometry, such as protrusions due to surface roughness. A protrusion can

concentrate the electric field at its tip. The enhanced electric field at a micro projection on the cathode surface can be high enough to produce a very high current density, field emission electron beam. When the current density exceeds a threshold, very high-density plasma is then formed. If this plasma reaches the anode, then electrical breakdown between electrodes is achieved [Sla02]. Some researchers find that the geometric surface enhancement is generally insufficient for the breakdown in experiments [Hou06, Go10]. Instead, they believe that ion-enhanced field emission is the primary factor that contributes to the breakdown in microdischarges. The ion-enhanced field emission is similar to the secondary emission from cathode, but it occurs when positive gaseous ions approach the cathode and both lower the potential barrier at the cathode and reduce its thickness. In consequence, it becomes easier for electrons to tunnel through the potential barrier at the cathode, and then the field emission is enhanced. Many other studies indicate that ions can increase the emission current by one to three orders of magnitude [Tes96, Gay96, Spa97, Jos98].

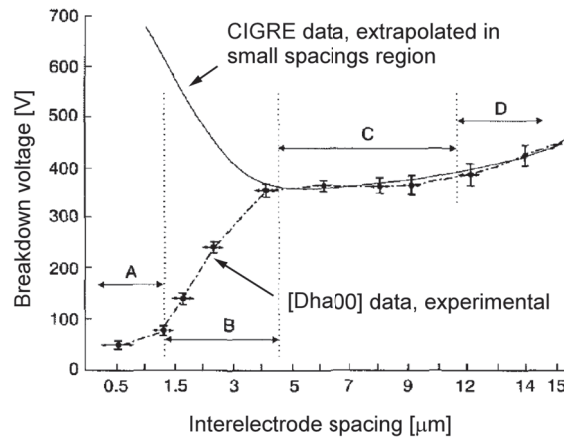


Figure 1.3: Breakdown voltage results in air at atmospheric pressure against interelectrode spacing for Ni electrodes [Dha00]. CIGRE (International Conference on Large High Voltage Electric Systems) data were extrapolated in the region with small spacings based on traditional Paschen's curve. [Dha00] data were from experiments, indicating a modified Paschen's curve with four regions. Deviations from Paschen's curve are shown in Regions A, B and C, with the interelectrode spacings below $\approx 10 \mu\text{m}$.

The investigation of the modified Paschen's curve was originally motivated by the concerns of unintended electric breakdowns in MEMS with continuous miniaturizations of electrical components. However, the reduced breakdown voltage in the region of modified Paschen's curve can be good news for microdischarge-based devices in pursuit of further miniaturization and reduction of power consumption. In fact, the behavior of the microdischarge-based pressure sensor being described in Chapter 3 of this work can be partially explained by the modified Paschen's curve.

1.2.4. Microdischarge-Based Sensors

Microdischarges can be used in a variety of microsensors, including micro total analysis systems that use optical emission spectroscopy for chemical sensing [Wil02, Kar04, Mit08a], radiation detectors, sputter ion pumps, etc. [Eun12]. Microdischarge-based transducers, while not very well understood at present, have many attractive features. For the conditions encountered in these devices, ions have temperatures moderately above ambient with transport coefficients that are also not particularly sensitive to high operating temperatures. (Note that since the plasma is partially ionized, the high temperatures of the electrons and ions represent a small fraction of the total energy content.) The high temperatures of the electrically conducting species make microdischarge-based devices intrinsically immune to harsh environments. In addition, the inherent signal levels are large compared to both capacitive and piezoresistive devices, eliminating the need for a proximal interface circuit – and, in fact, substantially reducing the need for amplification. This is very appealing from the viewpoint of miniaturization.

1.3. Microdischarge-Based Pressure Sensors

A variety of microscale pressure sensing solutions have been explored in the past five decades, of which the most commonly used are piezoresistive and capacitive pressure sensors [Gia06]. Piezoresistive sensors typically measure stress in a diaphragm as it deflects in response to pressure. In contrast, capacitive pressure sensors respond to diaphragm deflection rather than stress. The smallest micromachined pressure sensors that have been reported – e.g., for use within cardiac catheters – use these transduction techniques. For both types of sensors, the side-dimensions of the diaphragms of the smallest devices have been about 1 mm long. Further reduction in size has been a challenge for both approaches, but for different reasons.

For piezoresistive pressure sensors, reducing the diaphragm diameter presents a challenge in localizing the resistor. If the resistor extends too far from the edge toward the center of the diaphragm, it loses signal due to stress averaging: the stress on the upper surface of the diaphragm changes from tensile at the perimeter to compressive at the center, with a null point located in between. Making the resistor smaller is a challenge as well. Smaller resistors demand more current to generate a measurable voltage, and are relatively imprecise, which affects calibration and yield. Resistors inherently have a high temperature sensitivity, which makes this transduction approach less appealing for high temperature applications. Piezoresistive sensors do have relatively low output impedance, which means that the sensing circuit does not have to be located in the immediate proximity of the sensor. The equivalent noise pressure from piezoresistive pressure sensors increases as $1/r^2$, where r is the equivalent radius of the diaphragm.

Capacitive pressure sensors present a scaling challenge because the capacitance decreases in proportion to the area of the diaphragm. This scaling puts the burden of detection on the

interface circuit, which must not only be precise, but must also be located in the immediate vicinity of the sensor in order to prevent the signal – which comes from a high impedance output, and hence is inherently weak – from leaking into parasitic capacitance. Another consequence of the reduced capacitance is the increase in $k_B T/C$ noise, which is a fundamental noise source due to a single electrical degree of freedom associated with a capacitor. Together with other noise sources, the equivalent noise pressure from capacitive pressure sensors increases as $1/r^5$. While capacitive pressure sensors have about $10\times$ lower sensitivity to temperature than piezoresistive devices, the proximal interface circuit must be tolerant of high temperature environments as well.

Approaches to pressure sensing based on microdischarges have recently been reported [Wri09a, Wri13]. This transducing mechanism is less dependent on the temperature and has simple readout circuits due to large inherent signals. Thus, the microdischarge-based pressure sensors have a promising scalability. The comparison of the active sensing area, interface circuit complexity and temperature dependence of different sensing approaches is plotted in Figure 1.4.

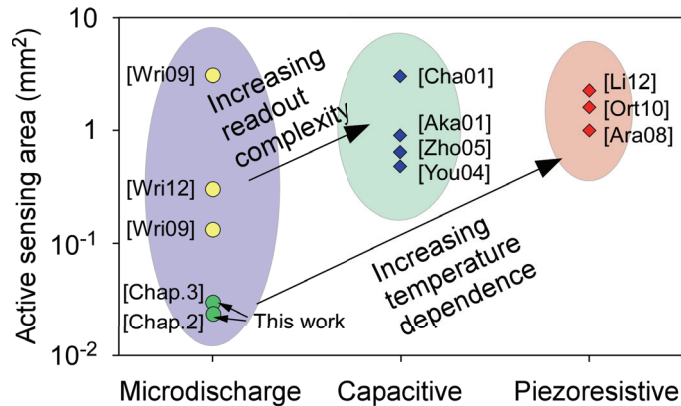


Figure 1.4: Comparison of active sensing area, readout complexity and temperature dependence of different pressure sensing approaches.

In general, these reported microdischarge-based pressure sensors operate by measuring the spatial current distribution of the microdischarge that is related to the pressure changes by the

sensor structures. To achieve the pressure related microdischarge distribution, two sensing mechanisms were studied.

In the first mechanism, the pressure sensor senses the mean free path changes of the ionized molecules, which are related to the surrounding pressure. For this mechanism, there are also two sensor configurations, as shown in Figure 1.5 [Wri09a]. In the bulk foil sensor (Figure 1.5a), one anode and two cathodes are stacked vertically in a trenched quartz substrate. The interelectrode spacings, 50–100 μm , are controlled by the depths of different trenches. The inner cathode is perforated so that discharges are able to have two paths to reach cathodes. When the pressure increases, the mean free paths of the ionized gas molecules reduce, and the discharges favor the short discharge path. Whereas at low pressures, more discharge current goes to the further cathode from the bottom anode. The differential current, *i.e.*, $(I_1 - I_2)/(I_1 + I_2)$, as a sensing output, reflects the pressure level. By using differential measurements, the absolute magnitude becomes less important than the fractional values, which minimizes the impact of energy variation from each measurement. This bulk foil sensor was tested in high temperature environments up to 1000 $^{\circ}\text{C}$, and a pressure range from 10–2000 Torr, showing the capability of operation in high temperature environments for the microdischarge devices. In another configuration, as shown in Figure 1.5b, the electrodes are all patterned on a planer substrate. The basic idea is the same as the bulk foil pressure sensor, also taking advantage of the mean free paths changes of the ionized gas molecules as the pressure changes.

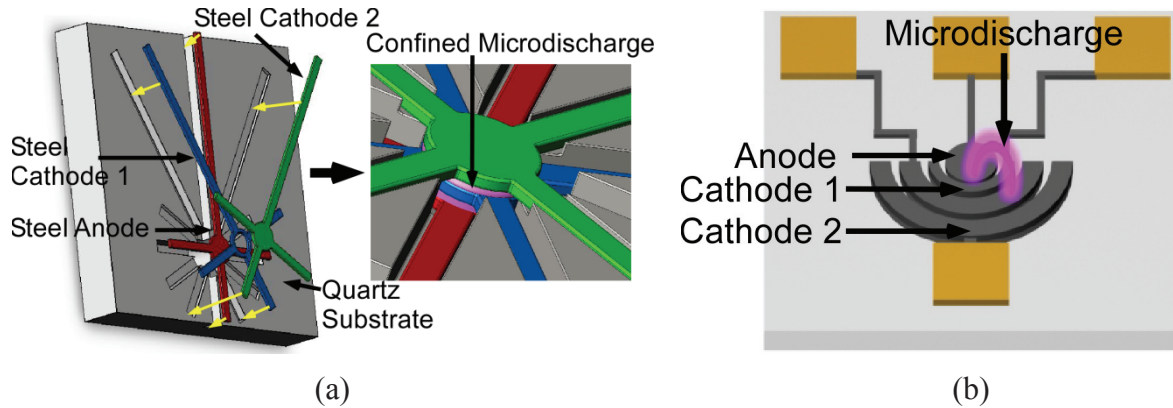


Figure 1.5: Schematic of (a) a bulk foil sensor with electrodes above a quartz chip, illustrating placement, and the microdischarge chamber during operation, and (b) a planar sensor with microdischarge [Wri09a].

In the second sensing mechanism, the change of the spatial discharge current distribution is directly attributed to the change of the physical interelectrode spacings [Wri13]. Figure 1.6 shows the schematic of the structure and operation of this microdischarge-based pressure sensor. This design also utilizes a vertically stacked structure with one anode on the bottom and two cathodes above. Different from the bulk foil pressure sensor, this design has a deflecting diaphragm that also serves as one cathode, and the microdischarge chamber is filled with nitrogen and sealed. The increased external pressure deforms the diaphragm and reduces the spacing between the anode and the diaphragm cathode, while the spacing between the anode and intermediate cathode remains unchanged. In this sense, the spatial microdischarge current distribution alters with the external pressure changes. It is noticed that in this configuration, the mean free path of the ionized gas molecules does not meaningfully contribute to the current redistribution, although the pressure inside the sealed chamber will change theoretically due to the deformation of the diaphragm. This is because the pressure change due to the chamber volume change is too small to affect the mean free path of the ionized gas molecules, which has been proven by calculations.

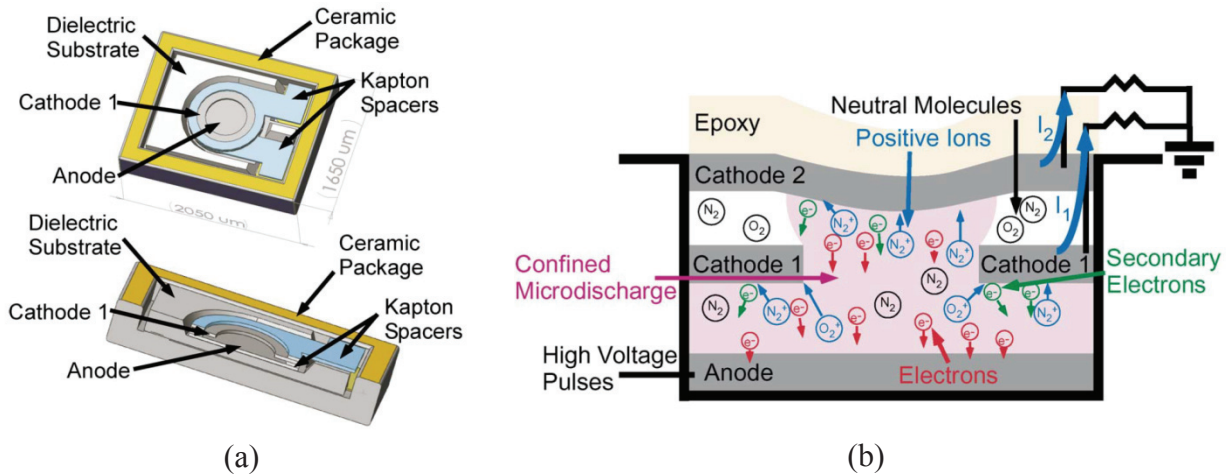


Figure 1.6: (a) Schematic of device contained within a commercial Kyocera package. (b) Diagram of a microdischarge between a single anode and two cathodes [Wri13].

The microdischarge-based pressure sensor, as a new member in existing pressure sensor family, has its unique advantages, including temperature immune, inherent large signal etc. Although prior work has demonstrated the application of microdischarges in pressure sensing [Wri09a, Wri13], many questions remain to be addressed, such as the scaling limit for the microdischarges, batch fabrication technologies, etc. These will be addressed in this dissertation.

1.4. Microfabricated High Voltage Generator for Microdischarge Initiation

1.4.1. Energy Scavenging Using Piezoelectric Materials

Microdischarges are attractive for miniaturized sensors in portable instruments. However, to provide high-voltage (HV) to initiate microdischarge is challenging for system integration. In fact, not only for the microdischarge-based transducers, HV sources are also of great interest for a number of other microsystems, including those that utilize electrostatic [Sum07] and piezoelectric actuation [Nah07]. In the microdischarge-based applications, the threshold voltages are typically a few hundred to a thousand volts.

One way to obtain high voltages in a portable system is using batteries and voltage converting circuits [Mit08b]. However, the lifetime of batteries could limit the application of those sensors in a long-term system. Sometimes it is difficult or even impossible to change batteries once the miniaturized systems are installed, for instance, monitoring systems that are embedded in infrastructures. Self-sustained sensor node systems are of particular interest. This concern has drawn large attentions in the MEMS community for a long time. One of the optimum ideas is to scavenge environmental energy, such as mechanical vibration, shock wave, solar energy, etc., to power microfabricated devices. Substantial efforts have been made to scavenge ambient mechanical energy and convert it into electrical energy [Kym98, Lel06, Ant07, Kue08, Gal11, Akt11]. For microsystem applications, piezoelectric energy conversion is attractive because of high efficiency [Rou03]. The piezoelectric effect is observed in materials such as lead zirconate titanate (PZT), quartz, and ZnO. Charge accumulates on the surfaces of these materials in response to applied mechanical stress. For microactuators and vibrational energy harvesters, PZT is appropriate because of its high piezoelectric coefficients and good electro-mechanical coupling. Energy harvesting devices that use PZT are conventionally designed to work in vibration mode and gather induced charges [Kue08, Akt11]. The output voltages are limited to several volts or even less than one volt. Research in energy harvesting using piezoelectric materials has been directed primarily at improving conversion efficiency of the energy harvesting system by selecting piezoelectric materials, optimizing electrode pattern, changing coupling modes and tuning the resonant frequency of the devices [Ant07]. However, the study of energy scavenging with high output voltage (>100 V) and high power density has not been extensively investigated.

Past efforts that were directed at increasing output voltage utilized several individual PZT elements connected together in series, and were based on vibrational PZT elements [Kob10, Zha12]. Two of these examples are shown in Figure 1.7. However, the output voltages of those studies were still inadequate for HV applications such as microdischarge-based sensing. Further, the use of multiple PZT elements typically increases the system complexity. In contrast, this work presents an approach to HV generation that uses a monolithic PZT51 element: electrode pairs that are patterned on the upper and lower surfaces of a single PZT element are series connected through a flexible polyimide cable [Luo12]. In response to transient mechanical loads, output peak voltages exceed 1 kV.

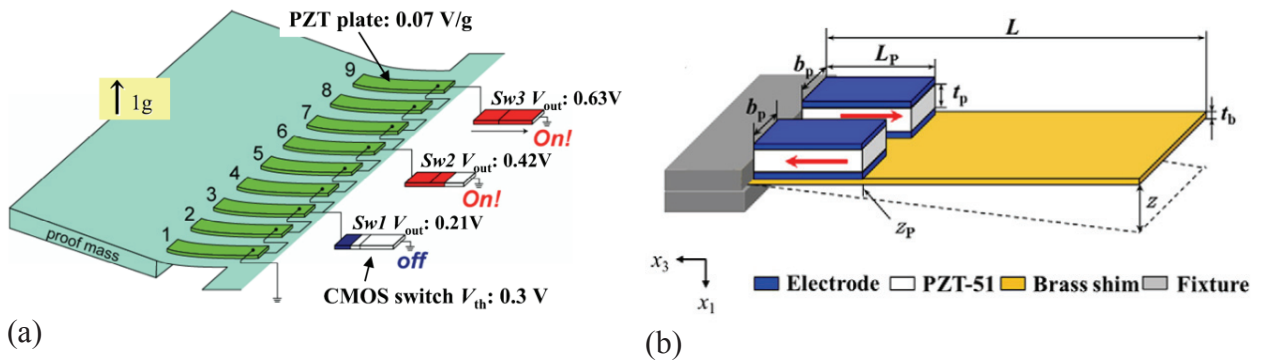


Figure 1.7: Examples of past work on increasing output voltage for (a) sensing accelerometer [Kob10] and (b) energy scavenging devices [Zha12], by connecting individual PZT element in-series.

The comparison of output voltage and voltage density (generated voltage per unit volume of the piezoelectric materials) of different energy scavenging devices is plotted in Figure 1.8. Although those works may focus on different targets, e.g. optimize output power, optimize working frequency, etc., the HV generator highlighted in this work produces highest output voltages with highest voltage density, and could potentially be used in microdischarge-based sensor systems.

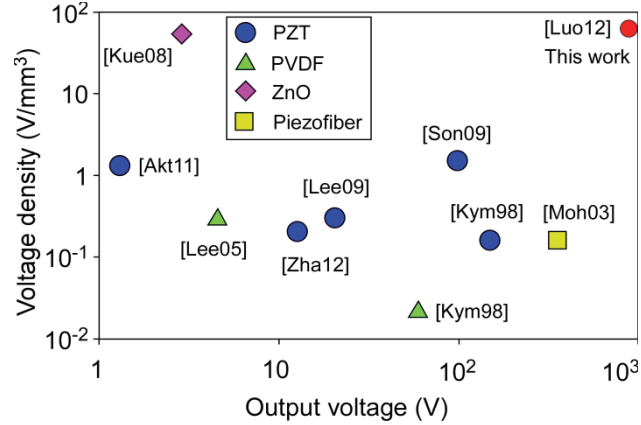


Figure 1.8: Comparison of output voltage and voltage density of different energy scavenging devices.

1.4.2. Nonlinear Piezoelectric Effect

In general, piezoelectricity in PZT is well described by standard linear piezoelectric constitutive equations at relatively low levels of applied electric field and stress. However, as the external field becomes larger, non-linearity is observed in the piezoelectric coefficients as well as the dielectric and elastic coefficients [Hal01]. Piezoelectric and dielectric properties are contributed by both intrinsic and extrinsic processes. Intrinsic contributions originate from the piezoelectric and dielectric responses of single domains, while extrinsic contributions arise from domain wall motions [Kim03]. However, only the extrinsic processes contribute to the nonlinearity [Ber59, Per04]. In the preparation of PZT ceramics, various dopants and additives are used to improve the electrical properties. Acceptor dopants (e.g. Mn, Fe) render hard PZT, such as PZT81, with lower piezoelectric coefficients and much reduced dielectric loss, while donor dopants (e.g. La, Nb) lead to soft PZT, such as PZT51, with high piezoelectric coefficients and relatively high dielectric loss. Because of the superior piezoelectric coefficients, soft PZTs are more attractive for high voltage generation by impact [Ber92].

The defects associated with dopants influence domain wall displacements, and thus have an effect on the nonlinearity [Mor05]. Damjanovic *et al.* reported the nonlinearity of piezoelectric effect in ferroelectric ceramics, including PZT, with devices operated in steady state [Dam96a, Dam96b, Dem96, Dam97a, Dam97b]. For static pre-loads up to 20 MPa superimposed with alternating pressure of 0–8 MPa, which are applied at 0.01–100 Hz, the d_{33} coefficient varied proportionally with the amplitude of the applied AC pressure (Figure 1.9). This non-linear effect is more evident in soft PZTs than in some other ferroelectric materials. For the HV generator presented in this work, soft PZT51 disks are used to provide the high voltage. However, for PZT51 disks that operate with rapid transients of stress and voltage, there is no evidence that the previously reported non-linearity is appropriately representative. To determine the effective non-linearity in the context of the HV generator, transient analysis is performed on the piezoelectric effect in PZT51.

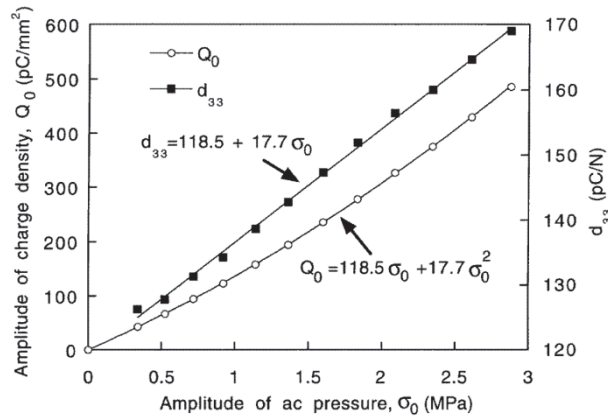


Figure 1.9: The longitudinal piezoelectric d_{33} coefficient and the amplitude of charge density Q_0 as a function of the amplitude of ac pressure for the PZT (63/37) sample doped with 4% at Nb. The dc bias pressure is 15 MPa [Dam97b].

1.5. Focus of This Work

Microdischarges offer a transduction approach that is potentially advantageous for certain microsensing systems. In order to utilize microdischarges effectively, however, a number of challenges must be addressed, ranging from device and package designs, to interface circuits, and power supply options. This work is primarily directed at the design and microfabrication of pressure sensors that use differential plasma currents. Two approaches are evaluated. The first uses a common anode and reference cathode located on a glass substrate, whereas a sensing cathode is located on an opposing silicon diaphragm that is deflected by applied pressure. Leads are transferred by electroplated through-glass vias. The second uses a common cathode and reference anode located on a silicon substrate, whereas a sensing anode is located on a thin film diaphragm that deflects under applied pressure. Leads are transferred by through-wafer isolated bulk-silicon lead transfer (TWIST).

For the microdischarge-based pressure sensors, there are three specific goals. (a) Miniaturization of microdischarge-based pressure sensors, targeting a 100× device volume reduction over prior work [Wri13]. (b) Investigation of microfabrication process that would potentially benefit other microdischarge-based sensors, and other microfabricated sensors based on different sensing principles. (c) Study of scaling properties of microdischarges by reducing device dimensions.

This thesis also describes a preliminary exploration of options to initiate microdischarges using scavenged energy – in this case from mechanical impact. Two specific goals are targeted: (a) Scavenging mechanical energy using piezoelectric materials and developing voltage boosting strategy; (b) Output voltages could be over 500 V to initiate microdischarges, and demonstration of microdischarge initiation on microdischarge-based sensors.

A miniature high voltage (HV) generator is formed by connecting multiple electrode pairs in series on a single PZT element. This strategy amplifies voltage roughly in proportion to the electrode pair count. A 3-electrode-pair device is used to successfully initiate microdischarges on a microdischarge-based sensor with peak voltages exceeding 1.35 kV. This work also provides the opportunity to study nonlinear piezoelectric behavior in transient mode. Effective piezoelectric coefficients increase linearly as the applied stress increases within the range of 1–5 MPa.

A number of challenges are addressed in this research. For microdischarge-based pressure sensors, potential challenges include: (a) Microdischarge initiation in small volume, high pressure with low breakdown voltages, (b) lead transfer as a general difficulty for sealed pressure sensors, (c) diaphragm design for the broad pressure range as targeted. For the HV generator, main challenges include (a) device design for effective scavenging of mechanical energy, (b) increasing output voltage from scavenged energy to a high level of hundreds of volts that have not been fully studied.

This research effort has yielded two additional outcomes that are noteworthy extensions of the primary contributions. 1) The evaluation of microfabricated electrode arrangements on a glass substrate has led to the first demonstration of pulse-plasma based gas sensors used in conjunction with gas chromatography. 2) The investigation of microfabrication processes for microdischarge-based pressure sensors has led to a low temperature process that can also be used to fabricate ultra-miniature capacitive pressure sensors. This process provides backside contacts that minimize the form factor and allow stacking of the sensor on interface electronics.

1.6. Organization of Thesis

This thesis is divided into five main chapters, with additional materials in appendices. Chapter 1 gives an introduction to this report, including literature reviews on pressure sensors and energy scavenging devices.

Chapter 2 describes the work on the first generation microdischarge-based pressure sensor fabricated by a two-wafer process. Technology in through-glass vias for 3-D electrical connection is investigated for the considerations of both lead transfer and device miniaturization. The exterior volume of the device is 0.05 mm^3 , which is $\approx 30\times$ smaller than prior work [Wri13] with interelectrode spacing $\approx 10 \text{ }\mu\text{m}$. The assembled device is tested in Ar environment, around atmospheric pressure, with varying interelectrode spacings.

Chapter 3 presents the effort on a further miniaturization of microdischarge-based pressure sensor, with interelectrode spacings less than $3 \text{ }\mu\text{m}$. The modified Paschen's law is considered for the second generation microdischarge-based pressure sensor when dimensions are aggressively scaled down. The devices are monolithically fabricated using a single wafer process. A through-wafer isolated bulk-silicon lead transfer (TWIST) technology is developed to achieve this further miniaturization. The exterior volume of the device is 0.01 mm^3 , another scaling down from the first generation by a factor of 5. The fabricated device is successfully tested in pressure range of 1–8 atm.

Chapter 4 describes the study on voltage boosting strategy and design of a monolithic PZT based high voltage generator aiming at microdischarge initiation. A configuration of in-series connected electrodes is proposed to increase the output voltage. The output voltages are characterized from 100 V to 900 V in response to the pulsed mechanical stress from 1 MPa to 5

MPa. Non-linear piezoelectric effect in transient mode is experimentally observed and presented in this chapter. The HV generator is then demonstrated to power a chemical vapor sensor.

Chapter 5 summarizes the findings and contributions of this work, and proposes the future work for a further miniaturization of microdischarge-based pressure sensor based on the configuration described in Chapter 3.

Appendices outline additional investigations on an application of microdischarge-based chemical sensor in gas chromatography, and a 100- μm diameter capacitive pressure sensor with 50-MPa dynamic range, fabricated using the process developed in Chapter 3.

CHAPTER 2:

First Generation Microdischarge-Based Pressure Sensor:

Two-Wafer Process with Through-Glass Lead Transfer

This chapter describes the investigation of a microdischarge-based approach for sensing the diaphragm deflection in a monolithically fabricated pressure sensor. This transduction approach is appealing from the viewpoint of miniaturization. The device consists of a deflecting Si diaphragm with a sensing cathode and a glass substrate with an anode and a reference cathode. The total exterior volume of the device is 0.05 mm^3 ; typical electrode size and separations are $35 \text{ }\mu\text{m}$ and $10 \text{ }\mu\text{m}$. Pulsed microdischarges are initiated in a sealed chamber formed between Si and glass chips and filled with Ar gas. External pressure deflects the Si diaphragm and changes the interelectrode spacing, thereby redistributing the current between the anode and two competing cathodes. The differential current is indicative of the diaphragm deflection which is determined by the external pressure. A 6-mask microfabrication process is investigated for device fabrication. Electrode connections to the interior of the chamber are provided by laser drilling and copper electroplating through high aspect ratio glass vias. The Si and glass substrates are bonded by Au-In eutectic. The re-distribution of plasma current between competing cathodes, as a consequence of diaphragm deflection over a range of pressure, was experimentally demonstrated.

2.1. Concept and Design

The device primarily consists of a glass substrate with copper filled through-glass vias (TGVs), a silicon diaphragm, one anode, and two competing cathodes, as shown in Figure 2.1. A microdischarge chamber is formed by the glass substrate, silicon diaphragm, and a Au-In eutectic bond ring. All three electrodes are made of thin-film Ni. The anode (A) and reference cathode ($K1$) are located on the glass side facing the microdischarge chamber. The sensing cathode ($K2$) is located on the silicon diaphragm, and is electrically connected to the exterior contact pad through a doped silicon layer and the $K2$ contact, which is a sandwich of Au and In layers in the interior of the chamber that mates with a TGV. All the electrical connections from within the chamber are routed to the exterior of the glass substrate through copper filled TGVs. In this three-electrode configuration, a voltage pulse is applied to initiate microdischarges, and two current paths are established between the anode and the two cathodes. (The pulsed nature of the microdischarge reduces power consumption and parasitic heating, but requires customized code for simulations and modeling, as discussed later.) As the diaphragm deflects due to external pressure, the spacing between the anode and the sensing cathode ($AK2$) decreases, but the spacing between the anode and the reference cathode ($AK1$) is essentially unaffected. This change of interelectrode spacing redistributes the spatial current: the ratio of sensing current (denoted by $I2$) between $AK2$, and reference current (denoted by $I1$) between $AK1$. The differential current, expressed as a fraction of the total peak current $(I1-I2)/(I1+I2)$, can then be used as the sensor output to indicate the value of external pressure. By using this relative change in current, the absolute current becomes less important, which minimizes the consequence of pulse-to-pulse variation in microdischarge characteristics.

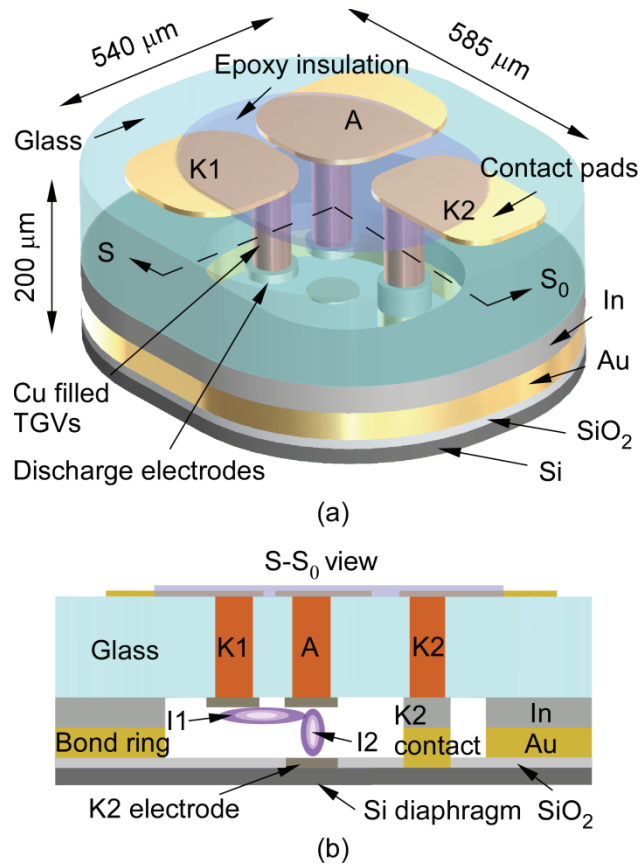


Figure 2.1: Concept of the microdischarge based pressure sensor. (a) 3D model of the pressure sensor. (b) S-S₀ view of the structure. I_1 and I_2 are discharge currents from two discharge paths.

The diaphragm is made of silicon to enable both large diaphragm deflection, within the fracture limit, and electrical conductivity. The eutectic bond ring is 200 μm-wide; it forms a sealed chamber (185 μm-long, 140 μm-wide) and determines the chamber height (and consequently the AK_2 interelectrode spacing). With this approach, etching the silicon or the glass to form a chamber is avoided. Electrostatic finite element analysis (FEA) using COMSOL[®] confirms that the use of this conductive bond ring as a spacing layer has little or no impact on the electric field profile. The discharge electrodes are made of nickel, which offers several benefits, including a high secondary electron emission coefficient (that contributes to a lower operation voltage), a high resistance to oxidation compared to alternatives [Wri13], a

convenient thin film deposition or electroplating, and ease of patterning. The architecture is designed with the vias in a glass wafer to provide adequate electrical isolation between the electrodes during device operation. This isolation allows the use of operating voltages that are 300–500 V or even higher. These vias are filled by copper electroplating. Prior work on 3D interconnect for integrated circuits (ICs) has mainly focused on through-silicon vias [Ngu02, Son08, Gu09, Gue12] for low-voltage devices. Through-glass vias have been investigated as means for providing better insulation and low-cost 3D packaging of ICs [Li02, Suk12]. More details of the approach to TGV fabrication are described in Section 2.3 of this chapter.

The interelectrode spacing and the thickness of the Si diaphragm are the most critical dimensional parameters of the design. The interelectrode spacing, the fill-gas, and the interior pressure of the chamber determine the discharge initiation (breakdown) voltage. The breakdown voltage between plane-parallel electrodes is given by the Paschen's curve (Figure 1.1) and as shown in Eq. (1.1). For this work Ar at 1 atm. is chosen for the fill-gas in the microdischarge chamber, because it offers lower operating voltages compared to nitrogen and is cost-effective. Based on this choice of gas and pressure, the *AK1* spacing is selected as 10 μm . The *AK2* spacing can be tailored by adjusting the thickness of the bond ring; it is set at 30 μm in the experiments.

The thickness of Si diaphragm has a significant influence on both sensitivity and dynamic range. A thinner diaphragm offers a high sensitivity but limits the pressure. To determine the appropriate design choice, FEA is performed using COMSOL[®] for pressures up to 50 MPa (Figure 2.2). A 5 μm thick diaphragm supports a large pressure dynamic range while allowing significant deflection. The deflection of the diaphragm supporting the *K2* electrode is up to

about 5 μm (0.12 $\mu\text{m}/\text{MPa}$) within the fracture limit, which is a significant fraction of the initial *AK2* spacing.

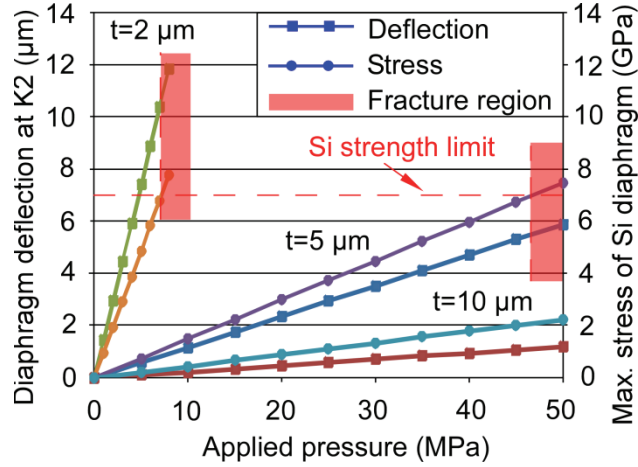


Figure 2.2: Simulation results of diaphragm deflection at cathode 2 and maximum induced stress for a 2 μm , 5 μm , and 10 μm thick Si diaphragms.

It should be noted that even for the smallest nominal *AK2* gap (10 μm), a full scale diaphragm deflection of 5 μm will only change the pressure within the microdischarge chamber from 1 atm. to about 1.2 atm. This is provided by the following formulae [Ged06], assuming that the ideal gas law is applicable and the gas inside the chamber is isothermal:

$$\Delta d = \frac{3 \cdot \Delta P (1 - \nu^2) a^4}{16 E h^3} \quad (2.1)$$

$$\Delta V = \frac{\pi \cdot a^2 \cdot \Delta d}{3} \quad (2.2)$$

where Δd is the deflection at the center of a circular diaphragm, ΔP is the pressure difference across the diaphragm, a is the radius, h is the thickness, ν is Poisson's ratio of the material, E is Young's modulus and ΔV is the volume change due to deflection.

The exterior dimensions of the device are shown in Figure 2.1. The total volume of the sensor in the design is 0.05 mm^3 , whereas the microdischarge chamber is only $2.2 \times 10^{-4} \text{mm}^3$.

2.2. Fabrication

The fabrication process requires 6 masks, 3 for glass processing (Figure 2.3) and 3 for silicon processing (Figure 2.4). The glass processing includes the laser-drilling of the TGVs, followed by the filling of the vias using copper electroplating. The next steps include the patterning of the contact pads on the exterior side of the wafer and the indium bond ring on the interior side of the discharge chamber. Finally, the Ni electrodes are patterned inside the microdischarge chamber. The silicon processing includes the deposition and patterning of an insulating oxide on the Si device layer of a silicon-on-insulator (SOI) wafer. This is followed by the patterning of the Au bond ring and *K2* electrode. Next, the glass and silicon chips are aligned and attached using a Au-In eutectic bonding method. Post-bonding, the Si diaphragm is released from the handle wafer by a deep reactive ion etching (DRIE) process, using the buried oxide layer as the etch stop.

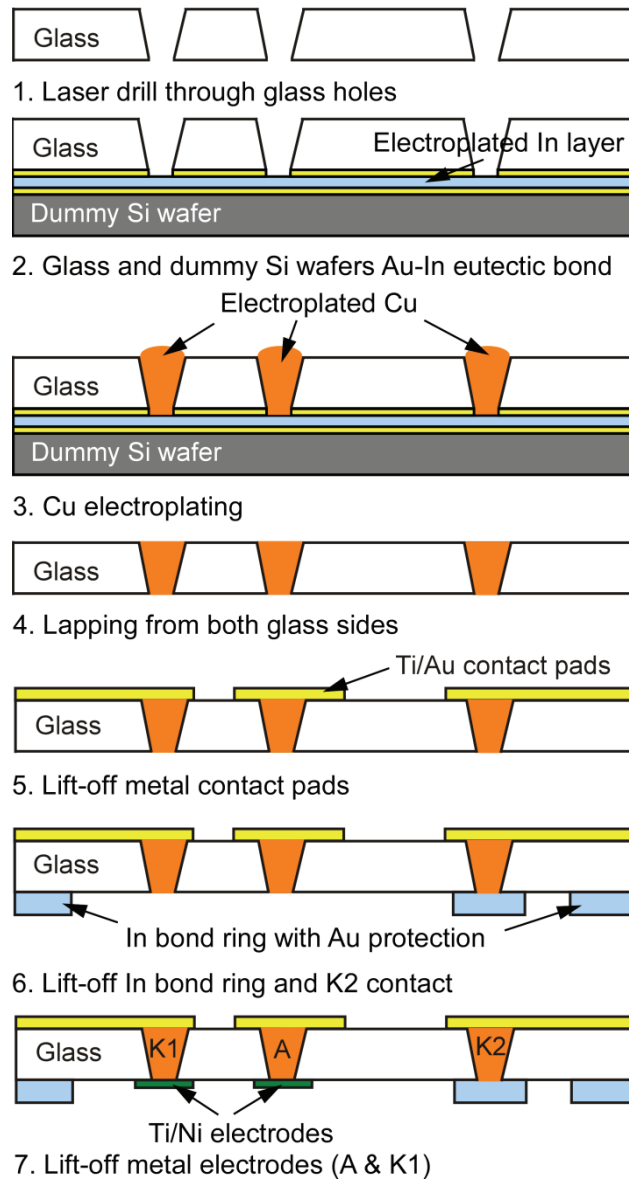


Figure 2.3: Process sequence for the glass wafer. 1) Through-holes are laser drilled. 2) Glass wafer is attached to a dummy Si wafer by eutectic bonding. A 4–6 μm thick electroplated indium layer on the dummy wafer serves as the seed layer for Cu electroplating. 3) Through-holes are filled by Cu electroplating. 4) A lapping step removes excess Cu and the dummy wafer. 5) The contact pads are deposited and patterned on the exterior of the glass wafer. 6) The bond ring and *K2* contact are defined on the interior side of the glass wafer. The In bond ring is covered with 50 nm Au for protection. 7) Electrodes are deposited on the interior of the glass wafer.

2.2.1. Glass Processing

The glass processing uses 300 μm -thick Schott Borofloat[®] glass wafers. In order to provide electrical contact from the pressure sensor electrodes (located within the sealed chamber) to the contact pads (located outside the chamber), vias are drilled (Precision Microfab, Severna Park, MD) using a 193 nm ArF excimer laser. This machining process has a depth control of approximately $\pm 5 \mu\text{m}$, a lateral precision of 1-2 μm , and a profile taper of 88.1° . The actual machined holes are 47.5 μm on the exterior side and 15.8 μm on the interior side for a machining profile of 87° (Figure 2.5a).

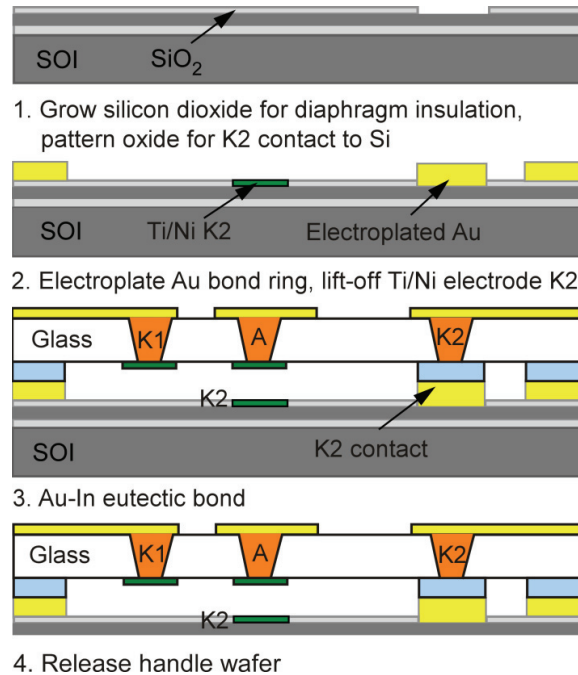


Figure 2.4: Process sequence for the Si wafer. 1) Silicon dioxide layer is grown and patterned on SOI for diaphragm insulation, and *K2* contact is then defined. 2) Au bond ring and *K2* contact on the interior of SOI wafer are electroplated. *K2* electrode is deposited by a lift-off process. 3) Eutectic bonding is performed between glass and silicon wafers. 4) Handle wafer is released by a backside dry etching.

A variety of methods can be used for achieving an electrical connection through the glass vias, including thin-film deposition, packing and melting of solder balls or powder, and electroplating. The high aspect ratios of the TGV structures make it impractical to achieve sufficient sidewall coverage for reliable electrical contacts using thin film deposition. The use of solder particles yields limited success because of inconsistent reflow when heated to the melting temperature (183°C for 37Pb/63Sn) and beyond (up to 280°C). Although the exact cause of this behavior has not been determined, it is possibly related to the large ratio of surface area to volume, which is known to prevent recrystallization.

Electroplating provides the consistency and scalability for filling the TGVs. Although a variety of plating metals are available, In and Cu are the best candidates for this application. Indium has a low reflow temperature (156°C), which allows temperature cycling post-plating in order to remove pinholes or voids. Copper offers lower resistivity and a higher plating rate. The higher re-melting temperature can also accommodate a higher operating temperature for the pressure sensor. Both metals were successfully plated in experiments.

Before electroplating, the glass wafer is attached to a dummy Si wafer coated with the appropriate metal seed layer (e.g. Ti/Au) for electroplating. Maintaining close contact and minimizing movement between the glass wafer and seed layer are critical. To ensure this, the dummy Si wafer is bonded to the glass wafer using Au-In eutectic bonding. Two other attachment options include photoresist to affix the dummy wafer [Li02] or electroless plating [Suk12]. The glass wafer is coated with a thin layer of Ti/Au 30 nm/300 nm. The dummy Si wafer is coated with a Ti/Au 30 nm/300 nm layer and a 4–6 μm-thick electroplated In layer. Following a degassing step to remove bubbles from the vias, Cu plating is performed (Enthone Cuprostar[®] CVF1) at 24°C. Pulse plating with periodic reversal of polarity is used to provide

uniform plating across the TGVs on the wafer. The effective current density is 15–20 mA/cm². After the plating, the stacked structure is lapped from the front to remove excessive metal build-up and planarize the surface, and from the back to grind off the dummy Si wafer. The measured resistance of the TGV is <5 Ω.

The next processing steps involve patterning the metal contact pads on the exterior side, followed by the patterning of the indium bond ring and Ti/Ni electrodes (*A* and *K1*) on the interior of the microdischarge chamber.

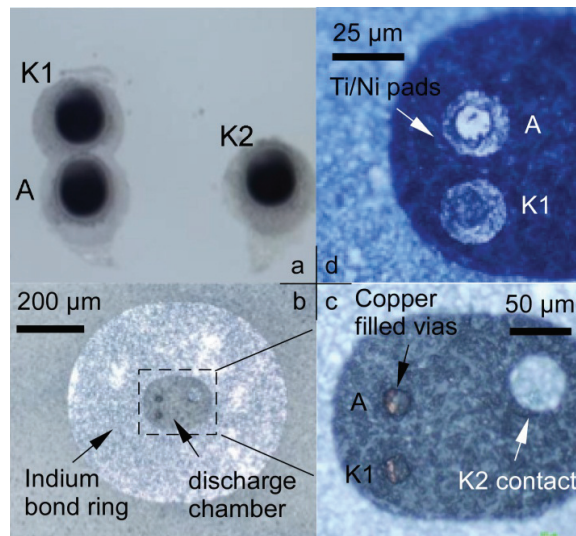


Figure 2.5: Optical photos of fabricated glass chip. (a) Laser drilled TGVs, out-chamber side. (b) TGVs are electroplated with copper; bond ring and *K2* contact are patterned with indium and Au protection. (c) Zoom-in view of the microdischarge chamber. (d) Anode and cathode *I* are patterned with Ti/Ni as electrodes by a lift-off process.

The Ti/Au (30 nm/300 nm) contact pads (located on the exterior of the glass chip) are patterned using the lift-off technique. To prevent discharges outside the chamber (*i.e.*, across the contact pad features), the corresponding contacts for the anode and two cathodes are strategically spaced farther apart compared to their spacing inside the chamber (10 μm), and partially coated with an insulating layer of epoxy above the TGVs (Figure 2.1).

The In bond ring (4 μm -thick, coated with a 50 nm-thick Au layer) and one side of *K2* contact are then formed by evaporation and lift-off (Figure 2.5). The Ti/Ni (20 nm/200 nm) electrodes (34.5 μm -wide) are formed by lift-off achieving an *AK1* spacing of approximately 11.1 μm . As shown in Figure 2.5d, the alignment of the TGVs and Ni electrodes is reasonably good and centered.

2.2.2. Silicon Processing

The silicon processing utilizes SOI wafers with a Si device layer (5 μm -thick), a buried silicon dioxide layer (2 μm -thick), and a Si handle wafer (500 μm -thick). The Si device layer includes As doping for low resistivity ($<0.005 \Omega\text{-cm}$); this is necessary to electrically route the *K2* electrode to the *K2* contact. When the glass and Si wafers are bonded, the *K2* contact on the Si wafer electrically connects to the *K2* contact on the glass wafer. This connection is then routed through the TGV to the contact pad for *K2*. The buried oxide layer provides a well-defined etch stop, which can later facilitate the final diaphragm release of the Si device layer by a backside dry etch of the handle wafer.

Silicon dioxide is grown (100 nm-thick, by dry oxidation at 1000°C) and then deposited (900 nm-thick low temperature oxide) for a total thickness of 1 μm on the Si device layer to provide electrical isolation of the bond ring from the *K2* electrode and contact. The oxide is patterned using a dry etch process based on CHF_3 and CF_4 to expose the doped device layer for the *K2* contact. Next, an 8 μm -thick Au bond ring and *K2* contact are provided by electroplating. In a following step, the oxide is removed in the region of the *K2* electrode, which is then formed by sputtering and lift-off of Ti/ Ni (20 nm/200 nm).

2.2.3. Eutectic Bonding

The transient liquid phase bonding technique has been used for vacuum packaging [Soh07, Str11] and wafer level attachment of ceramics (e.g., PZT) to Si [Akt09]. The motivations include: (1) a relatively low initial melting temperature (200°C) for the bonding step with the potential for high re-melting temperatures e.g., 500°C with Au-In; (2) the ability to bond a variety of surface profiles; and (3) the ability to control the thickness of the bond layer. The Au-In system was first investigated as a fluxless soldering technique in electrical packaging [Lee93, So00]. There are two basic types of Au-In bonding systems depending on the percent weight of the two metals: indium-rich [So00] and gold-rich bonding [Lee93]. If the weight percentage of indium is higher than 54%, also called “indium-rich”, the alloy is a mixture of indium and AuIn_2 , which means the re-melting (or de-bonding) temperature is still 156°C. If the weight percentage of indium is between 36.8–54 wt.%, the alloy is a mixture of AuIn and AuIn_2 intermetallic compounds with a re-melting temperature of 495.4°C and is considered “gold-rich”.

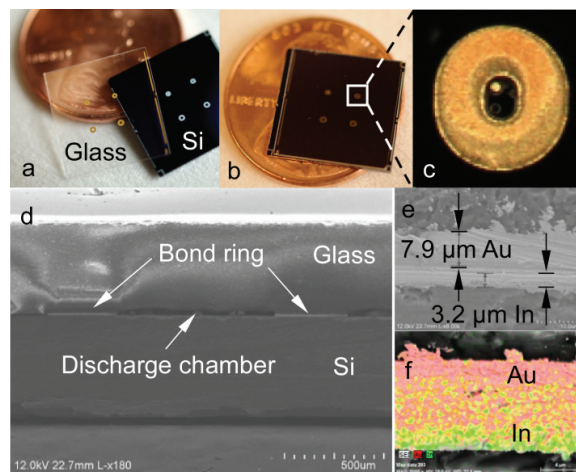


Figure 2.6: Chip level eutectic bonding of Au-In bond rings. (a) Glass and silicon chips, before and (b) after bonding, against a U.S. penny (Ø19.05 mm). (c) Zoom-in view of one bonded ring, viewed through glass. (d) SEM image of the cross-section of the Au-In bond ring. (e) SEM details of the bond structure. (f) Electron dispersive spectroscopy shows the diffusion of the Au and In components and the resulting Au and In intermetallic compounds that have formed.

For the pressure sensor described in this chapter, Au-rich bonding is used to ensure a relatively high operating temperature ($\approx 500^\circ\text{C}$). This bonding process does not depend on substrate materials (either glass or silicon). In this experimental investigation both cases, with Au on glass/In on silicon, and Au on silicon/In on glass were studied and successfully bonded. The bonding was performed in a vacuum oven at 200°C with an applied pressure >1 MPa for 90–120 mins. Figure 2.6d shows the cross-section of the bond ring structure captured using scanning electron microscopy (SEM). Electron dispersive spectroscopy (EDS) was used to evaluate the composition of the bond ring (Figure 2.6f). The EDS shows diffusion of the Au and In layers that form the intermetallic compounds.

2.3. Experimental Results

To evaluate the impact of multiple conditions for the interior of the microdischarge chamber, a test structure was formed in which the SOI wafer was thinned to $100\ \mu\text{m}$, but the handle wafer was not completely removed (Figure 2.7). The electrical characterization was performed with a glass chip and a SOI chip that were held together with a porous epoxy bond instead of an eutectic bond. The test structure was left unsealed and tested in an argon environment. The experimental setup is illustrated in Figure 2.8. A piezoelectric actuator was used to apply a force at the center of the assembled chip to induce a diaphragm deflection, which emulates a large external pressure. Voltage pulses of 1 ms duration were applied to the anode. Multiple microdischarge pulses were produced during each voltage pulse. Ballast resistor values of $10\ \text{M}\Omega$ and $20\ \text{M}\Omega$ were utilized in separate sets of experiments, while the currents going through two competing cathodes $I1$ and $I2$, were captured as voltages across $1\ \text{k}\Omega$ resistors.

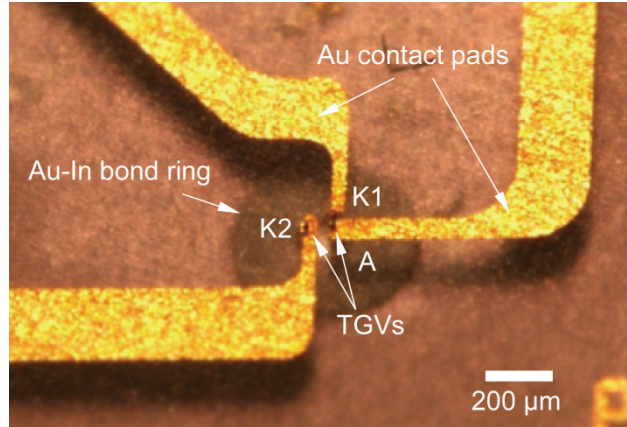


Figure 2.7: Photograph of the final assembly of the glass and silicon chips, viewed from the exterior of the glass.

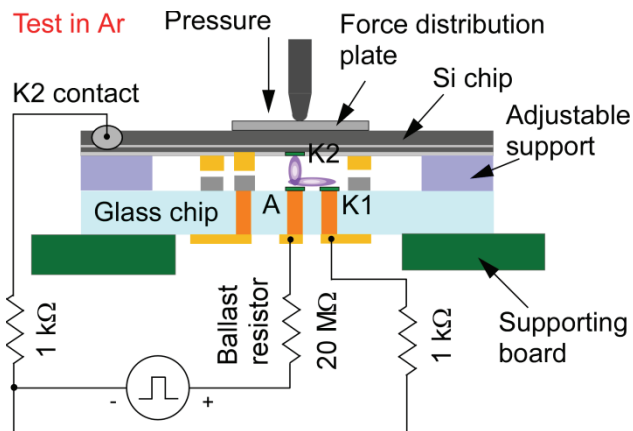


Figure 2.8: Test setup for the glass and Si chip assembly. A micromanipulator applies force at the center of the 100 μm -thick Si diaphragm to deflect the Si chip and change the $AK2$ spacing.

A representative waveform of a single microdischarge pulse is shown in Figure 2.9. The typical duration is several hundred nanoseconds with decaying oscillation. Possible sources of parasitic capacitance, to which the oscillation may be attributed, include the oscilloscope probes connected to $K1$ and $K2$. When a voltage pulse is applied to the anode, it also charges the parasitic capacitance on the anode, which can potentially contribute to the peak transient discharge currents.

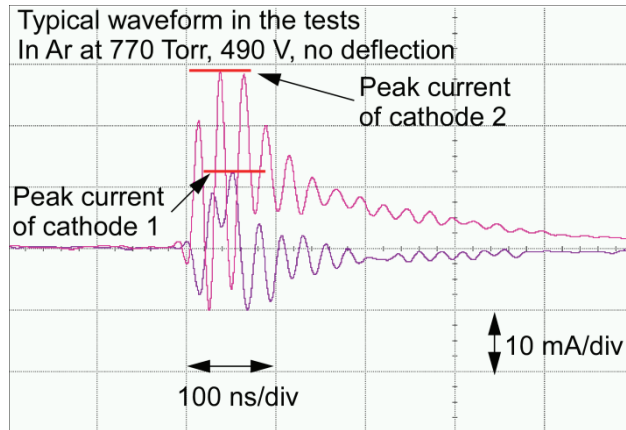


Figure 2.9: Representative waveforms of the microdischarges collected at the cathodes obtained from an oscilloscope during the tests.

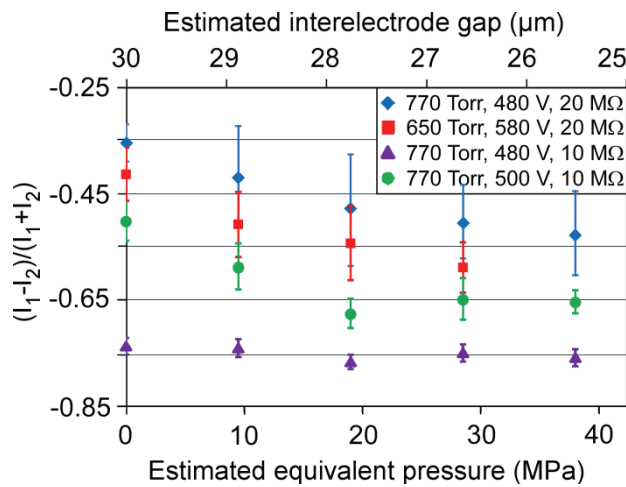


Figure 2.10: Differential currents from test results versus estimated equivalent pressure and interelectrode gap from simulation results based on a 5 μm thick Si diaphragm. I_1 and I_2 are peak values of envelope curves for AK_1 and AK_2 discharge waveforms, respectively. Tests are in Ar with the microdischarge chamber interior pressure between 650 Torr and 770 Torr. Applied voltage pulses are 480 V to 580 V. Ballast resistors are 10 $\text{M}\Omega$ and 20 $\text{M}\Omega$. Every point is the average of 5–8 measurements. Error bars indicate one standard error.

The relation between differential current and estimated equivalent pressure is plotted in Figure 2.10. The force applied to the diaphragm was converted to equivalent pressure using FEA. In four sets of experiments, the impacts of chamber pressure, applied voltage, and ballast resistor were investigated. When the ballast resistor value increases, the nature of the microdischarges changes and impacts the distribution of the cathode currents. For a chamber

pressure of 770 Torr and using a 20 M Ω ballast resistor, the operating voltage was 480 V and the differential currents ranged from -0.35 to -0.5. With a smaller 10 M Ω ballast resistor, the differential currents uniformly decreased.

Although the device is intended to operate with the microdischarge chamber at about 1 atm., the impact of lower pressure was also evaluated (Figure 2.10) with the test structure. At an interior pressure of 650 Torr, the (fractional) current in *KI* was lowered, as expected from the increase in the mean free path. Additionally, the operating voltage increased from 480 V for 770 Torr to 580 V for 650 Torr; this was also expected, given the nature of the Paschen's curve for Ar.

The impact of operating voltage on the discharge characteristics is also evident in Figure 2.10. For the microdischarge chamber pressure of 770 Torr and a ballast resistor of 10 M Ω , two magnitudes of voltage pulses were evaluated: 480 V and 500 V. For the 480 V pulses, the resulting differential current distribution as a function of diaphragm deflection does not indicate a clear trend. However, at 500 V, the impact of relative deflection can be clearly observed in Figure 2.10. This indicates the existence of a minimum threshold for the operating voltage of the pressure sensor. Thus, the combination of voltage (480 V) and ballast resistor (10 M Ω) is not expected to be selected for use.

Based on the electrical results, the mechanical load changed *AK2* by approximately 5 μm . This corresponds to the deflection expected from a 5 μm thick diaphragm of oval shape under an external pressure of about 40 MPa as noted in Section 2.1, and in Figure 2.2.

2.4. Discussion

The device is interrogated using high voltage pulses, and the energy consumption for each pulse is about 5 mJ. For previously reported work on pulsed microdischarge-based devices [Mit08a], the energy consumption can be as low as 2-20 $\mu\text{J}/\text{pulse}$. The power consumption for device described in this work depends on the duty cycle, but for 1 reading each second, it is ~ 5 mW.

Looking forward, it is notable that devices incorporating microdischarges are attractive for high temperature operation as electron temperatures are typically many eV (1 eV=11,600 K) and so are not significantly perturbed by a high ambient temperature [Wil03, Kus05]. For the conditions encountered in these devices, ions have temperatures moderately above ambient with transport coefficients that are also not particularly sensitive to high operating temperatures. Microdischarge-based pressure sensors have been operated as high as 1000°C [Wri09a]. Other pressure sensors for high temperature utilize Fabry-Perot and other interferometers [Gia06], and piezoresistors in high band gap materials such as SiC (up to 600°C) [Ned98] and even Si (up to 600°C) [Guo08]. The temperature tolerance of monolithic microdischarge-based pressure sensors will be investigated in our future efforts.

2.5. Conclusions

There are a number of conclusions that can be drawn from the effort described. First, the differential cathodes arrangement that was investigated – with anode (*A*) and reference cathode (*K1*) on the glass substrate, and the sensing cathode (*K2*) on the diaphragm – was demonstrated to produce a differential output current that was a function of diaphragm deflection. For an *AKI*

spacing of 10 μm , the fractional differential current changed by approximately 20% as $AK2$ changed from 30 μm to 25 μm . The overall device size was $0.585 \times 0.54 \times 0.2 \text{ mm}^3$. It was demonstrated that microdischarges could be initiated at voltages below 500 V in an Ar filled microdischarge chamber at about 1 atm. interior pressure. Further, the peak current levels were at a level of $\approx 10 \text{ mA}$, and pulse durations were $\approx 100 \text{ ns}$, which permits the discharge to remain relatively energy efficient. Tightly packed, high aspect ratio TGVs can be fabricated by combining laser drilling with electroplating. The electroplating can be performed with the aid of a Si dummy wafer that supports a seed layer; the wafer is eutectically bonded to the underside of the glass substrate, and later removed by lapping. Although the device design and fabrication approaches may continue to evolve, differential microdischarge currents present a viable approach to sensing diaphragm deflection, and so can be implemented in a variety of devices, such as gas or liquid pressure sensors in harsh environments.

CHAPTER 3:

Second Generation Microdischarge-Based Pressure Sensor: Single Wafer, Surface Micromachined Process with Through-Silicon Lead Transfer

This chapter presents a surface micromachined microdischarge-based pressure sensor with through wafer backside contacts. This second generation microdischarge-based pressure sensor targets a further reduction in sensor element volume from the one described in Chapter 2, which motivates a monolithic approach to design and fabrication. The microdischarge-based pressure sensors described in this chapter indicate external pressure based on the change of the spatial distribution of discharge current inside the sealed cavity, which is directly attributed to the change of the physical interelectrode spacings caused by the diaphragm deflection. Different from the previous design with two cathodes ($K1$, $K2$) and one anode (A), the structure in this design features one cathode (K) and two anodes ($A1$, $A2$) to enhance the current modulation caused by diaphragm deflection. The spatial distribution of microdischarge current, indicated by a differential expression of two current paths between one cathode and two anodes, is expected to monotonically increase with applied pressure. Additionally, the sensor is monolithically fabricated using a single wafer, combining surface micromachining and through-wafer isolated bulk-silicon lead transfer (TWIST). The use of TWIST technology not only solves a general problem of lead transfer from within the sealed cavity, but also provides an option of backside contacts for device miniaturization and ease of system integration. The active footprint of a

complete sensor measures $300 \times 300 \mu\text{m}^2$ in size. Explanations and discussions on experimental observations are provided at the end of the chapter.

3.1. Concept and Design

The second generation microdischarge-based pressure sensor (Figure 3.1) primarily consists of a deformable diaphragm with an anode ($A2$), a circular sealed cavity, and an oxide isolated silicon substrate with a cathode (K) and another anode ($A1$). Argon gas at ≈ 700 Torr is sealed in the cavity to facilitate microdischarge initiation. When high voltages (~ 100 's V) are applied between cathode and anodes, electrical breakdown occurs in the cavity under high electric fields ($\sim 10^8$ V/m), and discharges are created, leading to currents $I1$ and $I2$ (Figure 3.1b). In operation, the external pressure deflects the diaphragm and changes the interelectrode spacing between K and $A2$, while the spacing between K and $A1$ remains the same. The change of interelectrode spacing in turn redistributes the spatial plasma between $I1$ and $I2$. A more detailed examination reveals that there are additional factors at play, such as the interaction between the $K-A1$ and $K-A2$ electric field distributions. The normalized differential current between $I1$ and $I2$, expressed as $(I1-I2)/(I1+I2)$, is used to describe the plasma current distribution and serve as the sensor output to indicate external pressure value.

In practice, short-period high voltage pulses (~ 1 ms) are preferably utilized to not only reduce power consumption but also extend the electrodes lifetime. In addition, the use of three electrodes in a differential configuration effectively eliminates the impact of pulse to pulse variation in the absolute current. In the three-electrode configuration, two anodes and a single cathode are selected instead of two cathodes and a single anode previously described (Chapter 2) [Luo14, Eun14]. This is mainly because electron current has greater spatial variation than ion current [Wil03]. As a consequence, the electron current distribution is more sensitive to the

diaphragm deflection, which is of particular interest when the diaphragm deflection is limited due to the dimensional scaling. As shown in Figure 3.1b, all electrodes are electrically routed to the device backside contact pads by using the TWIST technology. In this manner, the contact pads do not increase the overall device. In addition, the backside contacts allow surface mount and chip stacking in the third dimension, eliminating wire bonding for system integration.

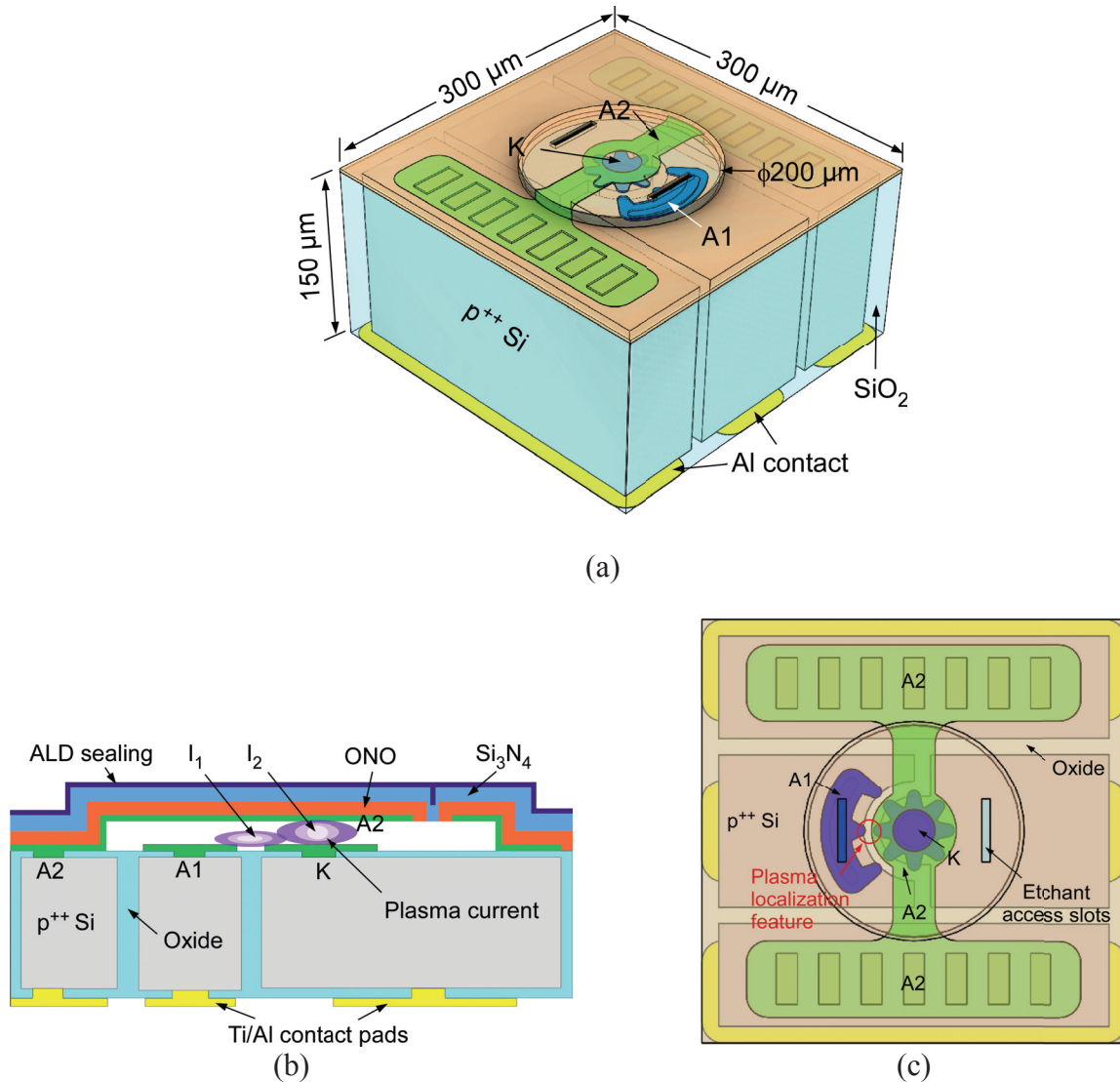


Figure 3.1: Schematics of the microdischarge-base pressure sensor. (a) A 3-D view with dimensions labeled. (b) A cross section view illustrating two plasma current paths inside the cavity, the configuration of multiple anodes and single cathode, and through-wafer isolated bulk-silicon lead transfer (TWIST) with backside contacts. (c) A top view showing the plasma localization feature.

As noted previously in Chapter 1, the electrical breakdown inside the cavity is determined by a number of factors, such as the interelectrode spacing, the fill-gas and the interior pressure of the cavity. For parallel and opposing electrodes, the breakdown voltage is described by the Paschen's curve (Eq. 1.1 and Figure 1.1). The compromise between breakdown voltage and dimension scaling is a major consideration in the design of the pressure sensors described in this chapter.

With consideration for performance targets and fabrication constraints, the cavity height is selected to be 3 μm ; this also defines the spacing between K and $A2$. To achieve comparable plasma current for $I1$ and $I2$, the same interelectrode spacing as $KA2$, *i.e.*, 3 μm , is also selected for the minimal interelectrode spacing between K and $A1$. A plasma localization feature, with aligned protrusions of the electrodes (Figure 3.1c), is designed for the in-plane electrode pair of KAI to better guide and control the plasma initiation. This feature allows spatial control of the region where the plasma discharge is initiated and also diminishes the voltage necessary to initiate the microdischarge.

The interior Ar pressure of the cavity is selected to be around atmospheric pressure (≈ 700 Torr), in order to reduce possible long-term leakage. Consequently, the $p \cdot d$ for this design is about 0.2 Torr-cm, which falls on the left side of the minimum in Paschen's curve (Figure 1.1) with an expected breakdown voltage > 1 kV. However, the breakdown voltage can be much lower than this theoretical value, if the enhanced field emission from the cathode is considered when the interelectrode spacing is smaller than 10 μm [Dha00, Sla02, Wal03, Hou06, Go10]. In fact, the enhanced field emission from the cathode due to both geometric surface enhancement and ion-enhancement can potentially lower the breakdown voltage below 400 V for this

particular design. Other major dimensions are labeled in Figure 3.1a. The total volume is $\approx 0.01 \text{ mm}^3$, about $5\times$ smaller than the first generation device [Luo14, Eun14].

The diaphragm is comprised primarily of an oxide-nitride-oxide (ONO) layer and a thick nitride layer, offering high fracture strength $\approx 6 \text{ GPa}$ and low residual stress [Gad06]. The discharge electrodes are made of nickel, which provides high secondary electron emission coefficient (that contributes to a lower operation voltage) and relatively high resistance to oxidation [Wri13, Eun14].

Finite element analysis (FEA) was performed using COMSOL Multiphysics® version 4.4 to study the diaphragm deflection and the maximum von Mises stress in response to external pressure (Figure 3.2). The initial stress of the diaphragm was set at 200 MPa based on the residual stress of silicon nitride measured at room temperature. The FEA results indicated that the diaphragm deflection had dynamic range from 0 to 2.7 MPa before touching the substrate, at which the maximum stress was less than 2 GPa . This corresponded to a safety factor >3 based on the fracture strength of Si_3N_4 material. As always, the simulation results depended on a variety of factors, including material properties and geometry simplifications, which can lead to differences from experimental results. Nevertheless, the simulation results provide insights into the design.

As noted in Section 2.2, the interior pressure of Ar-filled cavity may increase as the diaphragm deflects in response to applied pressure. Assuming that the ideal gas law is applicable and the gas inside the cavity is isothermal, even at the maximum diaphragm deflection the interior cavity pressure should not be more than $1,050 \text{ Torr}$ when the initial pressure is $\approx 700 \text{ Torr}$. It has been previously reported that a pressure change in the range of $1\text{--}4 \text{ atm}$ ($760\text{--}3,040 \text{ Torr}$) appeared to have no impact on the breakdown voltage when the interelectrode spacing was

smaller than 3 μm for the electrode geometry that was used [Dha00]. Thus, the interior pressure change of the microdischarge cavity in this design does not significantly impact the microdischarge initiation.

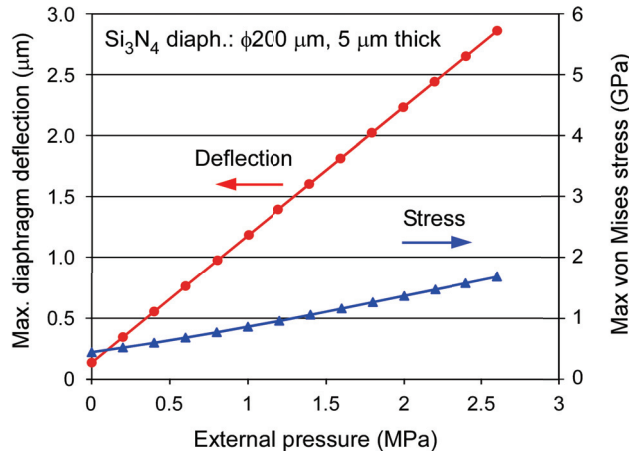


Figure 3.2: Finite element analysis of diaphragm deflection and maximum von Mises stress with selected dimensions in response to external pressure. In this simplified FEA, contact pressure for a 3 μm cavity height is ≈ 2.7 MPa.

3.2. Fabrication

The second generation microdischarge-based pressure sensor is fabricated by an 8-mask process (Figure 3.3) utilizing low resistivity ($<0.005 \Omega\text{-cm}$) p^{++} silicon wafers. The first mask defines deep reactive ion etch (DRIE) insulating channels with 4 μm wide and 250 μm deep features. The resulting trenches are fully filled with thermally grown SiO_2 and tetraethyl orthosilicate (TEOS) oxide. The wafers are then thinned by lapping and chemical mechanical polishing (CMP) both sides, which provides a flat, mirror surface finish. The final thickness was about 150 μm , but it can be thinner if necessary. After polishing, silicon oxide is deposited on both sides by plasma-enhanced chemical vapor deposition (PECVD) and patterned by reactive-ion etching (RIE) to provide contact vias for metal features using the second and third masks.

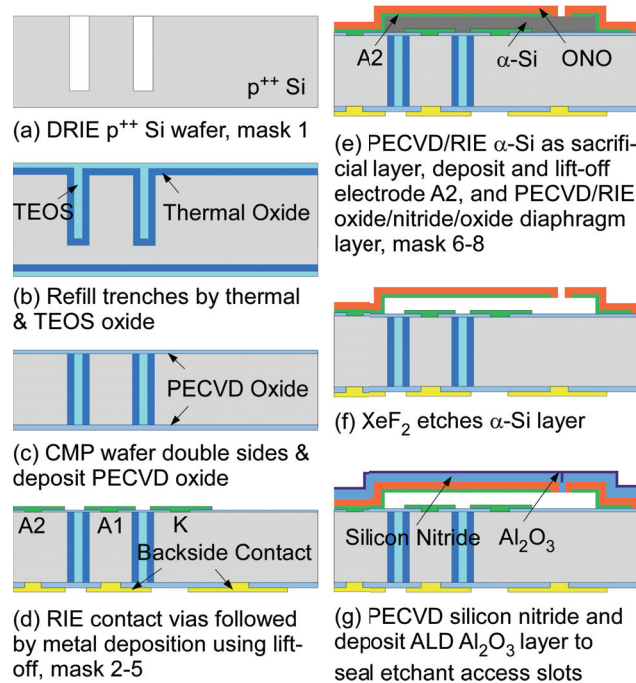


Figure 3.3: Fabrication process. (a) Heavily doped silicon wafer is etched by DRIE to define individual isolated region. (b) Etched trenches are filled by thermal oxidation and TEOS deposition. (c) Wafer is double-side lapped and polished, followed by PEDVD oxide on both sides. (d) Metal contact vias are patterned on PECVD oxide layers by RIE, followed by metal deposition using sputtering and lift-off. (e) Amorphous silicon is deposited and patterned as a cavity sacrificial layer, followed by another metal layer deposition and the first diaphragm layer oxide/nitride/oxide (ONO) deposition. (f) Amorphous silicon is etched by gaseous XeF₂. (g) Etchant access slots are sealed by a PECVD silicon nitride layer and an atomic layer deposition (ALD) Al₂O₃ layer.

Metal layers, including bottom electrodes (200 nm/50nm Ti/Ni) and backside contacts (50 nm/500 nm Ti/Al), are deposited and patterned by lift-off using the fourth and fifth masks. A 3- μm thick sacrificial layer for the sensor cavity is deposited by PECVD amorphous silicon ($\alpha\text{-Si}$), and patterned by RIE using the sixth mask. Following this, the top electrode (50 nm/200 nm Ni/Al) is patterned by lift-off using the seventh mask. To provide good step coverage across the $\alpha\text{-Si}$ layer, the electrode is deposited using sputtering instead of evaporation. Next, a stack of PECVD oxide-nitride-oxide (ONO) is deposited to form the first layer of the diaphragm, and patterned by RIE for etchant access slots using the eighth mask. The sacrificial $\alpha\text{-Si}$ layer is etched by gas phase XeF₂, which provides isotropic etching and very high selectivity to other

materials. The etchant access slots are sealed by a layer of PECVD nitride, followed by a 100 nm thick layer of atomic layer deposition (ALD) Al_2O_3 for hermeticity, which has proven to be a reliable approach to wafer level vacuum sealing [An13]. Optical images at various stages of fabrication are shown in Figure 3.4.

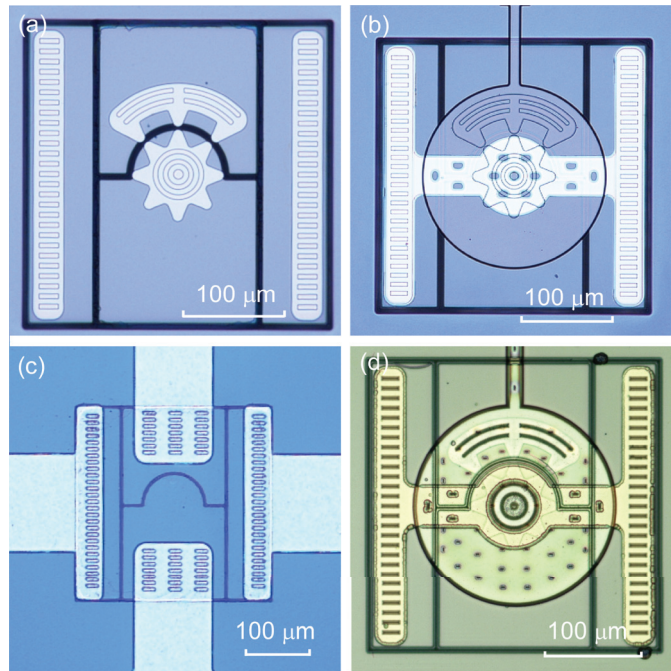


Figure 3.4: Selected fabrication results: (a) Top view of a device after bottom Ti/Ni electrode deposition. (b) Top view of a device after pattern of α -Si sacrificial layer and top Ni/Al electrode. (c) Back view of a final device with Ti/Al contact pads. (d) Top view of a final device.

The initial DRIE step targets a depth-to-width aspect ratio >60 , and requires special considerations to prevent lateral undercut, narrowing at the trench bottom, and premature self-termination. A standard Bosch process was used [Lae96], but both the etching and passivation cycles within it were optimized by a method described in [Owe12]. In the etch cycles, the bias power in the first second of the etch cycles was increased to improve ion directionality and passivation breakthrough. Additionally, the duration of the etch cycles was increased to allow more etchant gas to reach the trench bottom, and the chamber pressure was reduced further to

improve the etchant transport. In the passivation cycles, both duration and chamber pressure were increased to increase the thickness of passivation layer and reduce the lateral undercut at the top of the trenches. All these parameters were linearly and continuously changed over the whole 90 min. DRIE step. After DRIE, the trenches were fully filled by a combination of both thermal oxidation and TEOS oxide deposition (Figure 3.5a–b). Thermal oxide provides the insulation strength, whereas TEOS provides conformal filling that prevents the formation of voids in filled trenches. The total width of oxide is $\approx 6 \mu\text{m}$, which is expected to provide a high insulation strength and withstand operation voltages $>3 \text{ kV}$ [Bar09].

The PECVD silicon nitride used in the diaphragm is customized to target a modest tensile stress (150 MPa). A stack of oxide/nitride/oxide ($0.15 \mu\text{m}/0.8 \mu\text{m}/0.15 \mu\text{m}$) is used as the first diaphragm layer. The primary consideration is protection of the nitride layer from the later XeF_2 etch step. Because XeF_2 selectively etches silicon and the PECVD nitride is essentially “silicon rich,” the XeF_2 can potentially attack the diaphragm layer if there is no stacked oxide protection. After the deposition of all three dielectrics in the ONO stack, etchant access slots are patterned and opened in it. Slot dimensions of $1.5 \times 5 \mu\text{m}^2$ are selected to permit subsequent sealing by additional deposition steps. Smaller dimensions can be considered if appropriate lithography equipment is available. The sacrificial layer of $\alpha\text{-Si}$ is then etched by gaseous XeF_2 through the etchant access slots. Transparent ONO diaphragms are obtained after XeF_2 etching. SEM images of fabrication results are shown in Figure 3.5, and a typical device cross section is shown in Figure 3.5c–d. A number of measurements on multiple devices indicate that the diaphragm thickness varies from $4.90 \mu\text{m}$ to $5.03 \mu\text{m}$, and the cavity height is between $2.96 \mu\text{m}$ and $3.25 \mu\text{m}$.

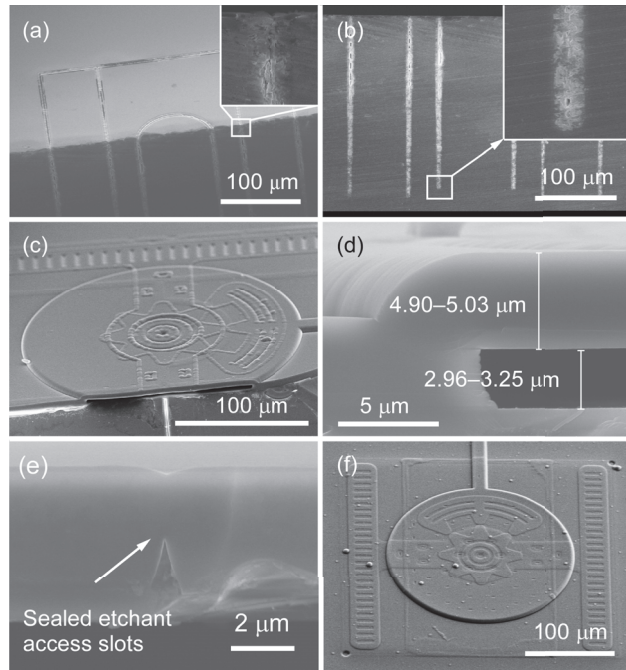


Figure 3.5: SEM images of (a) fully filled silicon trenches with details of trench top and (b) bottom, (c) cross section of a fabricated device and (d) enlarged details, (e) a sealed etchant access slot, (f) a fabricated device.

The sensor design includes a narrow channel connected to the discharge cavity (Figure 3.5f). The interior dimensions of the channels are $10 \times 3 \mu\text{m}^2$, and it is 2.4 mm long. It runs across the seam of the chips, so it is opened at the edge of the chip during singulation. It is used for filling the interior of the discharge cavity with the discharge gas, Ar, which as noted offers a relatively low breakdown voltage minimum on Paschen's curve. The devices are placed in a sealed chamber (Figure 3.6). After the chamber is pumped to vacuum to evacuate all ambient air from the microdischarge cavity, Ar is filled to a controlled pressure (≈ 700 Torr). The channels are then sealed with epoxy by a micromanipulator controlled probe inside the chamber.

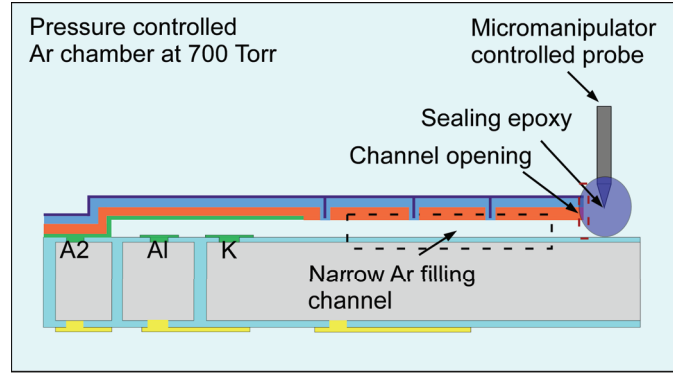
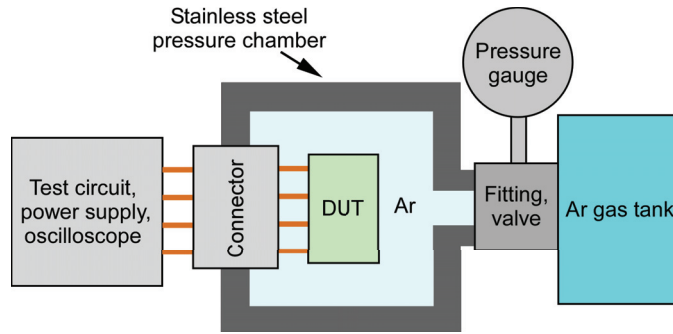


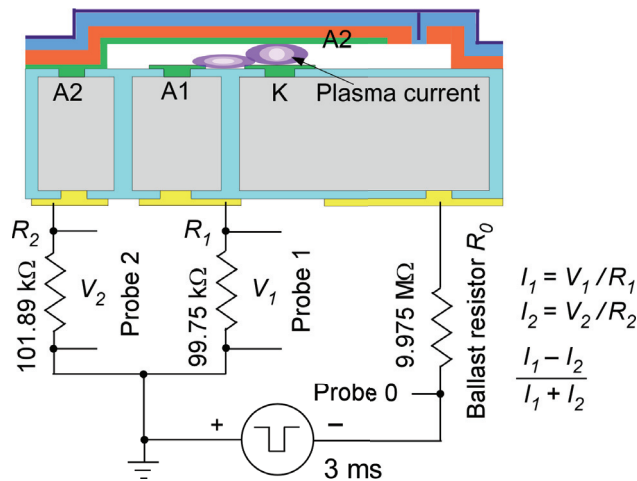
Figure 3.6: Schematic of the Ar sealing strategy. After the microfabrication, the narrow Ar filling channel is opened, and then the device is placed in a pressure controlled chamber. The chamber is first pumped to vacuum, followed by filling with Ar at ≈ 700 Torr. A micromanipulator is used to control the probe to apply epoxy at the channel opening.

3.3. Experimental Results

For testing, the device under test (DUT) was surface mounted to a prototype board using conductive silver epoxy. The prototype board was then soldered to an electrical connector, which was inserted into a customized stainless steel pressure chamber (Figure 3.7a). The DUT was tested in a gaseous environment, pressurized by a gas tank and monitored by a reference pressure gauge. The test circuit is shown in Figure 3.7b. Negative voltage pulses of 200–300 V with duration of 3 ms were applied to the cathode through a ≈ 10 M Ω ballast resistor. This limited the discharge current to 10–100 μ A, limiting power consumption, and preventing unnecessary heating and plasma damage to the electrodes. Two relatively small resistors $R1$, $R2$ were connected to $A1$ and $A2$, respectively, to read out individual microdischarge current $I1$ and $I2$ from oscilloscope probes. Applied voltages were monitored by a high voltage oscilloscope probe, denoted as *Probe 0* in Figure 3.7b.



(a)



(b)

Figure 3.7: Experimental setup. (a) Device under test (DUT) is surface mounted to a prototype board, which is soldered on a connector. The connector is inserted in a customized stainless steel pressure chamber, which is connected to a gas tank with a reference gauge. (b) Test circuit. Negative voltage pulses (3 ms) are applied on the device through a ballast resistor. Microdischarge current I_1 and I_2 are read out through pick up resistor R_1 and R_2 using oscilloscope probes.

In experiments, the voltage was gradually increased until breakdown occurred. The electrical breakdown was experimentally observed at 250 ± 50 V over the external pressure range of 1–8 atm (101–811 kPa). No monotonic trend of breakdown voltage was found in this range. Typical profiles of microdischarges are shown in Figure 3.8. At low pressures (1–2 atm), microdischarge current appeared as DC current during the 3 ms supplied voltage pulse (Figure 3.8a). The intensity of the DC current was relatively low, and the total current $I_1 + I_2$ was 2–3 μA .

In contrast, the microdischarges were pulse-like when external pressure exceeded 2 atm (Figure 3.8b). In addition, the intensity of discharge was higher, with total peak current $I_{1p}+I_{2p}$ around $10 \mu\text{A}$. As evident in the microdischarge profiles, decaying charging currents appear in both $KA1$ and $KA2$ at the beginning of voltage pulses; this is the combined effect of the parasitic capacitors and the ballast resistor. To calculate the normalized differential current $(I_1 - I_2)/(I_1 + I_2)$, the steady current was used for DC-like discharge, while peak current was selected for pulsed microdischarge. The pressure response in the range of 1–8 atm is plotted in Figure 3.9. Based on the measurements of total current, plasma impedance can be calculated, which is also included in Figure 3.9.

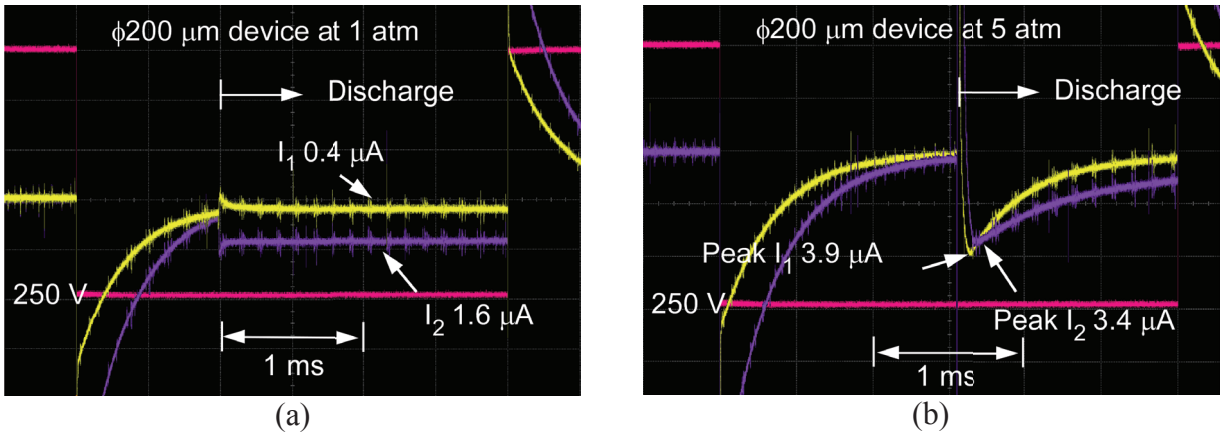


Figure 3.8: Typical profiles of microdischarges (a) at low pressure (1 atm) with DC-like discharge current, and (b) at high pressure (5 atm) with pulsed discharge current. Breakdown voltages were 250 V. The red line denotes applied voltage, yellow is I_1 and violet is I_2 .

From Figure 3.9 it is evident that the normalized differential current monotonically increases from -0.7 to 0.2 with increasing external pressure from 1 atm to 8 atm, whereas the plasma impedance reduces from $\approx 100 \text{ M}\Omega$ at low pressure ($< 3 \text{ atm}$) to $\approx 20 \text{ M}\Omega$ at high pressure ($> 4 \text{ atm}$). The differential current transitions from negative to positive around 4 atm, which implies the currents $KA1$ and $KA2$ are well balanced, as necessary to achieve a high sensitivity.

The spatial current distribution between $I1$ and $I2$ shifts from $KA2$ to $KA1$ with increasing external pressure or reducing cavity gap. These results are discussed in Section 3.4.

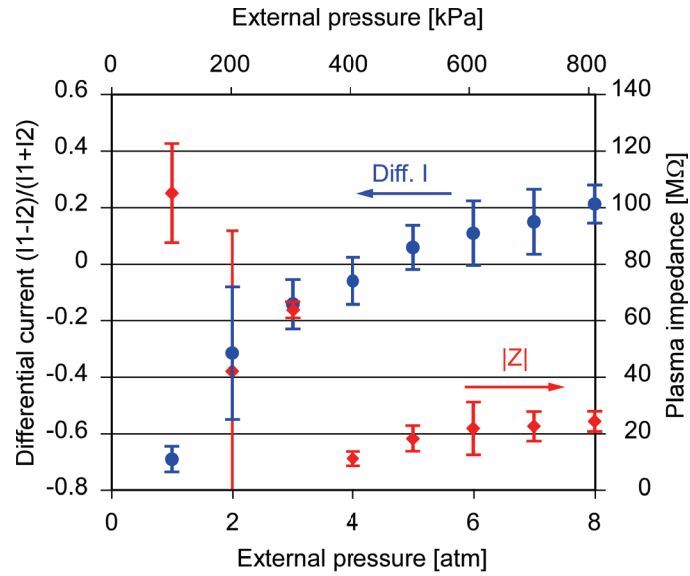


Figure 3.9: Pressure response of the DUT: normalized differential current and the corresponding calculated plasma impedance against the external pressure from 1 to 8 atm. Breakdown voltages were 250 ± 50 V. Every data point was an average of 10–20 microdischarge readings. Errors bar indicate one standard deviation.

In addition to the DC-like and pulsed microdischarges described above, a low intensity steady current was observed in $KA2$ only at high pressures ≥ 5 atm (Figure 3.10). Compared to the profiles of the DC-like discharges and the pulsed discharges, there was no clear breakdown that appeared as a current jump in this smoothly transitioning current profile. The pressure responses of the low intensity steady current $I2$ and corresponding plasma impedance in pressure range of 5–8 atm are plotted in Figure 3.11. The current increases near-linear with increasing pressure in the given range, and the maximum intensity is about $1.2 \mu\text{A}$. More discussion is presented in Section 3.4.

Larger external pressure was applied to the DUT in experiments above 8 atm. However, the diaphragm touched the substrate at ≈ 9 atm, which was determined by an observation of short

current between *KA2* when low voltages (≈ 30 V) were applied. When the pressure dropped to ≈ 7 atm, the short current disappeared, which confirmed that the short current was due to the contact between diaphragm and substrate.

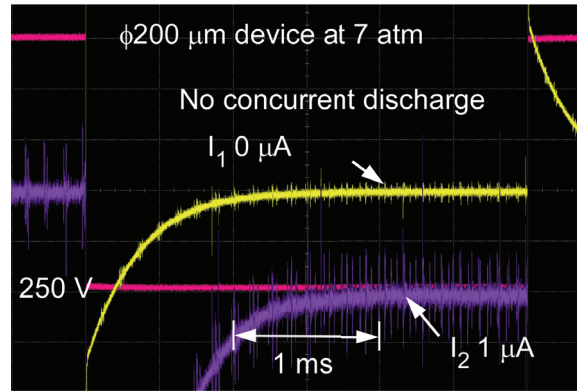


Figure 3.10: Typical profile of the low intensity steady current I_2 at high pressure, while I_1 was zero. Voltage pulses (3 ms) at 250 V were applied. The red line denotes applied voltage, yellow is I_1 and violet is I_2 .

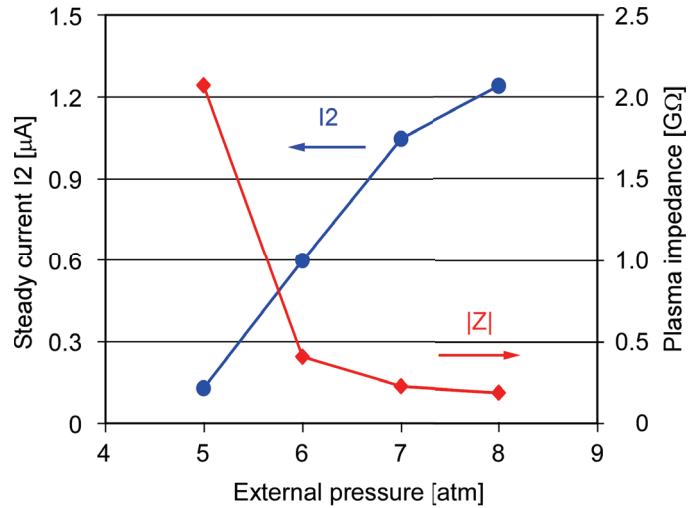


Figure 3.11: Low intensity steady current I_2 and calculated plasma impedance with external pressure from 5 to 8 atm. Voltage pulses (3 ms) at 250 V were applied.

3.4. Discussion

There are a number of points about the operation of the pressure sensor that are worth noting. The first point concerns the contact pressure, at which the interelectrode gap is reduced to zero. There are two simplifications which cause the compliance of the diaphragm to be larger than anticipated by the simulation. As shown in Figure 3.5e, the diaphragm is thinner in the region near sealed slots, which increases the deflection in response to applied pressure. Additionally, the applied high voltage introduces an electrostatic force between $KA2$, which varies inversely with the square of interelectrode gap. Thus, the electrostatic force plays a more important role when the gap is small, *i.e.*, at higher applied pressure. In experiments, it was found that the external applied pressure at which the diaphragm is deflected to the point that the electrodes are shorted is approximately 9 atm (912 kPa). This is substantially lower than the 2.7 MPa contact pressure predicted by the simplified FEA in Figure 3.2.

The second point concerns the pressure response. As evident from Figure 3.9, fractional $I2$ diminishes with applied pressure, indicating that the $p \cdot d$ product within the discharge cavity is smaller than the value that leads to the minimum breakdown voltage in Paschen's curve (Figure 1.1), *i.e.*, it is to the left of the minimum in the plot. From another perspective, discharge current $I2$ tends to retreat from the electrode edges, following a longer path. The available paths are influenced by the windows in the electrode metal that were provided for the etchant access slots in the diaphragm. The change in the interior pressure of the cavity with the deflection of the diaphragm may also have a minor influence. The breakdown voltage does not significantly increase because of reasons outlined in Section 1.2.3. Adding more electronegative species to the fill gas can potentially reduce the breakdown voltage.

The third point concerns the low intensity steady current observed through *A2* at 5–8 atm applied pressure. The high impedance of this plasma component suggests the presence of a Townsend or dark discharge that may contribute to the initiation of microdischarge observed in Figure 3.8.

3.5. Conclusions

In summary, this Chapter presented the second generation microdischarge-based pressure sensor with a further miniaturization in both device volume and the interelectrode gaps compared to the first generation described in Chapter 2. In pursuit of the miniaturization, a TWIST technology was explored, which provided through-wafer lead transfer with backside contacts and was suitable for high voltage applications. Devices were successfully fabricated using an 8-mask process and tested in gaseous environment in the range of 1–8 atm. Both DC-like and pulsed microdischarges were observed concurrently in *I1* and *I2*, with breakdown voltage ≈ 250 V. The normalized differential current $(I1-I2)/(I1+I2)$ was monotonically increased from -0.7 to 0.2 with external pressure increased from 1 atm to 8 atm. The plasma impedance reduced with smaller cavity gap at high external pressures. Low intensity steady current was also observed between only *K* and *A2* at high pressures (≥ 5 atm).

CHAPTER 4:

A Pulsed High Voltage Generator for Microdischarge Initiation

This chapter presents a monolithic pulsed high voltage (HV) generator utilizing a single piezoelectric element (PZT51 disk, 5 mm in diameter and 740 μm thick) with electrodes series-connected via a flexible polyimide cable. The design, fabrication, assembly and testing of the HV generator are described. In response to transient mechanical load, the HV generator is evaluated within the stress range from 1 MPa to 5 MPa and the corresponding peak output voltages vary from 100 V to 900 V. Performance comparison between single-electrode pair HV generator and three-electrode pair device indicates series-connected electrodes on a monolithic PZT element greatly boost the output voltage under the same mechanical load conditions. In further tests, the generated high voltage pulses exceed 1.35 kV and are successfully used to initiate microdischarges on monolithically patterned electrodes across a 75 μm air gap. The measured capacitance of the test HV generator is 25 pF and the calculated charge delivered to the terminal electrodes in each discharge is 34 nC. The nonlinear piezoelectric property of the PZT51 in transient mode is studied. A linear increase of the effective piezoelectric coefficient as the applied pressure increases within the range from 1 MPa to 5 MPa is experimentally obtained.

To integrate the microdischarge-based sensors into a long-term, self-powered microsystem, sustainable high voltage energy sources are favorable. Although the research on miniaturized energy scavenging devices has been substantially studied for more than ten years, there is still no work that has been reported yet aiming at the microdischarge initiations. This

work [Luo12] investigates the energy scavenging from the pulsed mechanical energy with high voltage outputs for microdischarge applications. The design, modeling and fabrication of the HV generator are described in Section 4.1. Experimental results of a three-electrode pair device and its comparison to a single-electrode pair device are described in Section 4.2, along with the demonstration of microdischarge initiation in a practical device. Section 4.2 also describes the non-linear piezoelectric effect of the PZT51 disk used in the HV generator operating in transient mode. Discussion and conclusions are included at the end of this chapter.

4.1. Design Modeling and Fabrication

4.1.1. Design and Configuration

A schematic representation of the HV generator is shown in Figure 4.1. A monolithic PZT disk (PZT51, 5 mm in diameter, 740 μm thick) is patterned with gold electrodes on both surfaces. The patterned PZT is then sandwiched between a 75 μm thick flexible polyimide (Kapton[®]) cable. Opposing and vertically aligned electrodes on the upper and lower surfaces form an electrode pair that operates together. All three electrode pairs are then series-connected by this cable, *i.e.*, the top electrode of one pair is connected to the bottom electrode of another electrode pair. The bottom electrode of the first pair and the top electrode of the third pair are connected to the output pads on the same polyimide cable. The output signal is measured at these output pads.

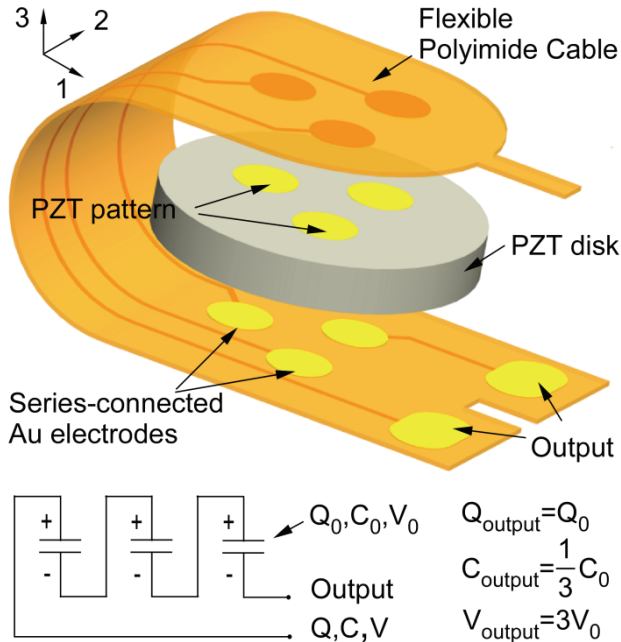


Figure 4.1: Schematic diagram of the HV generator and its circuit model, including a monolithic PZT disk with three series-connected electrode pairs through a flexible polyimide cable. The HV generator is analyzed using a series-connected capacitor model.

The PZT element operating in $d33$ orientation generates positive and negative charges along the polarization direction in response to the external mechanical stress applied in the same direction. For the PZT element used in this paper, the polarization lies along the thickness, which provides an electric potential difference between two sides of surfaces. When three electrode pairs are connected in series, the equivalent voltage output is the summation of every individual voltage. As a result, the electric potential distribution on the surface of the PZT element will not be uniform. For example, Figure 4.2 shows COMSOL Multiphysics[®] 4.3 simulations under uniform mechanical loads on the PZT surface. It is also evident from this simulation that the segmentation and series connection of the electrodes provides higher voltage than a conventional element for the same applied stress.

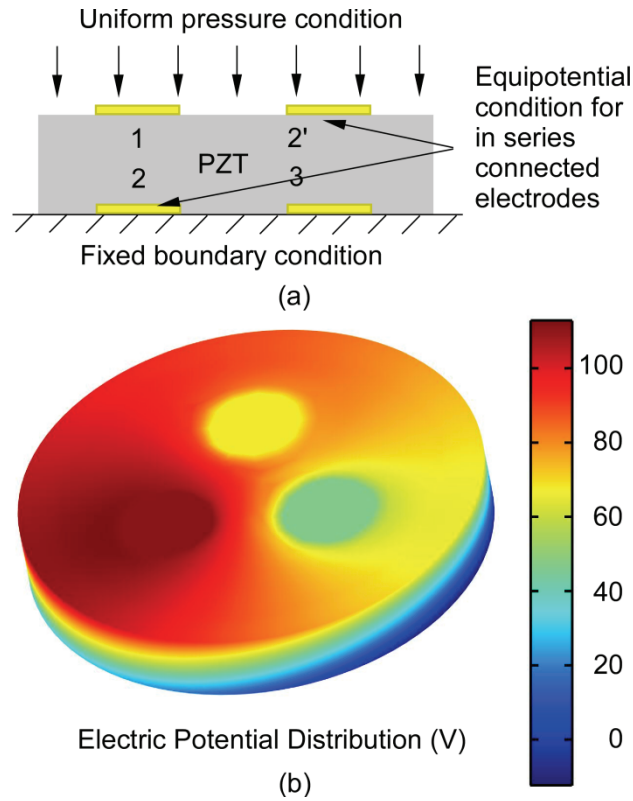


Figure 4.2: Simulation in COMSOL Multiphysics[®] 4.3. (a) Uniform pressure of 5 MPa is applied on a $\varnothing 5$ mm, 740 μm thick PZT disk. Series-connected electrodes are set as equipotential. (b) Electric potential distribution.

4.1.2. Theory and Modeling

From the general constitutive equation of piezoelectric material and considering such PZT element operating in d_{33} mode, the relation between mechanical stress and electrical voltage is described by:

$$\begin{aligned}
d_{ij} &= \begin{pmatrix} 0 & 0 & 0 & 0 & d_{15} & 0 \\ 0 & 0 & 0 & d_{24} & 0 & 0 \\ d_{31} & d_{32} & d_{33} & 0 & 0 & 0 \end{pmatrix} \\
\sigma_{ij} &= [\sigma_1 \quad \sigma_2 \quad \sigma_3 \quad \sigma_4 \quad \sigma_5 \quad \sigma_6]^T \\
\begin{bmatrix} D_1 \\ D_2 \\ D_3 \end{bmatrix} &= d_{ij} \sigma_{ij} = \begin{bmatrix} d_{15} \sigma_5 \\ d_{24} \sigma_4 \\ d_{31} \sigma_1 + d_{32} \sigma_2 + d_{33} \sigma_3 \end{bmatrix}
\end{aligned} \tag{4.1}$$

in which, d_{ij} the piezoelectric coefficient for PZT materials; σ_{ij} denotes the mechanical stress applied to the PZT element; D_{ij} is the electric displacement. In this effort, it is assumed that the only non-zero input stress is σ_3 and it is applied uniformly to the top surface. Solid mechanics analysis shows that although uniaxial load along direction 3 induces radial strains because of a non-zero Poisson's ratio, the lateral stresses, σ_1 and σ_2 , are negligible. In addition, the stress σ_3 does not introduce shear stresses σ_4 , σ_5 , and σ_6 . Thus, the induced voltage due to the piezoelectric effect is accrued only in direction 3, and can be expressed as:

$$V_3 = E_3 t_{PZT} = \frac{D_3 t_{PZT}}{\epsilon_{33}} = \frac{d_{33} t_{PZT}}{\epsilon_{33}} \sigma_3 \tag{4.2}$$

in which, E_3 and ϵ_{33} are the electric field and electrical permittivity in direction 3; t_{PZT} is the thickness of the PZT element and V_3 represents the voltage built across the surfaces along the thickness direction. The voltage generated across the PZT surfaces is proportional to the thickness of the PZT element and the applied mechanical stress along axis normal to the PZT surface. With uniformly applied stress, for a PZT element with uniform thickness, the potential on each surface is the same. Therefore, no voltage is built between electrodes that are located on the same surface of the PZT element.

Figure 4.1 shows the equivalent circuit model of the HV generator. Each pair of electrodes is modeled as an individual capacitor with capacitance C_0 . Nominally, this design concept could obtain output voltage up to $N \cdot V_0$, in which N is the total number of electrode pairs on the single PZT elements, V_0 is the voltage across each electrode pair. In the current configuration, the nominal output voltage is $3V_0$. However, the fringe capacitance limits the nominal amplification that is achieved.

Two main cases of fringe capacitance exist in the above model, as illustrated in Figure 4.3. Table 4.1 lists the comparison of these models in terms of the charges, equivalent capacitance and built voltage. From the comparison, the fringe capacitance increases the equivalent capacitance, which, in turn, decreases the built voltage. For calculating these fringe capacitances, Bansal *et al.* studied an analytical model using conformal mapping, and expressed as [Ban06]:

$$C_{f1} = C_{corner} = \frac{\epsilon D}{\pi} \sqrt{\frac{HS}{H^2 + S^2}} \quad (4.3)$$

$$C_{f2} = C_{top,top} = \frac{\epsilon D}{\pi} \left[\ln\left(1 + \frac{2W}{S}\right) + e^{\left(-\frac{T+S}{3S}\right)} \right] \quad (4.4)$$

where H , S , W , T are geometry parameters as shown in Figure 4.4; D is the depth of the metal which does not show in that 2-D illustration; ϵ is the dielectric constant of the material between two metals. Minimizing the influence from fringe capacitances is necessary to achieve better performance for the HV generator. One effective approach is thinning the PZT element to increase the equivalent capacitance of the device and reduce the fringe capacitance influence.

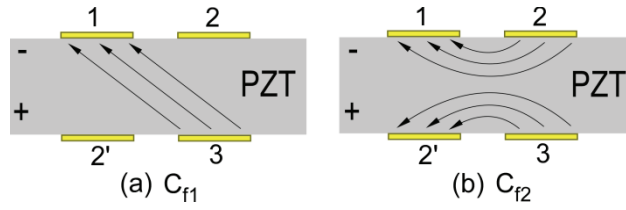


Figure 4.3: Schematic illustration of two cases of fringe capacitance. Electrodes 2 and 2' are shorted together. The arrows indicate electric fields in charged fringe capacitors.

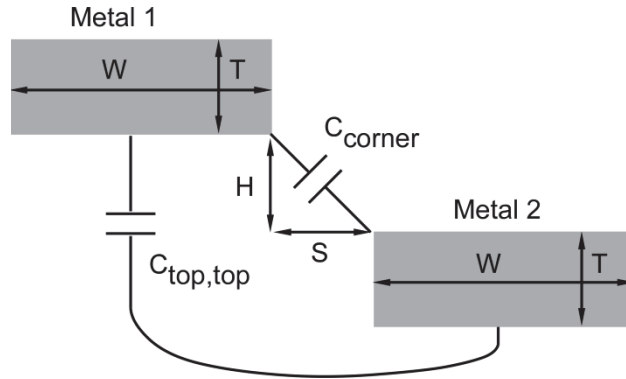


Figure 4.4: Illustration of two types of fringe capacitance that exist in the HV generator.

Table 4.1: Comparison of different circuit models considering fringe capacitance.

	Simplified model	Fringe case (a)	Fringe case (b)	Combination
Circuit model				
Charge	Q_0	Q_0	Q_0	Q_0
Capacitance	$\frac{C_0}{2}$	$\frac{C_0}{2} + C_{f1}$	$\frac{C_0 + C_{f2}}{2}$	$\frac{C_0 + C_{f2}}{2} + C_{f1}$
Voltage	$\frac{2Q_0}{C_0}$	$\frac{2Q_0}{C_0 + 2C_{f1}}$	$\frac{2Q_0}{C_0 + C_{f2}}$	$\frac{2Q_0}{C_0 + C_{f2} + 2C_{f1}}$

4.1.3. Fabrication and Assembly

The fabrication of HV generators begins with appropriately sized PZT discs (Figure 4.5). These can be acquired in the necessary dimensions or fabricated by ultrasonic machining and lapping, as described in [Li06]. Then, both sides of the PZT disk are patterned with 100 nm Cr/500 nm Au electrodes by evaporation. The flexible polyimide cable (Sierra Circuits, Inc., CA, USA) with Cu leads embedded within it and Au contacts exposed is wrapped around three sides of the PZT disk. A narrow slot and a flat pin with the same dimension at two ends of the cable are designed as alignment marks for assembly process. The patterned PZT is sandwiched by the folded flexible polyimide thin film cable along the alignment mark. The sandwiched structure is then bonded using both superglue in the field regions and conductive silver epoxy at the cable contacts. The assembled HV generator is shown in Figure 4.6 against a U.S. penny.

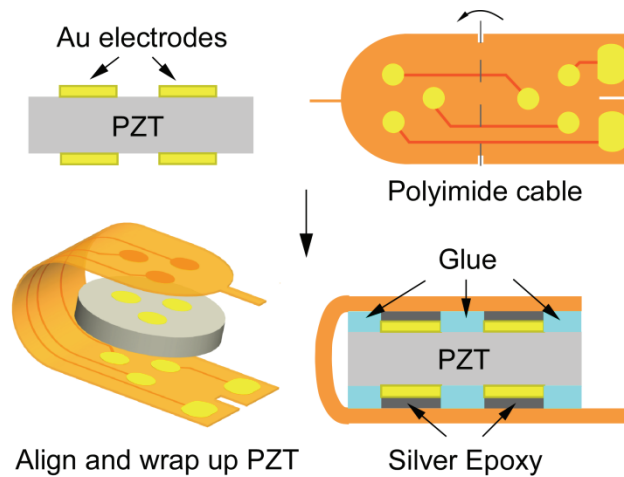


Figure 4.5: Fabrication and assembly process. Both sides of PZT51 disks are patterned with Cr/Au electrodes. The patterned PZT disks are then sandwiched by customized flexible polyimide cables, and bonded using both superglue and silver epoxy.

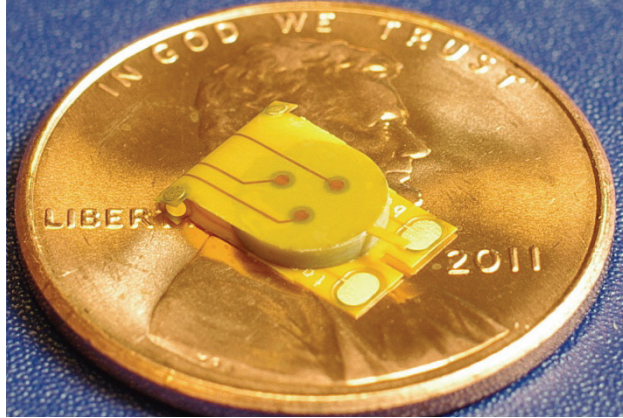


Figure 4.6: The assembled HV generator against a U.S. penny of 19.05 mm diameter.

4.2. Experimental Results

4.2.1. Experimental Setup

The experimental setup is depicted in Figure 4.7. The assembled HV generator is mounted on a load cell (208C01, PCB Piezotronics Inc., NY, USA) to determine the applied mechanical load. In order to protect the PZT element and uniformly transfer the mechanical load, a 500 μm thick glass cover with the same lateral dimension as the device is attached to the device surface. A transient mechanical load in the experiment is applied by dropping a stainless steel ball (6.8 mm in diameter) directly on the glass cover. The ball is guided by a glass tube held vertically above the device. By adjusting the height of release position, the applied mechanical load is controlled accurately.

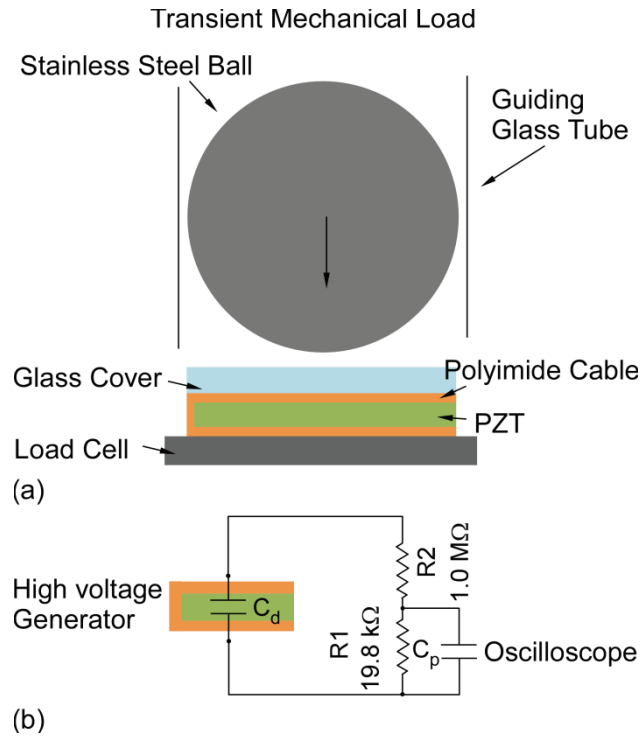


Figure 4.7: Experimental setup. (a) Transient load is applied by dropping a stainless steel ball (OD 6.8 mm) guided by a glass tube. (b) Resistor divider readout circuits. C_d and C_p are the capacitance of the HV generator and the oscilloscope probe, respectively.

A resistive divider is used to measure a fraction of the generated voltage through an oscilloscope probe (Figure 4.7b). The measured voltage is then converted to the generated voltage by considering the division factor. Using this readout circuit instead of directly measuring the full output voltage reduces the influence of the capacitance of the oscilloscope probe. Otherwise, the measurement capacitance introduced from the oscilloscope probe has a significant influence on measured output voltages for the HV generator. In the Figure 4.7(b), the capacitance of the device and the oscilloscope probe are respectively denoted by C_d and C_p ; C_d is measured as 25 pF and C_p is typically around 12 pF (although it can vary from 7 pF to 15 pF).

The measured voltage, V_m , is:

$$V_m = \frac{Q_d}{C_d + \frac{R_1}{R_1 + R_2} C_p} \quad (4.5)$$

where Q_d is the charge generated by the HV generator; $\frac{Q_d}{C_d}$ is the HV voltage intended to be measured. Equation (4.5) indicates that increasing the ratio of R_2/R_1 would reduce the influence from the measurement probe. For the selected values of resistors, the measured voltage could reach 95% of the voltage intended to be measured according to this simple model. This is validated by simulation using NI Multisim™ software, as shown in Figure 4.8. In reality, the model of PZT and measurement probe may be more complicated.

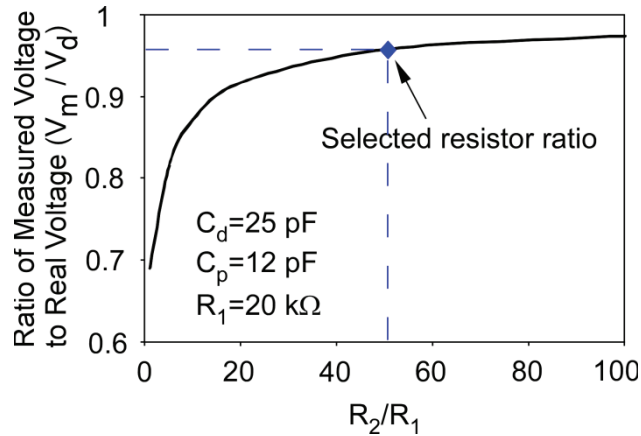


Figure 4.8: Simulation in NI Multisim™ of the ratio of the measured voltage to the real value as a function of the voltage division.

4.2.2. Experiments on HV Generator

In order to validate the proposed device concept and characterize the HV generator, two types of devices were tested in experiments. One was the three-electrode pair HV generator discussed above, with electrode pairs series-connected via a flexible polyimide cable. The other

one was a single-electrode pair device, with only one electrode pair connected to a flexible polyimide cable while the other two electrode pairs remain disconnected. For these two types of devices, except for different numbers of electrode pairs that connected into the circuit, all the other conditions and components were the same. Experimental results of both devices are shown in Figure 4.9. Both devices yield an increasing output voltage as the applied stress increases. Specifically, the three-electrode pair device is able to produce pulsed high voltage with peak value up to 900 V in response to a 5 MPa stress pulse, whereas the single-electrode device generates peak voltage close to 400 V under the same mechanical load. This result clearly demonstrates the voltage boost achieved by the series-connected electrodes on a monolithic PZT element.

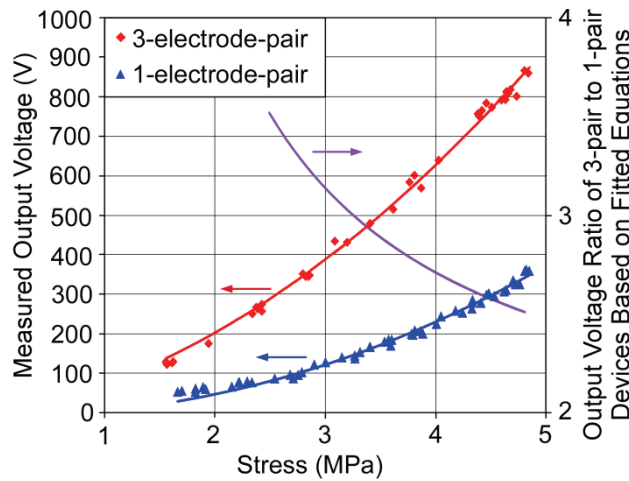


Figure 4.9: Experimental results of the measured output voltage as a function of the applied mechanical stress from single-electrode pair device and three-electrode pair device. Voltage amplification provided by the output voltage ratio of the three-electrode pair to single-electrode pair devices determined by equations fitted to experimental data.

Experimental data points are fitted by a second order polynomial function in the form of

$$V = A\sigma^2 + B\sigma$$

using the least squares method, and the equations are expressed by:

$$\begin{aligned} {}^{(3)}V &= 27.32\sigma^2 + 47.95\sigma \\ R^2 &= 0.995 \end{aligned} \quad (4.6)$$

$$\begin{aligned} {}^{(1)}V &= 16.67\sigma^2 - 8.63\sigma \\ R^2 &= 0.991 \end{aligned} \quad (4.7)$$

where ${}^{(3)}V$, ${}^{(1)}V$ are output voltage of the three-electrode pair device and the single-electrode pair device, respectively, with unit of V; σ is the peak value of the applied mechanical stress, with unit of MPa. The ratio of the voltage output from the two devices under the same mechanical load is also plotted in Figure 4.9, based on the fitted equations (4.6) and (4.7). As noted previously in Section 4.1, this ratio varies from the nominal value of 3 possibly because of the fringe capacitance and parasitic inductive components within the arrangement that might affect the transient response. The transient mechanical load applying on the HV generator is limited by the measurement capacity of the load cell; therefore, stress levels above 5 MPa were not characterized.

4.2.3. Non-Linearity of the Effective Piezoelectric Coefficient

Since the experimental test setup utilizes intermediary layers of glass and polyimide between the ball and the PZT, an effective piezoelectric coefficient, d'_{33} , is introduced to estimate the piezoelectric coefficient of the HV generator. The value of d'_{33} can be obtained from the experimental measurements of both three-electrode pair devices and single-electrode pair devices. The latter are less affected by parasitics, and consequently may provide better representation of the non-linearity of the true piezoelectric coefficient. Using equations (4.2), (4.6), and (4.7), the effective piezoelectric coefficient d'_{33} is derived as:

$$d'_{33} = \frac{V}{\sigma t_{PZT}} \varepsilon_{33} = A\sigma + B \quad (4.8)$$

where ε_{33} is constant, t_{PZT} can be regarded as constant, because the deformation of PZT disk is negligible compared to its initial thickness. Thus, A , B are constant coefficients depending on the properties of piezoelectric materials and device structures. As shown in Figure 4.10, the experimentally derived effective piezoelectric coefficient, d'_{33} , is a stress-dependent variable, which is different from constant values of the piezoelectric coefficients in conventional models. For stress levels in the range of 2.5–5 MPa, the piezoelectric coefficient increases by 419 (pC/N)/MPa based on the single-electrode pair device. Previous reports of non-pulsed behavior of PZT materials also indicate that the piezoelectric coefficient increases linearly with applied stress at higher levels, but remains relatively unaffected by stress at lower levels [Hal01, Dam96a].

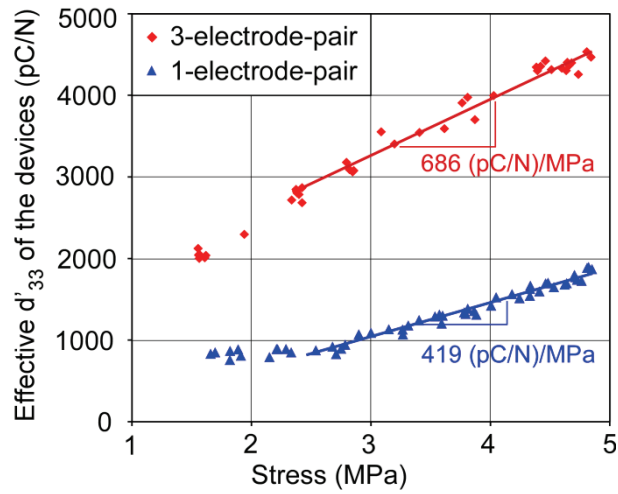


Figure 4.10: Effective piezoelectric coefficient, d'_{33} , for the single-electrode pair device and the three-electrode pair device. Data points are calculated based on experimental results shown in Figure 4.9 and Eq. (4.2). Linear fittings are based on Eq. (4.6)–(4.8).

4.2.4. Demonstration of Microdischarge Initiation

To demonstrate a potential application, the HV generator was used to power a microdischarge-based chemical vapor sensor [Mit08a, Luo11], as shown in Figure 4.11. The core component of this sensor is a $1 \times 1 \text{ cm}^2$ glass chip with thin film Ni electrodes patterned on the surface. The anode and cathode are separated by a $75 \text{ }\mu\text{m}$ gap, where microdischarges occur in the air gap above the electrodes when the voltage higher than the breakdown voltage is applied. This particular chemical sensor typically needs a voltage pulse $>800 \text{ V}$ to initiate microdischarges between sensing electrodes [Luo11]. The microdischarges break chemical bonds of the vapor species around the sensing electrodes, emitting characteristic spectra that are captured by a portable spectrometer. By analyzing the emission spectra, the chemical vapor can be identified. As shown in Figure 4.11a, the HV generator was connected to the anode and cathode of the chemical vapor sensor chip across a $19.8 \text{ k}\Omega$ current-limiting resistor. The transient mechanical load was applied using the same approach used in the characterization experiments (Figure 4.7). Figure 4.11b is an optical image of the sensor electrodes before the onset of a microdischarge, whereas Figure 4.11c shows a transient microdischarge that was triggered by the HV generator. In these experiments, the voltage across a $19.8 \text{ k}\Omega$ resistor connected in series with the discharge gap was monitored. A typical transient pulse is shown in Figure 4.12. One peak is as high as 1.35 kV , and voltage pulses oscillate with decaying amplitude. The inset of Figure 4.12 shows that the highest voltage pulse appears at the beginning and is built up within several nanoseconds. This first and highest voltage pulse initiates the microdischarge. From the voltage response profile, the charge transfer in each microdischarge is calculated at about 34 nC .

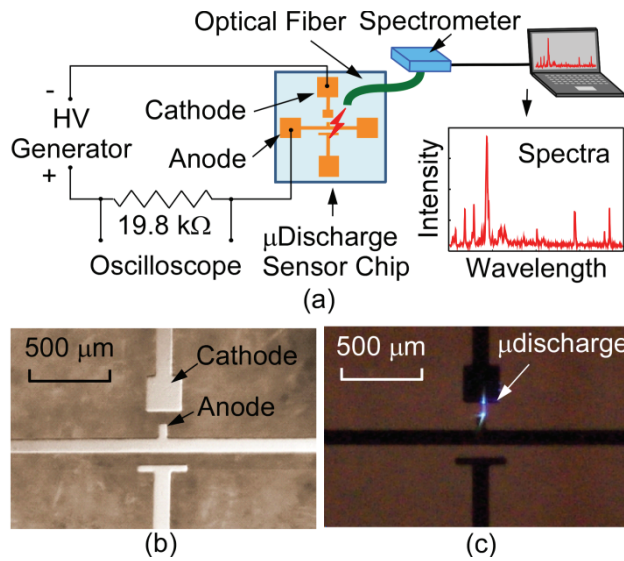


Figure 4.11: Demonstration experiment setup and results. (a) Experimental setup for testing the HV generator on a microdischarge based chemical vapor sensor. (b) Electrodes details of the microdischarge chemical vapor sensor, before discharge. (c) Discharge moment of the chemical vapor sensor.

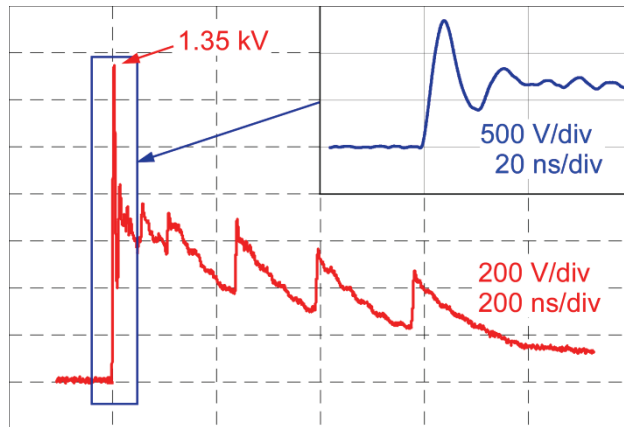


Figure 4.12: Measured transient voltage response across a 19.8 kΩ resistor during the discharge.

4.3. Discussion

It is worthwhile to note that there are several approaches by which the HV generators can be enhanced. First, increasing the number of total electrode pairs is clearly an option to increase the output voltage. However, several caveats are associated with this approach: Limited by the

surface area, a large number of electrodes imply smaller gaps between electrodes on the same plane, increasing fringe capacitance. More series-connected electrode pairs render a far smaller equivalent capacitance that delivers that charge, and less dominant over the fringe capacitance. Additionally, the alignment and bonding process can become more complicated.

Another possible approach to enhancing the voltage output is to minimize the fringe capacitance by redistributing the electrodes patterned on the PZT surface to enlarge the distance between any two electrodes. The fringe capacitance associated with two output electrodes has the most deleterious impact, because it is directly added to the equivalent capacitance of series-connected electrode pairs, with which it is in parallel. Therefore, those two output electrodes should have a greater spacing between each other than their counterparts.

The third approach to performance enhancement is to optimize the thickness of the PZT disk based on Eq. (4.2). A thicker PZT element would build larger voltage. However, the equivalent capacitance would correspondingly reduce, and the boosting efficiency would decrease; *i.e.*, the output voltage ratio of series-connected electrodes device and single electrode device would be smaller than the nominal value.

As noted in the experiments, damping does exist in the operation of the HV generator. Possible damping sources include PZT element itself, polyimide cable, bonding glue and silver epoxy for the device assembly, and bonding glue between the device and the load cell in the experiment. The glue and silver epoxy are hardened after bonding, which reduces their contribution to damping. The damping dissipates mechanical energy applied on the device to some extent; however, because the added layers (polyimide – 75 μm ; glue layers <5 μm) are much thinner than the PZT disk (740 μm), most of the mechanical energy is imparted to the PZT element.

4.4. Conclusions

In Section 4.2, it was noted that the voltage peak in the demonstration experiment reaches as high as 1.35 kV, which is out of the range of characterization shown in Figure 4.9. In further studies, a larger capacity load cell will be used to explore the performance of the HV generator under an even larger input mechanical stress.

In summary, a pulsed high voltage generator utilizing a monolithic PZT51 element (5 mm in diameter and 740 μm) with electrodes series-connected via a flexible polyimide cable was designed, fabricated, assembled and tested. Through experiments on both single-electrode pair device and three-electrode pair HV generator, the voltage boosting strategy of series-connected electrodes pairs on a monolithic PZT element was experimentally validated. The characterization was performed in the pulsed stress range from 1 MPa to 5 MPa and the corresponding peak output voltages were from 100 V to 900 V. The potential applications on microdischarge-based microsystems were demonstrated in further experiments. The HV generator was successfully used to operate a microdischarge based chemical vapor sensor and initiate sparks between a 75- μm gap in sensor electrodes. The peak voltage during the discharge reached 1.35 kV and 34 nC charge was delivered to the sensor. The non-linear piezoelectric effect in transient mode was investigated for the PZT51 element. The results showed that above stress levels of about 2.5 MPa, the effective piezoelectric coefficient d'_{33} increases linearly with the amplitude of the applied stresses in transient mode.

CHAPTER 5:

Conclusions and Future Work

This chapter summarizes the efforts presented in previous chapters, including design, modeling, fabrication and testing of two generations of microdischarge-based pressure sensors targeting for harsh environments, and a miniaturized pulsed high voltage generator using a single bulk PZT51 element for microdischarge initiation. This chapter also places in context the work described in Appendices A and B. These include an effort to use microdischarge-based chemical sensors in gas chromatography, and an assessment of capacitive pressure sensors that are derived from the process for microdischarge-based pressure sensors described in chapter 3. Then, main contributions resulting from the overall effort are outlined. Future work directed at further miniaturization of the second generation microdischarge-based pressure sensor is suggested at the end of the chapter.

5.1. Summary

5.1.1. Microdischarge-Based Pressure Sensor

Two generations of microdischarge-based pressure sensors, which operate by measuring the change of spatial microdischarge current distribution with pressure, have been developed and demonstrated. The spatial discharge current distribution between two current paths formed by three electrodes is described by a normalized differential current $(I_1 - I_2)/(I_1 + I_2)$. The use of this

differential expression minimizes the consequence of absolute energy variation in microdischarge characteristics. Pulsed high voltage is applied to operate the devices, which reduces power consumption and parasitic heating. Aggressive device miniaturization has been achieved: the exterior device volumes of two generations devices are in the order of 0.01 mm^3 , about $30\times$ and $150\times$ smaller than prior work [Wri13]. The device miniaturization has further motivated the explorations of scaling properties of microdischarge and fabrication process: behaviors and characteristics of microdischarge with interelectrode gaps from $10\text{'s } \mu\text{m}$ to $1\text{'s } \mu\text{m}$ have been investigated inside the pressure cavity; two unique microfabrication processes with 3-D lead transfer configurations using through-glass or through-silicon interconnections have been developed. Operation pressure range has been extended to 10's MPa targeting for harsh environments, such as downhole environments for oil exploration.

The first generation microdischarge-based pressure sensor consisted of a deflecting Si diaphragm, a glass substrate, and a discharge cavity defined and sealed by an In-Au eutectic bonding layer. The three electrodes configuration provided two current paths, with one cathode ($K2$) on the silicon diaphragm, and one anode (A) and another cathode ($K1$) on the glass substrate. The overall device size was $0.585\times 0.54\times 0.2 \text{ mm}^3$, with typical interelectrode gaps of $10 \mu\text{m}$. A two-wafer, 6-mask microfabrication process was investigated for device fabrication. Electrode connections to the interior of the chamber were provided by laser drilling and copper electroplating through high aspect ratio glass vias. Microdischarges could be initiated at voltages below 500 V in an Ar filled microdischarge chamber at about 1 atm interior pressure. Further, the peak current levels were at a level of $\approx 10 \text{ mA}$, and pulse durations are $\approx 100 \text{ ns}$, which permits the discharge to remain relatively energy efficient. For an $AK1$ spacing of $10 \mu\text{m}$, the

fractional differential current changed by approximately 20% as $AK2$ changed from 30 μm to 25 μm , corresponding to external pressure changed from 0 to about 40 MPa.

The second generation microdischarge-based pressure sensor consisted of a deformable silicon nitride diaphragm, an oxide insulated silicon substrate, and a surface micromachined cavity. Different from the design of first generation, the three electrodes configuration used multiple anodes and single cathode, to achieve a higher sensitivity of discharge current to the diaphragm deflection. With further miniaturization in both device volume and the interelectrode gaps compared to the first generation, the overall device size was $0.3 \times 0.3 \times 0.15 \text{ mm}^3$ and minimum interelectrode spacing was 3 μm . The sensor was monolithically fabricated using a combination of surface micromachining and TWIST technology. The use of TWIST technology not only solved the general problem of lead transfer from within the sealed cavity, but also facilitated backside contacts for ease of system integration and miniaturization of the device footprint. In addition, TWIST technology was also suitable for high voltage application, withstanding voltages up to 3 kV. Fabricated devices were tested in a gaseous environment in the range of 1–8 atm. Both DC-like and pulsed microdischarges were observed concurrently in $I1$ and $I2$, with breakdown voltage $\approx 250 \text{ V}$. The normalized differential current $(I1-I2)/(I1+I2)$ was monotonically increased from -0.7 to 0.2 with external pressure increased from 1 atm to 8 atm. The plasma impedance reduced with smaller cavity gap at high external pressures. Low intensity steady current was also observed between only K and $A2$ at high pressures ($\geq 5 \text{ atm}$).

5.1.2. Pulsed High Voltage Generator

The pulsed high voltage generator outlined in this work described an avenue to boosting voltage generated by a single piezoelectric element using a pattern of electrode pairs and a connection strategy. The design utilized a monolithic PZT51 element (5 mm in diameter and 740 μm) with three pairs of electrodes deposited on top and bottom surfaces. When the electrode pairs were connected in series via a flexible polyimide cable, output voltage was multiplied roughly by a factor of 3 over a mechanical input from 1 MPa to 5 MPa, compared to a single pair. With transient mechanical load applied from 1 MPa to 5 MPa, the corresponding peak output voltages were experimentally obtained from 100 V to 900 V. The potential for use in microdischarge-based microsystems was demonstrated in further experiments. The HV generator was successfully used to operate a microdischarge based chemical vapor sensor and initiate sparks between a 75- μm gap in sensor electrodes. The peak voltage during the discharge reached 1.35 kV and 34 nC charge was delivered to the sensor. The non-linear piezoelectric effect in transient mode was investigated for the PZT51 element. The results showed that above stress levels of about 2.5 MPa, the effective piezoelectric coefficient d'_{33} increases linearly with the amplitude of the applied stresses in transient mode. Although only the three-pair electrodes configuration was demonstrated experimentally, a design with more pairs of electrodes targeting a higher voltage multiplication can be envisioned based on this strategy, which has been validated by finite element analysis.

5.1.3. Microdischarge-Based Chemical Sensor in Gas Chromatography

The evaluation of microfabricated electrode arrangements on a glass substrate has led to the first demonstration of pulsed microdischarge-based chemical vapor sensors used in conjunction with gas chromatography. A mixture of chemical vapors of acetone, 1-Hexanol, nitro-benzene, with weights of several micrograms, was detected by the microdischarge-based sensor chip and compared with the results from a reference method (flame ionization detector). The microdischarge operated in pulsed mode saves energy consumption and the lifetime of the sensor electrodes. The average power over a 25 mins span was ≈ 1 mW. More details are provided in Appendix A.

5.1.4. A 100- μm Diameter Capacitive Pressure Sensor

The investigation of microfabrication processes for microdischarge-based pressure sensors has led to a low temperature process that can also be used to fabricate ultra-miniature capacitive pressure sensors. The sensor had a $\varnothing 100$ μm diaphragm and a nominal interelectrode gap of 3 μm . The sensor operated in contact mode at the high end of the pressure range, which extended the dynamic range to 50 MPa. Multiphysics FEA was performed to investigate capacitance-pressure characteristics of contact mode operation. With the use of TWIST technology, the device had a small footprint of 150×150 μm^2 . Fabricated sensors with diaphragm thicknesses of 3 μm (*C100t3*) and 5 μm (*C100t5*) were successfully tested in an oil environment up to 20 MPa and 50 MPa, respectively. The average sensitivities were 7,200 ppm/MPa (3.1 fF/MPa) for *C100t3*, and 3,400 ppm/MPa (1.6 fF/MPa) for *C100t5* in the non-contact mode. In the contact mode, the average sensitivities were 9,900 ppm/MPa (5.3 fF/MPa)

for *C100t3*, and 3,100 ppm/MPa (1.6 fF/MPa) for *C100t5*. More details are provided in Appendix B.

5.2. Contributions

The main contributions of this work include:

1. First demonstration of monolithically microfabricated microdischarge-based pressure sensor with deflecting diaphragm in two generations of design and fabrication.
2. Successful demonstrations of both two-cathode/one anode and two-anode/one cathode differential operation of microdischarge-based pressure sensors.
3. Investigation of scaling behaviors and characteristics of spatial microdischarge distribution in a $\varnothing 200$ μm cavity between competing electrode pairs with interelectrode gaps from 10 μm to less than 3 μm , an order of magnitude smaller than prior work [Wri13]
4. A unique two-wafer 6-mask microfabrication process with metal filled through-glass vias, providing 3-D electrical feedthrough from inside cavity to device outside with high insulation strength.
5. The TWIST technology is the first demonstration of lead transfer for microfabricated devices using oxide-isolated heavily doped bulk-silicon islands with high insulation strength (>3 kV), offering approaches to easy of system integration and device miniaturization.
6. A successful demonstration of the application of TWIST technology by the investigation of a 100- μm diameter capacitive pressure sensor.

7. A unique strategy for voltage boosting using piezoelectric materials, with a demonstration of microdischarge initiation (>1 kV) in a microdischarge-based chemical sensor from the proposed HV generator.
8. An experimental observation of the non-linear piezoelectric effect in transient mode from bulk PZT51 elements; the effective piezoelectric coefficients increased linearly as the applied stress increased within the range of 1–5 MPa.

5.3. Future Work

One of many advantages of microdischarge-based pressure sensor is the dimensional scalability, due to the large inherent signal. Further miniaturization can be achieved in future work. In addition, the pressure range can be extended up to 50 MPa based on the configuration of the second generation microdischarge-based pressure sensors, with a careful selection of dimensions.

A parametric study, using FEA in COMSOL® version 4.3, was conducted to assess the options for the diaphragm design for the further miniaturization (Figure 5.1). For this study, three pressure ranges were selected: 0–10 MPa, 0–30 MPa, and 0–50 MPa. Given a pressure range, cases were then divided by different safety margins according to the fracture strength of the diaphragm materials (*i.e.*, low stress silicon nitride). Then, the thickness and diameter of the diaphragm were swept over a selected range. The resulting maximum deflection at the center of diaphragm was compared with the height of discharge chamber.

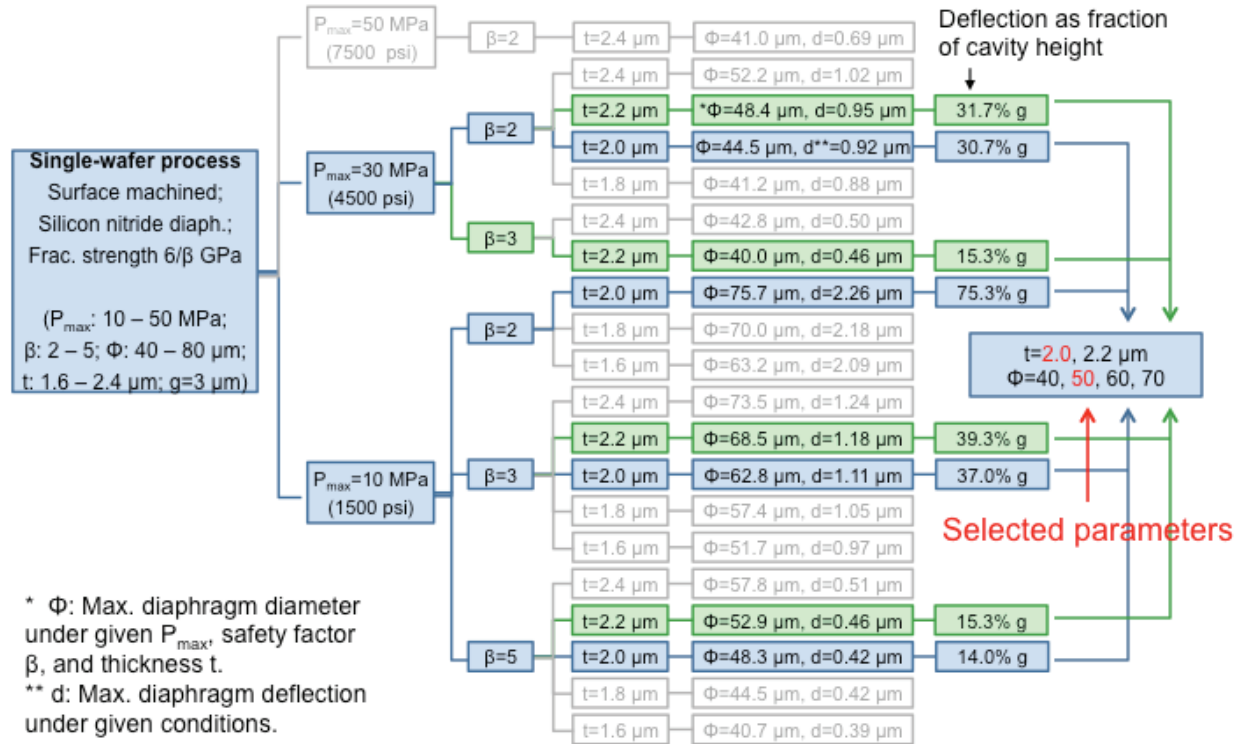


Figure 5.1: Parametric study for dimensional selection using finite element analysis.

The parametric study summarized in Figure 5.1 suggests that combinations of diameters ranging from 40 μm to 70 μm and thicknesses from 2 μm to 2.2 μm are the most suitable. Further FEA study was performed by sweeping the pressure from 0 to 50 MPa for a given selection of dimensions. The maximum deflection of the diaphragm was obtained, as well as the maximum pressure that could be applied for different safety margins (Table 5-1). Following the evaluations of multiple combinations of thickness and diameter, the final dimensions of the diaphragm of one of the primary devices were set at 2 μm thickness and 50 μm diameter, as highlighted in Table 5-1.

The maximum von Mises stress and corresponding diaphragm deflection under applied external pressure for the selected $\phi 50$ μm design are plotted in Figure 5.2. It was found that this

diaphragm can operate at external pressures up to 25 MPa with safety factor >2 , and deflection $\approx 1 \mu\text{m}$. The schematic of proposed design with exterior dimensions is shown in Figure 5.3.

Table 5.1: Further FEA parametric study results, selected dimensional design is highlighted.

Φ (μm)	t (μm)	$\beta=5$		$\beta=3$		$\beta=2$	
		P_{max} (MPa)	d_{max} (μm)	P_{max} (MPa)	d_{max} (μm)	P_{max} (MPa)	d_{max} (μm)
40	1.8	12.9	0.34	21.5	0.55	32.2	0.81
	2	15.5	0.31	25.9	0.50	38.8	0.75
	2.2	17.6	0.28	29.8	0.46	45.1	0.68
50	1.8	7.5	0.46	13.2	0.79	20.0	1.18
	2	9.2	0.43	15.6	0.71	23.4	1.05
	2.2	11.3	0.41	18.9	0.66	28.3	0.98
60	1.8	5.0	0.62	9.2	1.11	13.8	1.66
	2	6.2	0.58	11.1	1.01	16.7	1.50
	2.2	7.6	0.55	13.1	0.92	19.6	1.36
70	1.8	3.5	0.79	6.4	1.41	10.0	2.18
	2	4.2	0.72	7.7	1.27	11.8	1.93
	2.2	5.3	0.68	9.5	1.21	14.3	1.80

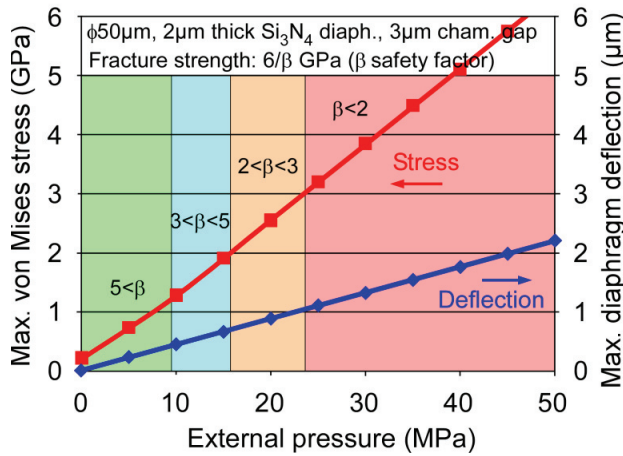


Figure 5.2: Maximum stress and diaphragm deflection under applied external pressure for selected parameters. Different safety margins are highlighted.

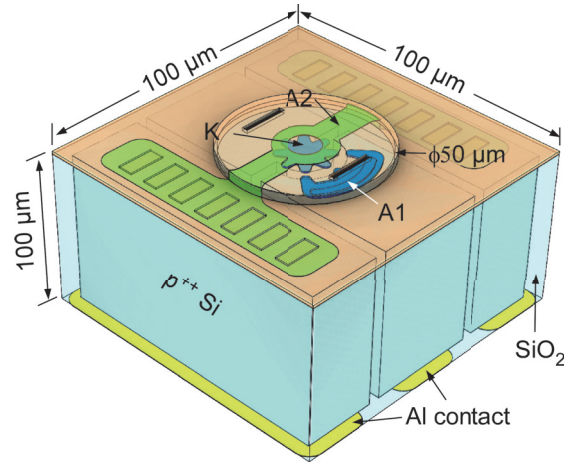


Figure 5.3: Schematic of the proposed design with further reduction in device volume, targeting a pressure range up to 50 MPa.

In addition, when dimensions are further scaled down, the sharpness of the plasma localization feature increases, which can enhance the local electric field. The enhanced electric field may lead to a field emission dominant discharge, which may reduce the sensitivity of the

discharge current to diaphragm deflection. Therefore, necessary geometric modifications of electrodes need to be considered in the design of further miniaturized devices.

Looking forward, inspired by the investigation of the 100- μm diameter capacitive pressure sensor presented in Appendix B, more applications that benefit from the TWIST technology can be envisioned, such as microphones.

APPENDICES

APPENDIX A:

**An Application of A Microdischarge-Based Chemical Sensor
in Gas Chromatography**

There is an increasing interest in miniaturized systems for chemical analysis in harsh environments. Chemical detection by emission spectroscopy of on-chip microdischarges [Eij00, Mit09a, Mit08b] can be performed at temperature exceeding 200°C [Wri09b], suggesting utility inspace exploration, volcanic monitoring, and oil well monitoring. This chapter describes the first use of pulsed microdischarge spectroscopy for gas chromatography (GC) [Luo11]. This effort supports NASA interests in monitoring closed-loop life support systems for spacecraft.

A.1. Introduction

With an increasing interest in chemical analysis, especially for environmental monitoring in harsh environments, a variety of miniaturized chemical detectors have been explored. Chemiresistor is the simplest technology to sense chemical compounds for miniaturized chemical sensor, with advantages of compact size, simple fabrication, low cost, and simple measurement electronics; whereas, it suffers from noise, drift, aging and sensitivity to environmental parameters [Wil01]. Chemiresistor belongs to one type of thin film sensor. The chemical vapor under test is absorbed by the thin film and the analyte concentration is proportional to the resistance of the thin film. Another class of sensor technology, the

potentiometric CHEMFETs, are more complex solid-state sensors. Unlike MOSFET, the threshold voltage is chemically modulated. Although this type of chemical sensor does not exhibit many of the fluctuations and instability of the chemiresistor, it also requires more complex signal processing. Several other solid-state chemical sensors are also practical for portable instruments, such as surface acoustic wave, bulk acoustic wave, etc. The chemical sensing could also be achieved using an optical way, the surface plasmon resonance-based sensor, which is capable of using a white light source as its optical input and use highly integrated compact optics for output signal measurements [Wil01].

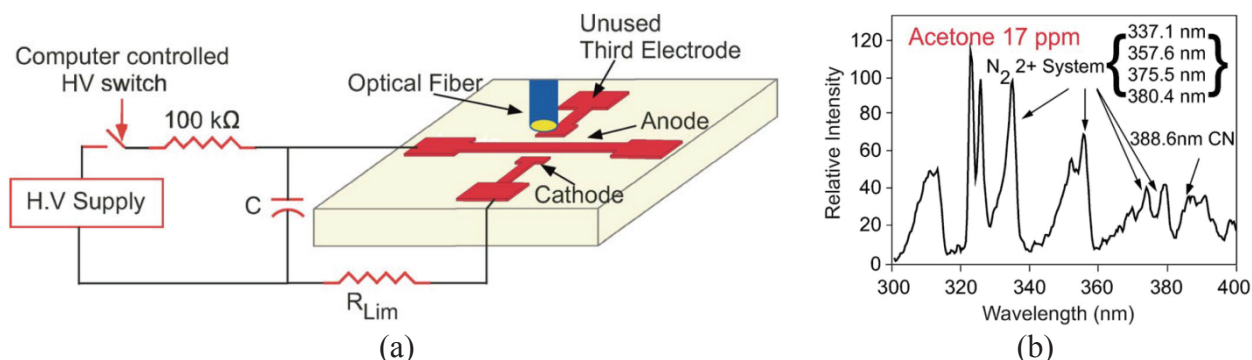


Figure A.1: One example of the optical emission spectroscopy from microdischarges for chemical vapor sensing using pulsed DC microdischarge. (a) Schematic of the sensor and experimental setup. (b) A typical spectrum obtained in an acetone environment, readout from the spectrometer [Mit08b].

Optical emission spectroscopy from microdischarge has been demonstrated as a rapid method to sense a large number of chemicals [Eij00, Mit08a, Mit08b]. One of those examples is provided in Figure A.1 [Mit08b]. These devices operate by exciting gas species using microdischarges and observing the characteristic spectral output from the energy transitions. Since most atomic species have their specific emission lines, emission spectroscopy can be used to identify numerous species concurrently without adding additional devices. For the operation, the microdischarge can be driven by either continuous DC [Eij00], or pulsed DC [Mit08a, Mit08b] which aims at lower power consumption. In an extended application, the

microdischarge-based chemical sensor has been integrated in gas chromatography (GC), using a continuous DC discharge [Eij00].

This work studies the use of a microdischarge-based thin film chemical vapor sensor, driven by pulsed DC, in a GC system.

A.2. Device Concept, Design and Fabrication

The microdischarge chip for chemical vapor detections includes a $1 \times 1 \text{ cm}^2$ glass chip, on which thin-film Ni electrodes are patterned with an anode-cathode gap of $160 \text{ }\mu\text{m}$. A glass lid with cross-shaped grooves ($500 \text{ }\mu\text{m}$ wide, $500 \text{ }\mu\text{m}$ deep) and inlet/outlet capillary tubes (ID $250 \text{ }\mu\text{m}$) are epoxy-sealed to the chip, as shown in Figure A.2. The assembly is then clamped in a chip holder that provides electrical and optical interfaces.

For the operation, in plane microdischarges will be initiated when the applied voltage across the anode and cathode exceeds breakdown voltages. External circuits are tailored by adjusting the ballast resistors to keep the microdischarge working in a glow discharge state. The microdischarge excites the gas molecules and breaks the chemical bonds. As a result of the energy transition from different energy levels, specific characteristic emissions at certain wavelengths for each chemical species are produced. Then the emission spectra from the microdischarge are captured by a spectrometer through an optical lens and fiber and exported for analysis. In general, each chemical species has its own characteristic emission profile. Therefore, this is a promising and general approach for chemicals detection.

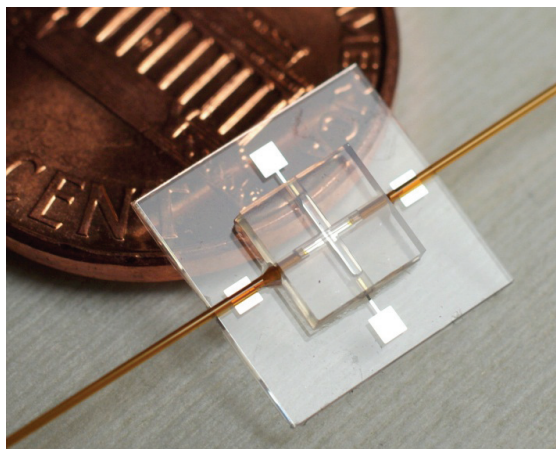


Figure A.2: The assembled chemical detector with a glass lid and inlet/outlet capillary tubes, against with a U.S. penny.

A.3. Experimental Results

Figure A.3 shows the schematic of the experimental setup for the sensor tests in a GC system. The microdischarge chip is connected at the downstream end of the 1.7 m-long, RTX-1-coated GC separation column. The emission signals are read by a USB-connected portable spectrometer. Chemicals under tests are injected in the GC, and carried by helium gas. Helium gas is widely used as the carrier gas in GC system, because it only has a few characteristic emission lines compared to air, which minimizes the background noises for analysis. Mixture chemical vapors are separated by the GC column, and come out separately in time domain. Then the separated chemicals come into either the commercialized flame ionization detector (FID) for reference or to the microdischarge-based chemical vapor sensor, controlled by valves.

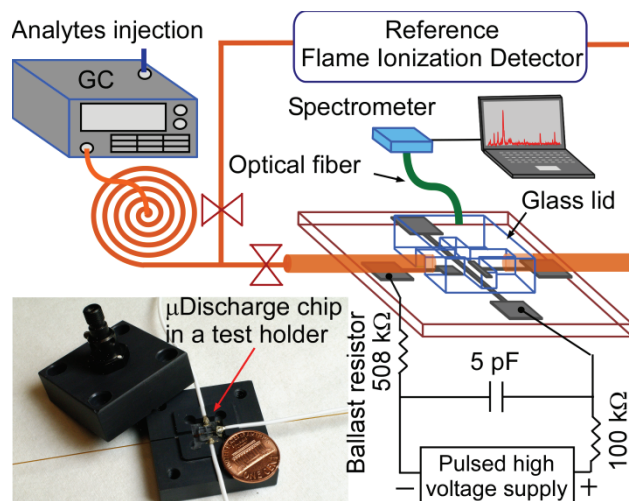


Figure A.3: Schematic of the sensing system.

In the experiments, a mixture of acetone 3.6 μg , 1-hexanol 2.8 μg and nitrobenzene 3.0 μg , was injected, with He carrier gas at 1.56 sccm, through the GC. For this, Acetone elutes quickly while nitrobenzene is slower. Voltage pulses (1100 V, 5 ms) were applied – at 0.5 Hz during the first 6 minutes, and 0.04 Hz after that – to reduce the power consumption.

A representative spectrum obtained when the acetone passed through the detector is shown in Figure A.4. The spectrum shows that the 388 nm peak, representing CN/CH fragments [Pea50], is enhanced by carbon compounds. Its strength relative to the 588 nm peak of He provides a data point in the chromatogram. Figure A.5 shows the chromatograms of one set of detection, with a benchmark result from FID. The differences in elution time are attributed to differences in the gas flow paths for the two detectors [Eij00].

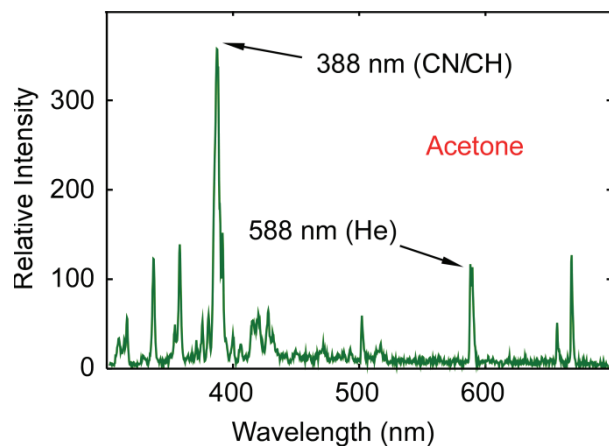


Figure A.4: A typical spectrum obtained when the acetone passed by the detector.

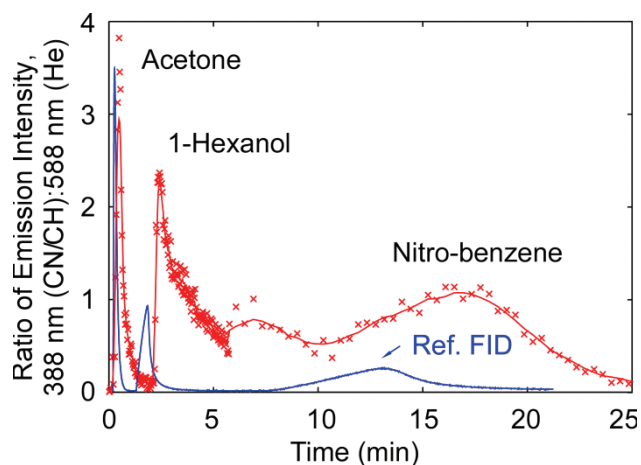


Figure A.5: Chromatograms obtained from the microdischarge response, and compared with the results from reference FID.

The current peak at each microdischarge was 1.42 mA, which corresponds to 7.8 mJ per discharge consumed. In this set of detection, 220 pulses were struck over 25 minutes; the average power was 1.14 mW.

The sensor has been tested with more than 500 pulses without any electrode crack.

A.4. Conclusion

This work presents the application of a pulsed microdischarge-based chemical vapor sensor in a GC system. A mixture of chemical vapors of acetone, 1-Hexanol, nitro-benzene, with weights of several micrograms, was detected by the microdischarge-based sensor chip and compared with the results from FID. The microdischarge operated in pulsed mode saves energy consumption and the lifetime of the sensor electrodes. The average power over a 25 mins span was ≈ 1 mW.

APPENDIX B:

A 100- μm Diameter Capacitive Pressure Sensor with 50 MPa Dynamic Range

This appendix presents a fully sealed absolute capacitive pressure sensor for high pressure hydraulic applications. The sensor has a $\varnothing 100\ \mu\text{m}$ diaphragm and a nominal interelectrode gap of $3\ \mu\text{m}$. The interior cavity is electrically isolated, allowing the sensor to operate in contact mode at the high end of the pressure range, at which the interelectrode gap is closed. Multiphysics finite element analysis is performed to investigate capacitance-pressure characteristics of contact mode operation. The sensor is monolithically fabricated using a combination of surface micromachining and through-wafer isolated bulk-silicon lead transfer that facilitates backside contacts for ease of system integration and miniaturization of the device footprint, which is $150\times 150\ \mu\text{m}^2$. Fabricated sensors with a diaphragm thickness of $3\ \mu\text{m}$ (*C100t3*) and $5\ \mu\text{m}$ (*C100t5*) are successfully tested in an oil environment up to 20 MPa and 50 MPa, respectively. The average sensitivities were 7,200 ppm/MPa (3.1 fF/MPa) for *C100t3*, and 3,400 ppm/MPa (1.6 fF/MPa) for *C100t5* in the non-contact mode. In the contact mode, the average sensitivities were 9,900 ppm/MPa (5.3 fF/MPa) for *C100t3*, and 3,100 ppm/MPa (1.6 fF/MPa) for *C100t5*.

B.1. Introduction

Providing high performance, small size and low cost, microfabricated pressure sensors are widely used in automotive systems, healthcare, industrial process control and consumer

applications. Microfabricated pressure sensors represent one of the largest segments of the entire industry of microelectromechanical systems (MEMS) with sales worth \$2.1B in 2013. Analysts forecast that the global MEMS pressure sensor market will grow at a compounded annual growth rate (CAGR) of 8.2 percent over the period 2014-2019 [Yol14].

Among a variety of micromachined pressure sensors that have been investigated [Gia06] including piezoresistive [Sam73], capacitive [He07], optical [Abe02], resonant-beam [Mel01] and microplasma-based [Eun14], capacitive pressure sensors are known to provide high sensitivity, low temperature coefficients, low noise and low power consumption [Gia83, Wan97, Aka01, Cha01, Par03, Haq10]. A variety of challenges and considerations are faced in the design of microfabricated capacitive pressure sensors, including the formation of a sealed cavity, lead transfer from inside the cavity, device miniaturization and system integration [Cha01].

To form a sealed pressure chamber, two major approaches have been widely used: bulk micromachining combined with wafer bonding, and surface micromachining using sacrificial layers. In the bulk micromachining approach, which inevitably requires multiple wafers, an impurity-based or other etch stop is used to form the cavity together with a sensing diaphragm; the cavity is then sealed by anodic bonding or other means to an opposing substrate [Gia83, Wan97, Aka01, Cha01, Par03, Haq10]. The electrode lead can be transferred laterally through the rim of the cavity to pads located beside the diaphragm [Cha01, Par03] or through glass vias (TGVs) to the backside of the structure [Gia83, Wan97, Haq10]. In the surface micromachining approach, which requires only one wafer, sacrificial materials such as phosphosilicate glass (PSG) [Guo00], silicon oxide [Mas96], or metal [Nar13], are used to define the cavity. After depositing the diaphragm layers, the sacrificial layer is typically removed by wet etching. Dry etching can be used for structures where wet etchant access is a challenge [An14]. The lead transfer for this

approach is typically through the diaphragm layers, and is positioned beside the cavity on the upper surface of the substrate. *A single wafer approach with backside contacts using through-silicon vias (TSVs) would allow greater miniaturization.*

In recent years, through-wafer lead transfer technology has received significant attention from the electronics industry [Ant81, Li02, Spi05, Koy09, Gu09, Suk12], because three-dimensional interconnections reduce the wiring length, parasitics, chip size and power consumption. Additionally, more chips can be stacked within a compact package using this technology, for added functionality and performance. Typically, TSVs [Spi05, Koy09, Gu09] are formed by filling deep trenches in silicon substrates with heavily doped poly-Si or metal using low-pressure chemical vapor deposition (LPCVD) or electroplating, after the surface of the silicon trench is thermally oxidized. The silicon trenches are formed by deep reactive-ion etch (DRIE). In contrast, TGVs [Ant81, Li02, Suk12] are laser drilled, followed primarily by electroplating with different metal and plating conditions. An increasing number of commercialized MEMS products from companies such as STMicroelectronics, Bosch and mCube are now taking advantage of this technology to miniaturize the entire package together with application-specific integrated circuits (ASICs) [Yol14].

Normally a capacitive pressure sensor is operated over a dynamic range within which the diaphragm does not come into contact with the substrate, i.e., the maximum deflection of the diaphragm is smaller than the cavity height. In this dynamic range the sensor provides a non-linear response that is inversely proportional to the interelectrode gap. There is a natural compromise between the sensitivity and dynamic range because a smaller initial gap provides a higher sensitivity, but lowers the dynamic range. By adding an insulation layer between two electrodes, a capacitive pressure sensor can be operated in the contact mode, which allows the

diaphragm to touch the substrate. The dynamic range is extended to a region beyond the initial contact pressure [Cho92, Wan99]. In the contact mode, the capacitance increases due to progressive increase in contact area between the diaphragm and substrate when the external pressure increases. The contact mode operation provides one or two orders of magnitude higher sensitivity than the region in which near linear operation can be obtained in non-contact mode [Wan99]. Other advantages include a good linearity in the contact range and overload protection. Thus, contact mode capacitive pressure sensors are advantageous for high pressure environments that require a large dynamic range and mechanical robustness.

This chapter describes a 100- μm diameter, monolithically fabricated, contact mode capacitive pressure sensor for high pressure hydraulic applications that is intended for integration in a submillimeter package [Ma14]. Performance targets are selected for downhole environments encountered in oil exploration and production. Overall, the targets include a sensor footprint on the order of 0.01 mm^2 , backside contacts for surface mounting and a chip stack, and a dynamic range of 50 MPa. The device is fabricated by a surface micromachining technique that incorporates through-wafer isolated bulk-silicon lead transfer for backside contacts, allowing aggressive miniaturization. The fabricated capacitive pressure sensors with $\text{\textcircled{1}}100\text{ }\mu\text{m}$ diaphragm have a footprint of $150\times 150\text{ }\mu\text{m}^2$.

B.2. Device Concept and Modeling

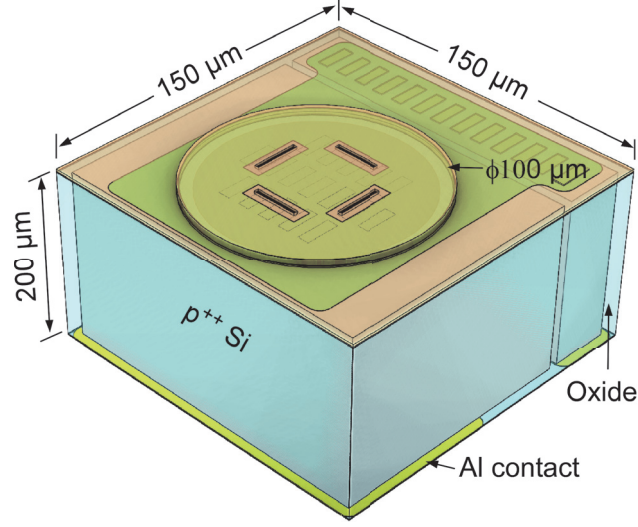
B.2.1. Device Concept

The sensor (Figure B.1) primarily consists of a deformable diaphragm with a top electrode, a circular vacuum-sealed cavity, and an oxide insulated silicon substrate with a bottom

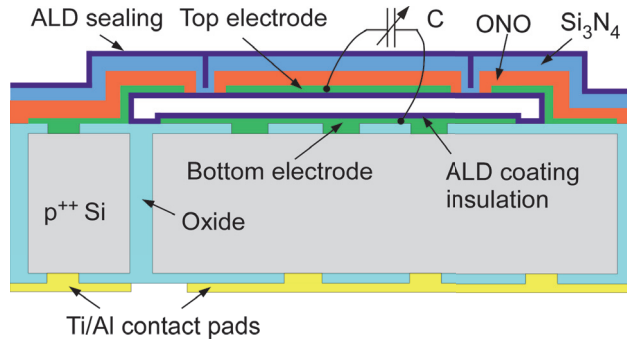
electrode. The two electrodes are separated by a nominal gap of the cavity height and form a capacitor. Surfaces of both electrodes that face the cavity are coated with a thin layer Al_2O_3 , which enables the device to operate in contact mode. The capacitance in contact mode is primarily determined by the combined thickness of the insulation layers between two electrodes and the area in contact. Because this insulation layer is typically very thin compared to the height of the cavity, the capacitance per unit area is much larger than that of the untouched area. As shown in Figure B.1b, both electrodes are electrically routed to backside contact pads through the heavily doped silicon substrates. Individual silicon substrate islands are separated and insulated by silicon oxide. In this configuration, the contact pads do not increase the overall device size. In addition, the backside contacts allow surface mounting and chip stacking in the third dimension, eliminating the need for wire bonding in system integration.

B.2.2. Modeling of Contact Mode Pressure Sensors

Finite element analysis (FEA) is performed using COMSOL Multiphysics® version 4.4 to study the capacitive response to external pressure changes. The *MEMS Electromechanics* module in this software provides a dedicated interface to capacitive sensor and actuator simulation, by combining a conventional *Solid Mechanics module*, an *Electrostatic Module* and a *Moving Mesh* method. Different from a two-step approach that separately calculates deformation and capacitance [Wan99], this coupled simulation directly provides capacitance change with applied pressure in the non-contact mode. The disappearance of the interelectrode gap in contact mode simulations can be accommodated by making two modifications. First, the dielectric layer of Al_2O_3 coated on electrodes is geometrically defined as a part of the cavity



(a)



(b)

Figure B.1: A schematic of the capacitive pressure sensor. (a) 3-D view of the sensor, with dimensions labeled. (b) A cross section view of the sensor.

region (Figure B.2), but it is differentiated from the vacuum by defining a different relative permittivity, as expressed in Eq. (B.1):

$$\epsilon_{2-cavity} = \begin{cases} \epsilon_{vacuum} = 1, & g_i \leq z < g_a \\ \epsilon_{Al_2O_3} = 9.1, & 0 < z \leq g_i \end{cases} \quad (B.1)$$

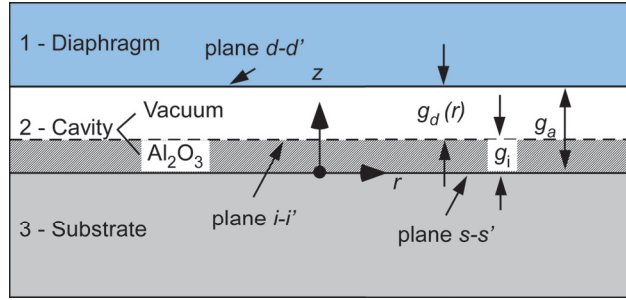
where $\epsilon_{2-cavity}$ is the relative permittivity of the cavity in this model, ϵ_{vacuum} and $\epsilon_{Al_2O_3}$ are the relative permittivity of vacuum and Al_2O_3 , respectively. In the coordinate system (Figure B.2a),

the vertical direction is denoted by z , while the radial direction is denoted by r . The terms g_i and g_a represent the thickness of Al_2O_3 and the initial cavity gap, respectively. Second, to limit the diaphragm deflection, a distributed contact force f_d is added as a boundary condition on the lower side of the diaphragm, which is given by:

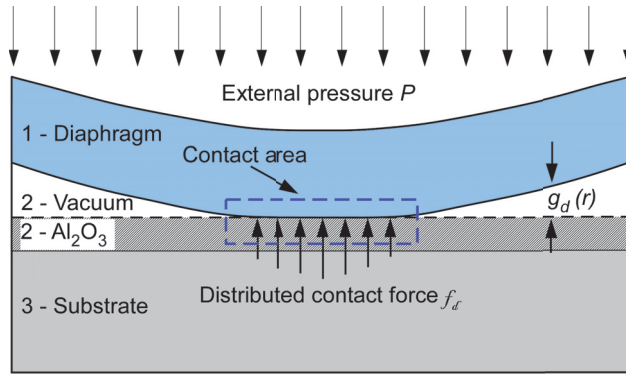
$$f_d = \begin{cases} 0, & 0 \leq g_d(r) < g_a \\ -k_{\text{Al}_2\text{O}_3} \cdot g_d(r) + f_0, & g_d(r) < 0 \end{cases} \quad (\text{B.2})$$

$$k_{\text{Al}_2\text{O}_3} = 10 \cdot \sqrt{P} \quad (\text{MPa/nm}) \quad (\text{B.3})$$

where $g_d(r)$ is the gap between the diaphragm and the insulation layer, and it is a function of position parameter r . The term $k_{\text{Al}_2\text{O}_3}$ is the spring constant of the insulation layer, which is defined as a function of external pressure P (MPa). The Eq. (B.2) is an empirical expression in the simulation and does not necessarily describe an exact relation between $k_{\text{Al}_2\text{O}_3}$ and P ; it is only needed to facilitate convergence during the numerical computation. The term f_0 is a constant, which also facilitates numerical computation without impairment of the rationality of the physics. In this study, 0.5 MPa is selected for f_0 . From Eq. (B.2), it is evident that the contact force f_d exists only when $g_d(r)$ is negative from a mathematical perspective, or when contact occurs from a physical perspective. It is also evident from Eq. (B.3) that $k_{\text{Al}_2\text{O}_3}$ is a relatively large number, which limits the penetration of the diaphragm into the insulation layer to 1–2 nm. With above two customized settings, this module can directly solve the contact mode problem.



(a)



(b)

Figure B.2: Schematic diagrams of the FEA model, dimensions are not to scale. (a) Initial state. (b) With external pressure P applied, the diaphragm contacts the substrate, and a distributed contact force f_d is added to simulate contact-mode operation.

Table B.1: Parameters used in the simulation. Nominal values are used unless noted otherwise.

Parameters	<i>C100t3</i>	<i>C100t5</i>
Diaph. Diameter (μm)	100 \pm 5	100 \pm 3
Diaph. thickness (μm)	3 \pm 0.3	5 \pm 0.5
Cavity height (μm)	3 \pm 0.3	3 \pm 0.3
Diaph. Young's modulus (GPa)	160 \pm 16	160 \pm 40
Diaph. residual stress (MPa)	60	60
Pressure range (MPa)	0–20	0–50

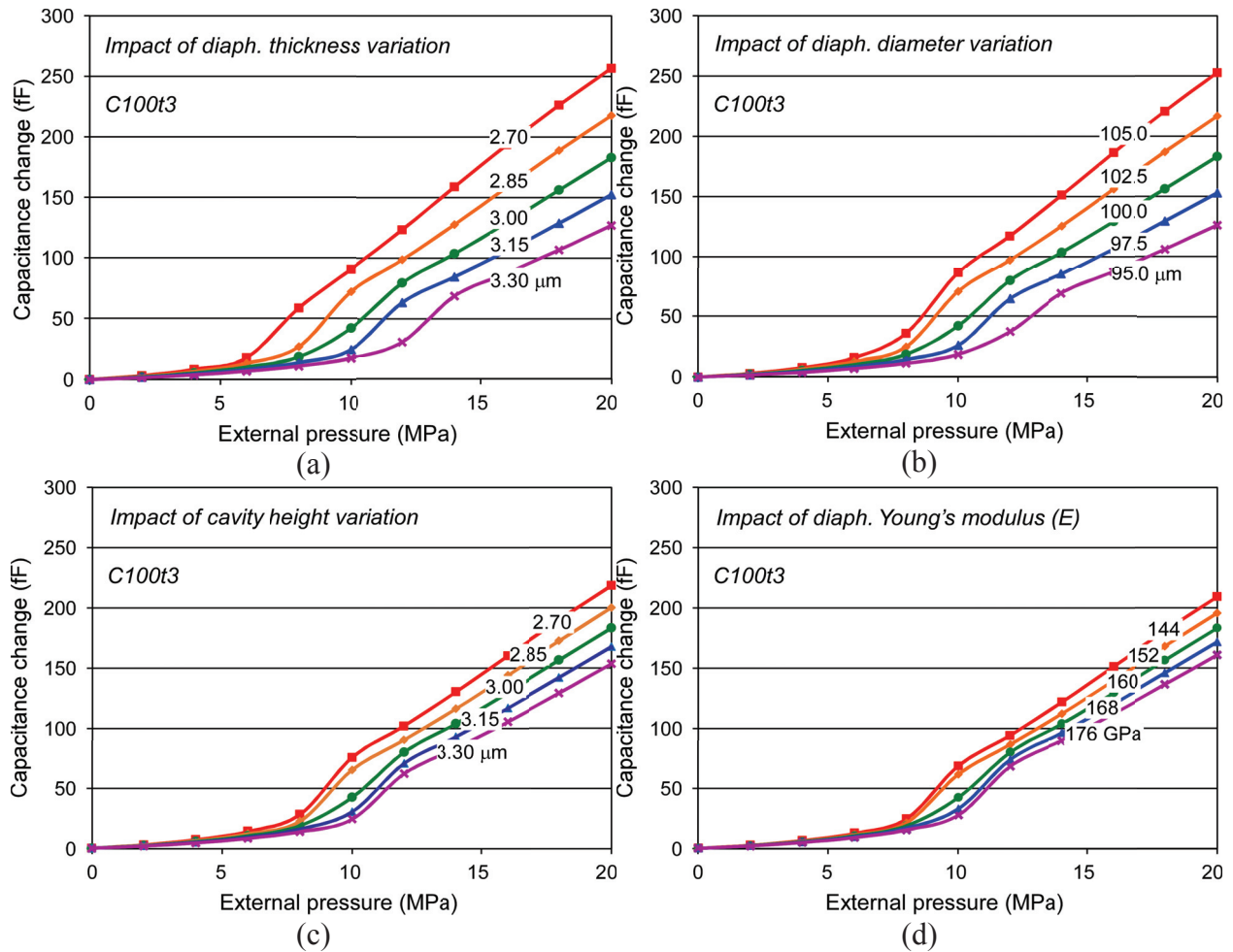


Figure B.3: Modeling results of *C100t3*: Impacts of individual parameter variation on capacitive response to external pressure from finite element analysis in COMSOL. (a) Impact of diaphragm thickness variation. (b) Impact of diaphragm diameter variation. (c) Impact of cavity height variation. (d) Impact of diaphragm Young's modulus variation.

The nominal capacitance C_0 , including contributions from the substrate, contact pads, etc., was simulated by a 3-D model. The nominal capacitance C_0 obtained was 412.9 fF, including all parasitic and fringe influences. A 2-D axisymmetric model can be used to reduce computational time for the study of capacitance-pressure (C - P) characteristics, due to the axial symmetry of a circular diaphragm. In the 2-D axisymmetric simulation, two designs with 100 μm diameter and thickness of 3 μm (*C100t3*) and 5 μm (*C100t5*) were studied. Parameters used in the simulation are listed in Table B.1. Mechanical properties of the diaphragm, including Young's modulus, Poisson's ratio and residual stress, were obtained from both experimental data and references

[Hua06]. Pressure sweeps of 0–20 MPa for *C100t3* and 0–50 MPa for *C100t5* were simulated. The impact of variations in diaphragm thickness, diameter, cavity height, residual stress and the Young’s modulus of the diaphragm, were systematically investigated.

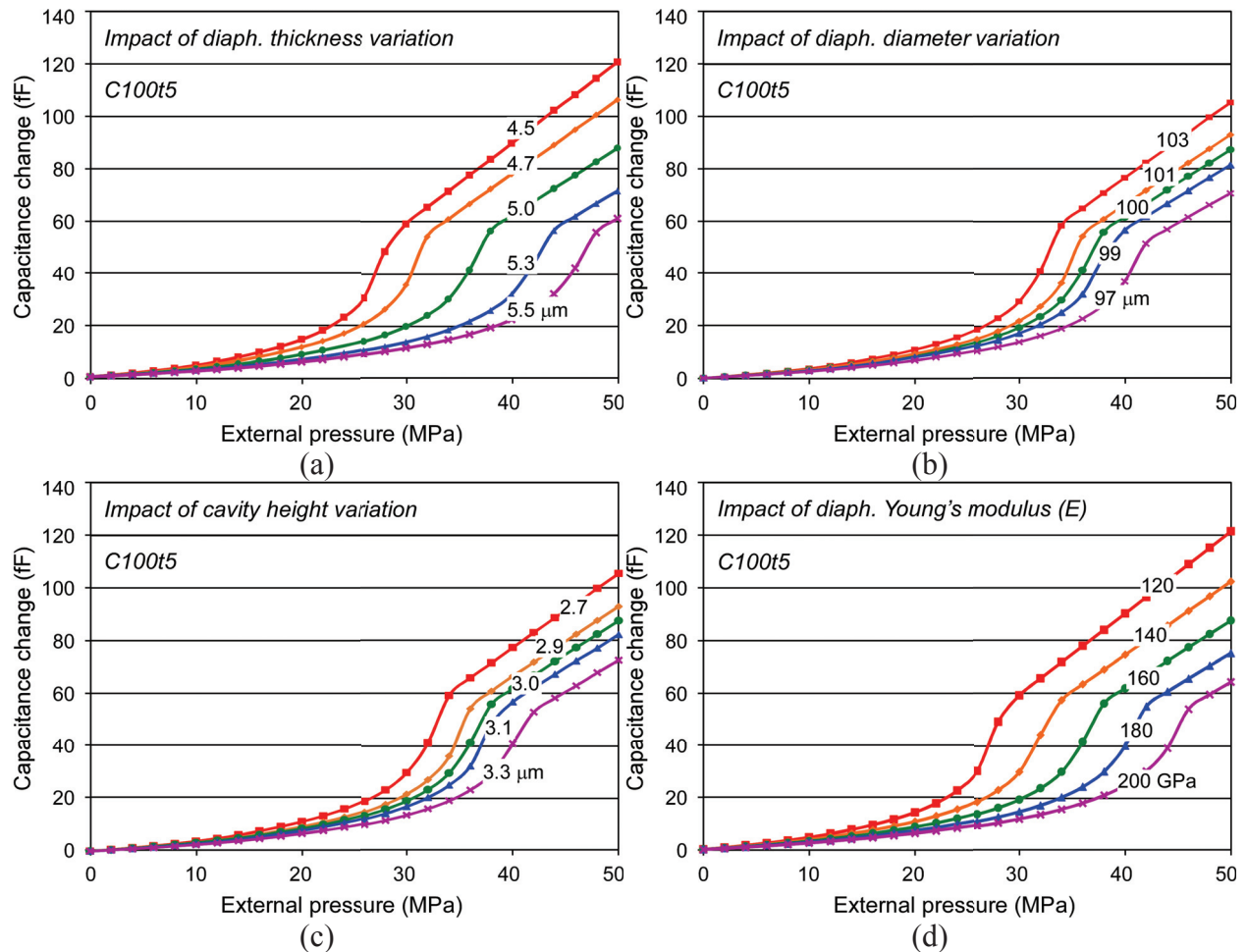


Figure B.4: Modeling results of *C100t5*: Impacts of individual parameter variation on capacitive response to external pressure from finite element analysis in COMSOL. (a) Impact of diaphragm thickness variation. (b) Impact of diaphragm diameter variation. (c) Impact of cavity height variation. (d) Impact of diaphragm Young’s modulus variation.

A study of the geometric parameters and the Young’s modulus of the diaphragm is shown in Figure B.3–B.4. The simulated *C-P* characteristics were in agreement with a typical response from a contact mode capacitive pressure sensor reported in the past [Wan99]. Further analyses on different regions, sensitivity and full scale swing, can be studied and obtained from these

plots. As an example, an analysis of impact of the diaphragm thickness variation is summarized in Table B.2.

Table B.2: Impact of selected diaphragm thickness variation on sensitivity for *C100t3* and *C100t5* based on FEA results.

Parameters	<i>C100t3</i>			<i>C100t5</i>		
Diaph. thickness (μm)	2.7	3.0	3.3	4.5	5.0	5.5
Non-contact mode						
Quasi-linear region (MPa)	0–6	0–8	0–10	0–20	0–28	0–36
ppm/MPa	6,900	5,500	4,200	1,700	1,400	1,100
fF/MPa	3.0	2.3	1.8	0.7	0.6	0.5
Contact-mode						
Linear region (MPa)	8–20	12–20	14–20	30–50	38–50	
ppm/MPa	29,200	23,900	19,000	6,100	5,400	N/A
fF/MPa	16.7	13.0	9.7	3.1	2.6	

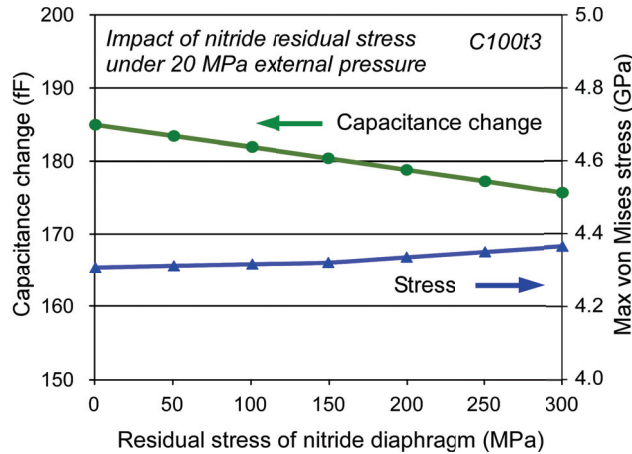


Figure B.5: Impacts of residual stress of nitride diaphragm on capacitive response and maximum von Mises stress under 20 MPa external pressure from finite element analysis of *C100t3*.

The influence of the residual stress in diaphragm materials was also considered. Although the fabrication process used in this effort was designed to provide a residual stress of ≈ 60 MPa (tensile) in the diaphragm materials, a broad range of 0–300 MPa tensile stress was examined in the simulation (Figure B.5). Under 20 MPa applied pressure, the variation of capacitance change over the given range of stress was about 5%.

The impact of combined variation of diaphragm diameter and thickness is illustrated in Figure B.6a. The pressure applied to the diaphragm is fixed at 20 MPa, and both parameters are changed concurrently. Contours of capacitance change, projected to the diameter-thickness plane, indicate discrete values of capacitance change with certain combinations of diameter and thickness of the diaphragm. This study is useful to analyze experimental results from a fabricated device. For example, in the experiment which will be described in Section B.4, the total capacitance change from atmospheric pressure to 20 MPa for the *C100t3* design was experimentally measured at 140 fF. If dominant variations are assumed from the diaphragm thickness and diameter, then a possible combination of these two parameters from a fabricated device will fit in the 140 fF contour curve. Similarly, the impact of a combined variation of thickness and Young's modulus of the diaphragm is shown in Figure B.6b. A more sophisticated study that considers the combined variation of three or more parameters can be envisioned, but its complexity is beyond the intended scope of this work.

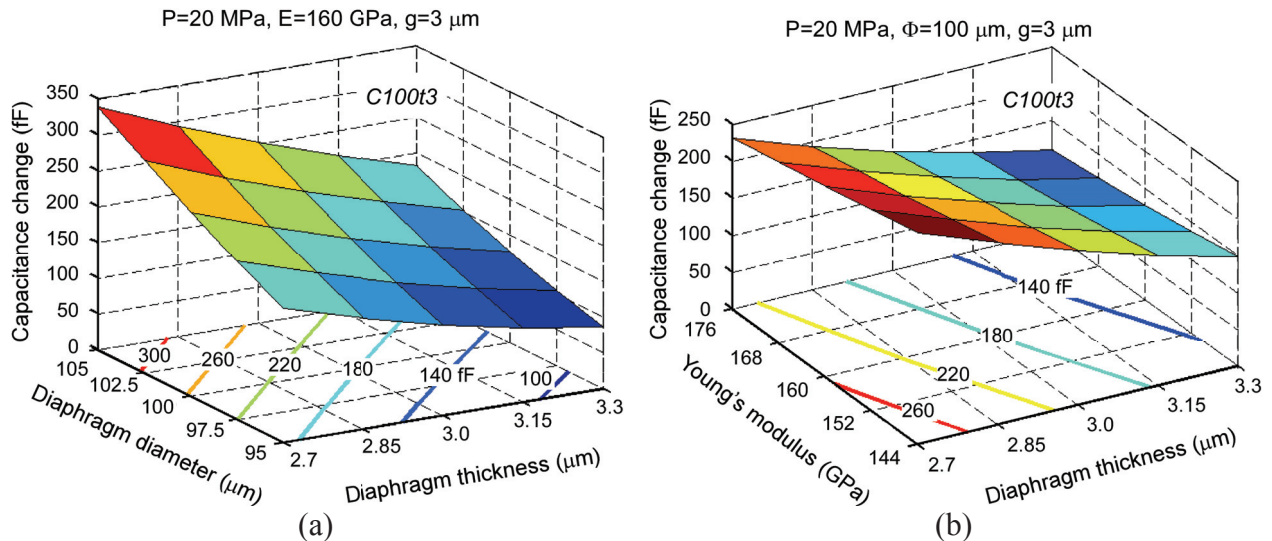


Figure B.6: Simulated impact of coupled parameter variations on capacitance change for 20 MPa applied pressure on *C100t3*. Contours indicate discrete values of capacitance change obtained from changes of (a) diaphragm diameter and diaphragm thickness, and (b) Young's modulus of diaphragm material and diaphragm thickness.

B.3. Fabrication

The 8-mask fabrication process (Figure B.7) utilizes low resistivity ($<0.005 \text{ } \Omega\text{-cm}$) p^{++} silicon wafers. The first mask defines deep reactive ion etch (DRIE) insulating channels with $4 \text{ } \mu\text{m}$ wide and $250 \text{ } \mu\text{m}$ deep features. The resulting trenches are fully filled with thermally grown SiO_2 and tetraethyl orthosilicate (TEOS) oxide. The wafers are then thinned by lapping and chemical mechanical polishing (CMP) both sides, which provides a flat, mirror surface finish. The final thickness was about $200 \text{ } \mu\text{m}$, but it can be thinner if necessary. After polishing, silicon oxide is deposited on both sides by plasma-enhanced chemical vapor deposition (PECVD) and patterned by reactive-ion etching (RIE) to provide contact vias for metal features using the second and third masks. Metal layers, including bottom electrodes ($20 \text{ nm}/200\text{nm Ti/Ni}$) and backside contacts ($50 \text{ nm}/500 \text{ nm Ti/Al}$), are deposited and patterned by lift-off using the fourth and fifth masks. A $3\text{-}\mu\text{m}$ thick sacrificial layer for the sensor cavity is deposited by PECVD amorphous silicon ($\alpha\text{-Si}$), and patterned by RIE using the sixth mask. Following this, the top electrode ($20 \text{ nm}/200 \text{ nm Ti/Ni}$) is patterned by lift-off using the seventh mask. To provide good step coverage across the $\alpha\text{-Si}$ layer, the electrode is deposited using sputtering instead of evaporation. Next, a stack of PECVD oxide/nitride/oxide ($100/800/100 \text{ nm}$, ONO) is deposited to form the first layer of the diaphragm, and patterned by RIE for etchant access slots using the eighth mask. The PECVD silicon nitride used in the diaphragm is customized to target a modest tensile stress ($\approx 60 \text{ MPa}$). The purpose of the oxide layers is the protection of the nitride layer in the later XeF_2 etch step. The etchant access slots dimensions of $0.8 \times 5 \text{ } \mu\text{m}^2$ are selected to permit subsequent sealing by additional deposition steps. Smaller dimensions can be considered if appropriate lithography equipment is available. The sacrificial $\alpha\text{-Si}$ layer is etched by gas phase XeF_2 , which provides isotropic etching and very high selectivity to other materials. Before the

cavity is sealed, a thin layer (20 nm) of Al_2O_3 deposited by atomic layer deposition (ALD) is coated on the interior of the cavity, where it covers the electrode surfaces for contact mode insulation. The etchant access slots are sealed by a layer of PECVD nitride, followed by a 100 nm thick layer of ALD Al_2O_3 for hermeticity, which has proven to be a reliable approach to wafer level vacuum sealing [An13].

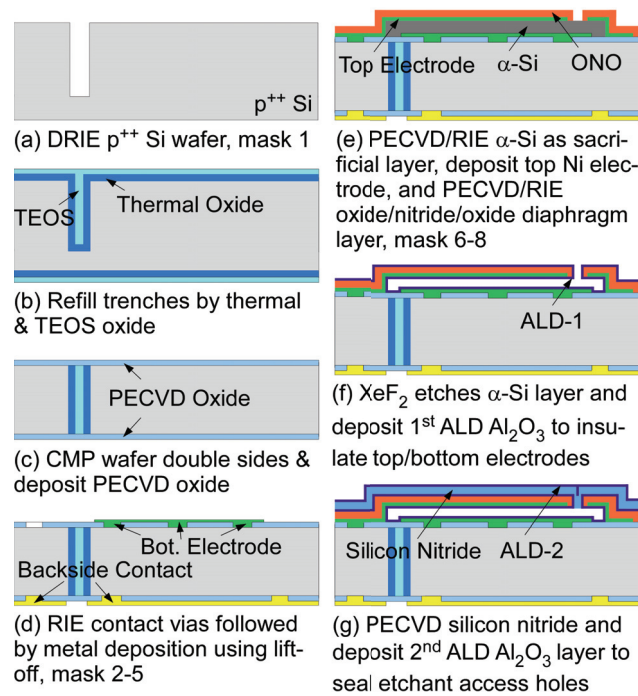


Figure B.7: Fabrication process. (a) Heavily doped silicon wafer is etched by DRIE to define individual isolated region. (b) Etched trenches are filled by thermal oxidation and TEOS deposition. (c) Wafer is double-side lapped and polished, followed by PEDVD oxide on both sides. (d) Metal contact vias are patterned on PECVD oxide layers by RIE, followed by metal deposition using sputtering and liftoff. (e) Amorphous silicon is deposited and patterned as a cavity sacrificial layer, followed by another metal layer deposition and the first diaphragm layer oxide/nitride/oxide (ONO) deposition. (f) Amorphous silicon is etched by gaseous XeF_2 , followed by atomic layer deposition (ALD) of Al_2O_3 . (g) Etchant access slots are sealed by a PECVD silicon nitride layer and another ALD Al_2O_3 layer.

The initial DRIE step targets a depth-to-width aspect ratio >60 , and requires special considerations to prevent lateral undercut, narrowing at the trench bottom, and premature self-termination. A standard Bosch process was used [Lae96], but both the etching and passivation

cycles within it were optimized by a method described in [Owe12]. In the etch cycles, the bias power in the first second of the etch cycles was increased to improve ion directionality and passivation breakthrough. Additionally, the duration of the etch cycles was increased to allow more etchant gas to reach the trench bottom, and the chamber pressure was reduced further to improve the etchant transport. In the passivation cycles, both duration and chamber pressure were increased to increase the thickness of passivation layer and reduce the lateral undercut at the top of the trenches. All these parameters were linearly and continuously changed over the whole 90 min. DRIE step. After DRIE, the trenches were fully filled by a combination of both thermal oxidation and TEOS oxide deposition (Figure B.9a). Thermal oxide provides the insulation strength, whereas TEOS provides conformal filling that prevents the formation of voids in filled trenches.

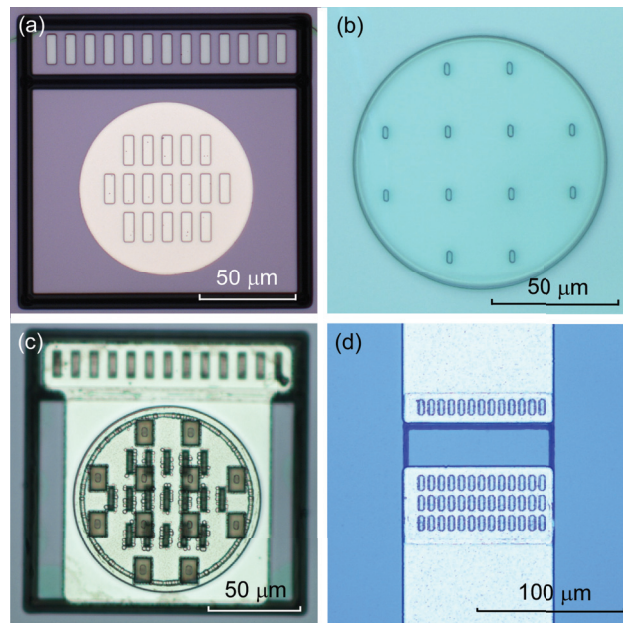


Figure B.8: Selected fabrication results: (a) Top view of a device after bottom Ti/Ni electrode deposition. (b) Top view of a test structure utilized to monitor the XeF_2 etch, since the top electrode of real devices blocks the view of etching process. (c) Top (front) view of a final device. (d) Back view of a final device with Ti/Al contact pads.

Optical images at various stages of fabrication are shown in Figure B.8. Transparent ONO diaphragms were obtained after XeF_2 etching. SEM images of fabricated device are shown in Figure B.9, and a typical device cross section is shown in Figure B.9b. A number of measurements on multiple devices indicate that the diaphragm thickness for a *C100t5* device varies from $4.90\ \mu\text{m}$ to $5.03\ \mu\text{m}$, and the cavity height is between $2.96\ \mu\text{m}$ and $3.25\ \mu\text{m}$.

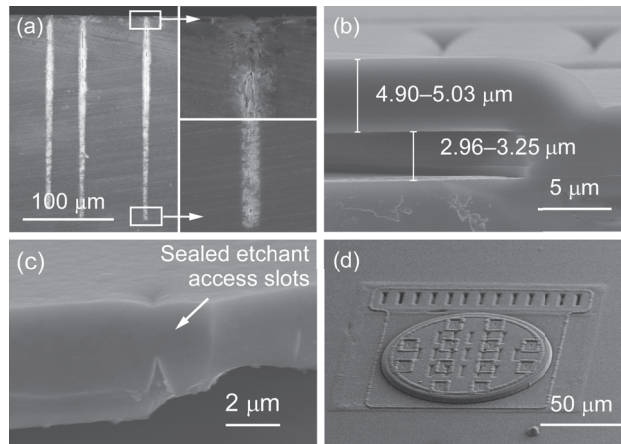


Figure B.9: SEM images of (a) fully filled silicon trenches, (b) details of the *C100t5* cross section, (c) a sealed etchant access slot and (d) a fabricated *C100t5* device.

B.4. Experimental Results

For testing, fabricated wafers were diced into $5\times 5\ \text{mm}^2$ dies with each die containing two devices. Individual die were surface mounted to a prototype board using conductive silver epoxy. The prototype board, together with a thermocouple, was then soldered to a connector, which was inserted into a customized stainless steel pressure chamber (Figure B.10). The chamber can be heated by a heating tape (HSTAT051002, BriskHeat, OH) wrapped outside. The devices were tested in an environment of hydraulic oil (LX-101, Enerpac, WI), pressurized by a manual hydraulic pump (P-142, Enerpac, WI) and monitored by a reference pressure gauge (GP-10S, Enerpac, WI). The device under test (DUT) was read by an Agilent 4284A Precision LCR Meter.

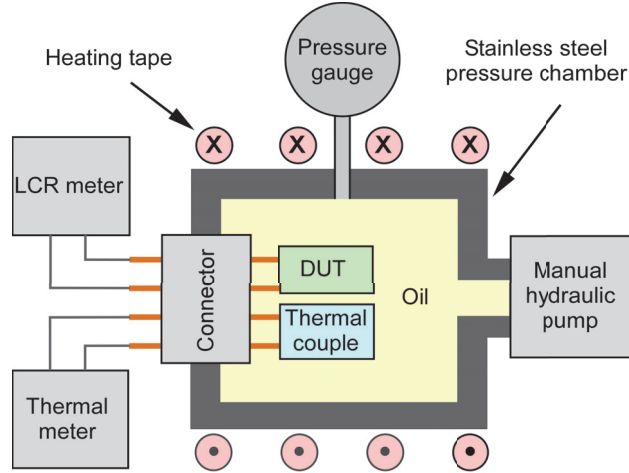


Figure B.10: Experimental setup. The device under test (DUT) and a thermocouple are soldered to a connector, which is inserted into a customized stainless steel pressure chamber. The chamber can be heated using an external heating tape. Pressure is applied by a manual hydraulic pump and measured by a reference pressure gauge. The DUT is read by an LCR meter.

The *C100t3* and *C100t5* devices were tested from atmospheric pressure to 20 MPa and 50 MPa, respectively. Typical pressure responses at room temperature are shown in Figure B.11. Each data point represents an average of ≈ 30 readings taken over three pressure cycles. The normalized pressure sensitivity (S) is given by:

$$S = \frac{\partial(\Delta C)}{C_p \cdot \partial P} \text{ (ppm/MPa)} \quad (\text{B.4})$$

where ΔC is the capacitance change, and C_p is the capacitance at pressure P . In the calculation, C_p is the sum of zero-pressure capacitance, C_0 , based on FEA simulation, and the experimentally measured capacitance change ΔC at P . For the *C100t3* devices, the typical capacitance change over the 20 MPa dynamic range was about 140 fF, and the corresponding average sensitivity was about 7,200 ppm/MPa (3.1 fF/MPa) in the non-contact mode (0–12 MPa), and about 9,900 ppm/MPa (5.3 fF/MPa) in the contact mode (14–20 MPa). The transition occurred between 12 MPa and 14 MPa. In comparison, the *C100t5* devices provided a larger

dynamic range, though the average sensitivity was lower. The typical capacitance change over 50 MPa dynamic range was about 110 fF, and the corresponding average sensitivity was about 3,400 ppm/MPa (1.6 fF/MPa) in the non-contact mode (0–36 MPa), and about 3,100 ppm/MPa (1.6 fF/MPa) in the contact mode (42–50 MPa). The results of both *C100t3* and *C100t5* are summarized in Table B.3.

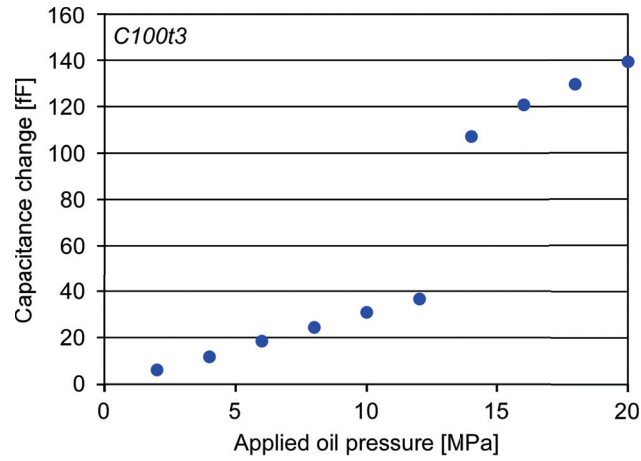
Table B.3: Sensitivities for *C100t3* and *C100t5* in non-contact and contact regions from experimental data.

	<i>C100t3</i>	<i>C100t5</i>
Non-contact (quasi-linear region)	0–12 MPa 0–36.8 fF 7,200 ppm/MPa (3.1 fF/MPa)	0–36 MPa 0–55.4 fF 3,400 ppm/MPa (1.6 fF/MPa)
Contact (linear region)	14–20 MPa 107.5–139.9 fF 9,900 ppm/MPa (5.3 fF/MPa)	42–50 MPa 99.9–110.1 fF 3,100 ppm/MPa (1.6 fF/MPa)

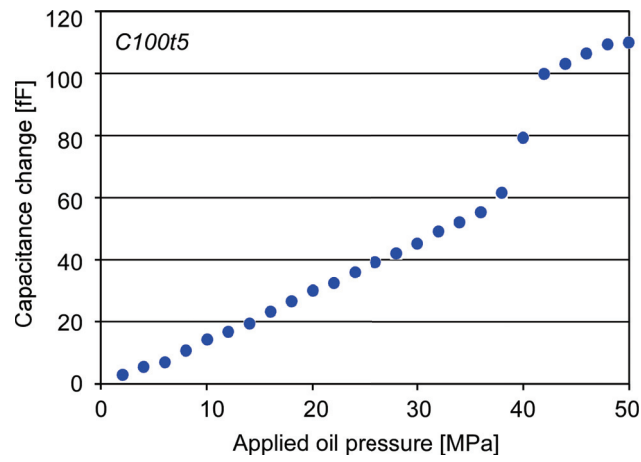
Pressure responses over temperature were investigated for *C100t3* devices in the non-contact mode (Figure B.12). The temperature coefficient of offset (*TCO*) at atmospheric pressure is about 13,800 ppm/°C. The temperature coefficient of sensitivity (*TCS*), defined as:

$$TCS = \frac{\partial S}{S \cdot \partial T} \quad (\text{ppm}/^\circ\text{C}) \quad (\text{B.5})$$

which is about 26,200 ppm/°C at ambient close to room temperature. Both *TCO* and *TCS* are large compared to prior work [Cha01, Cho92], primarily due to the mismatch between the thermal expansion coefficients of diaphragm materials and the substrate, as discussed in Section B.5. In the intended sensing application, however, both temperature and pressure will be measured concurrently, allowing offset and sensitivity to be compensated. For a reading of 10 MPa, the compensation would be approximately -1.84 MPa/°C from *TCO* and -0.26 MPa/°C from *TCS*.



(a)



(b)

Figure B.11: Typical pressure responses measured at room temperature (25°C) for (a) *C100t3* devices and (b) *C100t5* devices. The total capacitance changes are about 140 fF for *C100t3* at 20 MPa, and 110 fF at 50 MPa for *C100t5*. Each data point represents an average of ≈ 30 readings taken over three pressure cycles. Error bars are not visible at this scale.

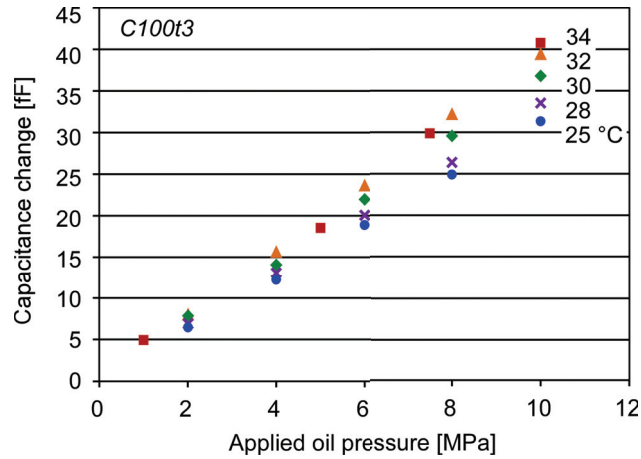


Figure B.12: Typical pressure responses for *C100t3* devices in the non-contact region over temperature.

B.5. Discussion

B.5.1. Comparison of FEA and experiments

It is notable that the experimental results obtained from both *C100t3* and *C100t5* devices agree with expectations, given possible variations in material and dimensional parameters. The typical capacitance change measured from *C100t3* devices was about 140 fF over 20 MPa; contour for this value of full scale change in Figure B.6 shows the combinations of diaphragm diameter, thickness, and Young's modulus that can provide this outcome. The basic properties of PECVD nitride, such as Young's modulus, Poisson's ratio, and residual stress can vary significantly based on deposition conditions [Hua06]. For example, a higher substrate temperature, higher plasma power, and lower chamber gas pressure will all increase the Young's modulus over a range that extends from 100 GPa to 200 GPa. Important dimensions such as the diaphragm diameter are affected by a number of non-idealities, including deviations of feature sizes in lithographic masks, pattern transfer to the photoresist, and the reactive ion etch of the sacrificial layer. Additionally, the effective thickness of the diaphragm can vary, not only from

the deposition process but also from variations in the etchant access slots. As shown in Figure B.9c, the diaphragm thickness in the region near sealed slots is thinner than the targeted value; this increases the diaphragm compliance. A more compliant diaphragm in turn increases the capacitive response to pressure.

B.5.2. TCO and TCS

Thermal Expansion Mismatch

The mismatch between thermal expansion coefficients of diaphragm materials and the substrate is the primary cause of large *TCO* and *TCS*. Diaphragm materials include silicon nitride (2.8 μm for *C100t3* and 4.8 μm for *C100t5*), silicon oxide (0.2 μm), aluminum oxide (0.12 μm) and Ti/Ni (0.02/0.2 μm). From the thermal expansion coefficients listed in Table B.4, the average value, weighted by thickness, is 3.3–4.4 ppm/°C for *C100t3* and 3.0–4.2 ppm/°C for *C100t5*. In contrast, the value for the silicon substrate is 2.6 ppm/°C. As a result, the diaphragm expands more than the substrate, exaggerating the deflection toward the substrate that is caused by the applied pressure. The reduced cavity gap not only increases *TCO*, but also increases sensitivity at a given pressure and contributes to *TCS*. Additionally, the thermal expansion of the silver epoxy and prototype board can change parasitic capacitance values, impacting *TCO*. In the long term, *TCO* and *TCS* can be reduced by at least 10 \times by reducing the metal thickness or replacing the Ni with a softer metal such as Al, and increasing residual tensile stress in the diaphragm to reduce bowing, and improving the attachment and lead transfer to the prototype board.

Table B.4: Thermal expansion coefficients of materials used in the device.

Materials	Thermal expansion ppm/°C
Si	2.6
Si ₃ N ₄	2.5–3.8 [Tam72, Rie88]
SiO ₂	0.4–0.5 [Rie88, Cho92]
Al ₂ O ₃	8.1
Ni	13.4
Ti	8.6

Uncertainty Estimation of TCS

The uncertainty mainly stems from two sources: the temperature fluctuation during the measurements at a targeted temperature and the fluctuation of readings at a given pressure from the LCR meter.

Limited by the precision of the temperature control, a fluctuation about 0.1°C can exist between two measurements at different pressure in the tests. According to the TCS , a fluctuation of 0.1°C induces an equivalent capacitance fluctuation ΔC_T of about 0.57 fF. The standard deviation of each measurement, σ_T , due to the temperature fluctuation is $\frac{1}{\sqrt{2}} \Delta C_T$ [Tay97]. The uncertainty of sensitivity ($\sigma_{s,T}$) and TCS ($\sigma_{TCS,T}$) can be derived using the method of propagation of uncertainty. The uncertainty of sensitivity ($\sigma_{s,T}$) and TCS ($\sigma_{TCS,T}$) are derived using the method of propagation of uncertainty [Tay97], and given by:

$$\sigma_{s,T} = \sigma_T \cdot S \cdot \sqrt{\frac{2}{(\Delta C)^2} + \frac{1}{C^2}} \quad (\text{ppm/MPa}) \quad (\text{B.6})$$

$$\sigma_{TCS,T} = \sigma_{s,T} \cdot TCS \cdot \sqrt{\frac{2}{(\Delta S)^2} + \frac{1}{2 \cdot S^2}} \quad (\text{ppm/°C}) \quad (\text{B.7})$$

where $S \approx 8,500$ ppm/MPa is the averaged sensitivity over 25–34°C in the 0–10 MPa region shown in Figure B.12, $\Delta C \approx 35$ fF is the capacitance change used to calculate the average sensitivity, $C \approx 430$ fF is the average capacitance, $\Delta S \approx 2,200$ ppm/MPa is the sensitivity difference between 25°C and 34°C, $TCS \approx 26,200$ ppm/°C is the average temperature coefficient of sensitivity over this temperature range. Then the uncertainty of sensitivity and TCS induced by temperature fluctuation are obtained as:

$$\sigma_{S,T} \approx 138 \text{ ppm/MPa} , \quad (\text{B.8})$$

$$\sigma_{TCS,T} \approx 2,582 \text{ ppm/}^\circ\text{C} . \quad (\text{B.9})$$

As mentioned before, the other main source of uncertainty comes from the fluctuation of readings from the LCR meter. A number of possible factors can cause the fluctuation, such as mechanical noise and electrical noise. In the measurement, each data is an average of 7–10 readings over about 5 seconds, and the standard deviation of 7–10 readings is about 0.5 fF. The temperature during each measurement (≈ 5 s) is assumed stable, although it can vary across measurements at different pressure as discussed above. The same method as the analysis of temperature fluctuation induced uncertainty is used, and the uncertainty of readings from the LCR meter are calculated as:

$$\sigma_{S,R} \approx 172 \text{ ppm/MPa} , \quad (\text{B.10})$$

$$\sigma_{TCS,R} \approx 3,203 \text{ ppm/}^\circ\text{C} . \quad (\text{B.11})$$

With the assumption that the temperature is stable during each measurement (≈ 5 s) at a certain pressure, the uncertainty from temperature fluctuation $\sigma_{TCS,T}$ and the uncertainty from LCR meter $\sigma_{TCS,R}$ are uncorrelated. The total uncertainty is given by Eq. (B.12).

$$\sigma_{TCS} = \sqrt{(\sigma_{TCS,T})^2 + (\sigma_{TCS,R})^2} = 4,100 \text{ (ppm/}^\circ\text{C)} \quad (\text{B.12})$$

The σ_{TCS} is relatively large, mainly because the swing of capacitive response, i.e. ΔC , is small (~ 10 's fF) due to the small sensor diaphragm. The final TCS is then expressed as:

$$TCS = 26,200 \pm 4,100 \text{ (ppm/}^\circ\text{C)}. \quad (\text{B.13})$$

B.5.3. Noise

There are two primary sources of noise associated with the pressure sensor: (1) Brownian mechanical noise and (2) electrical kT/C noise.

Brownian Noise

Brownian noise is one of the fundamental noise sources for diaphragm based pressure sensors. At low pressures, the mean free path of gas molecules is larger than the diaphragm diameter, and the local pressure fluctuations over the diaphragm are not spatially nor temporally correlated. At higher pressures, the increased collective interaction among gas molecules results in thermally generated acoustic waves and the pressure fluctuations then become correlated over space and time [Cha87a]. The pressure fluctuation in the medium can then be determined by calculating the density of thermal-acoustic vibration modes in it, as expressed in Eq. (B.14) [Mel52, Hun72, Cha87a]:

$$\overline{P^2}(f) = \frac{4\pi kT \rho f^2}{c} \quad (\text{B.14})$$

where $\overline{P^2}(f)$ is the power spectrum of the pressure fluctuation, k is the Boltzmann constant, ρ is the density of the medium, and c is the speed of sound in the medium. The mean-square sound pressure, in the frequency band $f_2 - f_1$ is then given by Eq. (B.15):

$$\overline{P_n^2} = \int_{f_1}^{f_2} \frac{4\pi kT \rho f^2}{c} df = \frac{4\pi kT \rho}{3c} (f_2^3 - f_1^3). \quad (\text{B.15})$$

To calculate the numerical value, following parameters are used: $k = 1.38 \times 10^{-23} \text{ J} \cdot \text{K}^{-1}$, $T = 298 \text{ K}$, $\rho = 900 \text{ kg/m}^3$, $c = 1,461 \text{ m/s}$, $f_2 = 10 \text{ kHz}$ and $f_1 = 20 \text{ Hz}$. Tests were taken in oil, and the frequency range was determined by the HP4284A LCR meter. The root mean square (*rms*) thermal noise pressure is then calculated as:

$$P_{rms} = \sqrt{\overline{P_n^2}} \approx 0.1 \text{ mPa}. \quad (\text{B.16})$$

Compared to the target operation pressure range $\sim \text{MPa}$, the thermal noise from Brownian motion is 10 orders of magnitude lower, which can be safely ignored.

If the frequency range is not limited by the LCR meter, it can be determined from the bandwidth of the sensor itself or from the interface circuits. For the given sensor structures of $\text{\textcircled{1}}100 \mu\text{m}$ devices, the bandwidth can be calculated or measured from damping coefficient and resonant frequency. For an analytical estimation, the resonant frequencies are obtained at 6.08 MHz for *C100t3* and 4.03 MHz for *C100t5* from the FEA in COMSOL. The limit from interface circuits will not be discussed here.

kT/C Noise

The kT/C noise is another fundamental noise source due to a single electrical degree of freedom associated with a capacitor. It is described by Eq. (B.17) [Cha87b]:

$$\overline{P_n^2} = \frac{kT(C_0 + C_p)}{(V_s \cdot C_0 \cdot S)^2} \quad (\text{B.17})$$

where C_0 is the zero-pressure capacitance and C_p is the parasitic capacitance in parallel with it, V_s is the bias voltage used to read out the capacitance, S is the sensitivity. To calculate the mean square pressure due to the capacitor noise, the following parameters are used: $C_0 = 412.9$ fF from FEA for both $C100t3$ and $C100t5$, C_p is in the order of 10's pF based on the readings from the LCR meter, including parasitic capacitance from prototype board, cables, connectors etc., $C_p = 10$ pF is used in this estimation, $V_s = 5$ V, sensitivity S is from experimental results listed in Table B.3. The *rms* pressures due to kT/C capacitor noise are:

$$P_{rms, C100t3} \approx 0.01 \text{ MPa} , \quad (\text{B.18})$$

$$P_{rms, C100t5} \approx 0.03 \text{ MPa} . \quad (\text{B.19})$$

It is noticed that the kT/C noise is a broadband noise, and is diminished by the bandwidth of the system in most cases.

Besides the fundamental noise mechanisms discussed above, readout circuit noise exists in a typical integrated system. Since the capacitance is measured through an LCR meter instead of a particular integrated circuit in this work, circuit noise will not be discussed here.

B.6. Conclusions

The fabrication process presented in this Appendix essentially combines surface micromachining with through-silicon lead transfer. The only high temperature step is a thermal oxidation; there are no wet etching steps; and the process requires only one wafer. Consequently, the process is scalable, permitting the fabrication of pressure sensors that can be highly miniaturized, with small diaphragm and backside contacts.

Two types of fabricated devices, *C100t3* and *C100t5*, were successfully tested over a pressure range of 0–20 MPa and 0–50 MPa, respectively. In the quasi-linear region of non-contact mode, the average sensitivities were 7,200 ppm/MPa (3.1 fF/MPa, 0–12 MPa) for *C100t3* devices, and 3,400 ppm/MPa (1.6 fF/MPa, 0–36 MPa) for *C100t5* devices. In the linear region of contact mode, the average sensitivities were about 9,900 ppm/MPa (5.3 fF/MPa, 14–20 MPa) for *C100t3* devices, and 3,100 ppm/MPa (1.6 fF/MPa, 42–50 MPa) for *C100t5* devices. Experimental results were consistent with simulated values within the range of variation expected in material properties and dimensions. For the *C100t3* in non-contact operation, the upper limit of *TCO* at atmospheric pressure was about 13,800 ppm/°C and the average *TCS* was 26,200±4,100 ppm/°C, mainly due to the mismatch between thermal expansion coefficients of diaphragm and substrate materials. In the long term, such devices are expected to find utility in a variety of applications ranging from oil exploration to industrial monitoring and robotics.

APPENDIX C:

Run Sheet of the Second Generation Microdischarge-Based Pressure Sensors

This appendix outlines detailed information of microfabrication steps for the second generation microdischarge-based pressure sensor described in Chapter 3. A brief summary is listed in Table C.1, followed by the run sheet with detailed steps.

Table C.1: A brief summary of the process steps for the second generation microdischarge-based pressure sensor.

Process Steps
Photomask 10 DRIE Si Trenches
10.10 Wet oxidation 2 μm - DRIE mask
10.20 Lithography
10.30 Oxide mask etch
10.40 DRIE $\approx 250 \mu\text{m}$
10.50 Wet oxidation filling 2 μm
10.60 TEOS filling 1.8 μm
10.70 Front CMP
10.80 Backside Lapping & CMP
10.90 PECVD oxide front side 0.2 μm /back side 3 μm
Photomask 20 RIE Backside Contact Vias
20.10 Lithography
20.20 RIE back contact vias
Photomask 30 Backside Ti/Al Contact Pads
30.10 Lithography (Image Reversal)
30.15 Plasma descum
30.20 Sputter Ti 500 \AA /Al 5000 \AA
30.30 Lift-off in acetone
Photomask 40 RIE Front Contact Vias
40.10 Lithography
40.20 RIE front contact vias
Photomask 50 Bottom Ti/Ni Electrodes

50.10 Lithography (IR)
50.15 Plasma descum
50.20 Evaporation of Ti 2000 Å/Ni 500 Å
50.30 Lift-off in acetone

Photomask 60 Pattern α -Si Sacrificial Layer

60.10 PECVD α -Si 3 μ m
60.20 Lithography
60.30 RIE α -Si pattern

Photomask 70 Top Ni/Al Electrode

70.10 Lithography (LOR)
70.15 Plasma descum
70.20 Sputter Ni 500 Å/Al 2000 Å
70.30 Lift-off

Photomask 80 Etchant Access Slots

80.10 PECVD 1st ONO 0.15/0.8/0.15 μ m
80.20 Lithography
80.30 RIE etch slots
80.35 Dicing
80.40 XeF₂ etch
80.50 PECVD 2nd nitride 3.9 μ m
80.60 ALD sealing 100 nm

Details of process run sheet

Photomask [10-DRIE Si]

10.10 Wet oxidation

Date:

- Wafer IDs:
- Pre-furnace clean
 - Tool: PFC-01
 - Recipe: RCA cleaning
 - Organic clean. H₂O:H₂O₂:NH₄OH = 5:1:1 (10min) @85°C
 - DI rinse 2 cycles
 - Oxide strip. 100:1 HF (30s)
 - DI rinse 2 cycles
 - Ionic clean. H₂O:H₂O₂:HCl = 6:1:1 (10min) @85°C
 - DI rinse 4 cycles
 - Spin dry

- Wet oxidation
 - Tool: S3T2-Wet Oxidation 4” and 6”
 - Recipe: 1100 °C, 9h
- Inspection & comments:
 - Grow 2µm thermal oxide, measured using Nanospec.

10.20 Lithography

Date:

- Wafer IDs:
- Spin coat photoresist & soft bake
 - Tool: ACS 200 Cluster
 - Recipe: SPR 220 3.0 5µm
 - Details: soft bake at 115°C, 90s; recipe includes HMDS vapor prime coat
- Expose
 - Tool: GCA AS200 AutoStep
 - Recipe: Exposure time 0.41s
 - After exposure, hold for 10mins
- Develop
 - Tool: ACS 200 Cluster
 - Recipe: Bake & Dev 115 120s 300 DEV 40s
 - Post bake @115°C 120s
 - Developer: AZ-300 MIF 40s
- Inspection & comments:

10.30 Oxide mask etch

Date:

- Wafer mounting
 - Tool: Vacuum hotplate @80°C
 - Bonding media: Santovac 5, 100 µL
 - Santovac 5 is a hydrocarbon based diffusion pump oil that spreads very thinly and evenly providing uniform thermal contact
 - Carrier: 6” silicon wafer
 - Time: 5 mins
- RIE
 - Tool: LAM 9400
 - Recipe: mnf_oxide1
 - Etch rate: expected oxide 1750Å/min, PR measured 1150-1230 Å/min
 - Etch time: (2µm/0.175µm/min*110%≈13mins)
- Wafer releasing
 - Tool: Vacuum hotplate @80°C

- Time: 30s
- Wafer cleaning
 - Acetone and IPA clean Santovac 5
- Inspection & comments:
 - Etch oxide mask, alternatively could use STS Glass etcher (uk submicron etch recipe, 9mins, 0.25 μ m/min) or STS Pegasus 4 (Oxynitride recipe 16mins, 0.14 μ m/min)
 - Sidewall profile of Pegasus 4 etching is not as vertical as LAM 9400
 - Glass etcher has more physical etching, could burn PR mask

10.40 DRIE

Date:

- Wafer IDs:
- Wafer mounting
 - Tool: Vacuum hotplate @80°C
 - Bonding media: Santovac 5, 100 μ L
 - Carrier: 4" silicon wafer
 - Time: 5 mins
- DRIE
 - Tool: STS Pegasus 4
 - Recipe: Modified LNF recipe 1 (parameters ramping)
 - Etch time: 45mins+45mins
- Wafer releasing
 - Tool: Vacuum hotplate @80°C
 - Time: 30s
- Wafer cleaning
 - Acetone and IPA clean Santovac 5
 - SPR 2000, 15mins, DI rinsed 4 cycles
 - Nanostrip: Acid 12, removing remaining PR
 - HF (49%) etching: Acid 12, 2mins, removing remaining oxide
- Inspection & comments:
 - Backside protection uses carrier Si wafer

Table C.2: Table of parameters ramping in customized recipe 1 for DRIE.

Time (mins)	Recipe	Etch parameters			Passivation parameters	
		Step length (sec)	Pressure (mTorr)	Bias power (W)	Step length (sec)	Pressure (mTorr)
	Recipe 1	2.6	30	60	2	24
0-90	Custom	2.6→4.4	30→21	60→114	2→2.9	24→30

10.45 Si thinning (optional)

Date:

- Wafer IDs:
- Wafer mounting
 - Tool: Vacuum hotplate @80°C
 - Bonding media: Santovac 5, 100 μ L
 - Carrier: 6" silicon wafer
 - Time: 5 mins
- RIE thinning
 - Tool: LAM 9400
 - Recipe: Oxynitride
 - Etch rate: Measured oxide 1800-1900Å/min; Measured Si 1200-1500 Å/min
 - Etch time: $5\mu\text{m}/0.15\mu\text{m}/\text{min}=33\text{min}$
- Wafer releasing
 - Tool: Vacuum hotplate @80°C
 - Time: 30s
- Wafer cleaning
 - Acetone & IPA
- Inspection & comments:
 - Removing narrowed Si layer, prepare for oxide filling
 - This step was not performed in the first batch of process
 - If DRIE is optimized based on Recipe 4 to reduce undercut, this step is not necessary

10.50 Wet oxidation

Date:

- Wafer IDs:
- Pre-furnace clean
 - Tool: PFC-01
 - Recipe: RCA cleaning
 - Organic clean. $\text{H}_2\text{O}:\text{H}_2\text{O}_2:\text{NH}_4\text{OH} = 5:1:1$ (10min) @85°C
 - DI rinse 2 cycles
 - Oxide strip. 100:1 HF (30s)
 - DI rinse 2 cycles
 - Ionic clean. $\text{H}_2\text{O}:\text{H}_2\text{O}_2:\text{HCl} = 6:1:1$ (10min) @85°C
 - DI rinse 4 cycles
 - Spin dry
- Wet oxidation
 - Tool: S3T2-Wet Oxidation 4" and 6"
 - Recipe: 1100 °C, 9h
- Inspection & comments:

- Grow 2 μ m thermal oxide, measured using Nanospec.

10.60 TEOS

Date:

- Wafer IDs:
- Tool: S4T4 TEOS 4" only
- Recipe: TEOS
 - Time: 2.5 hrs (\approx 120 \AA /min)
 - Thickness: 1.8 μ m (measured using Nanospec on monitor wafer)
- Inspection & comments

10.70 Front CMP

Date:

- Wafer IDs:
- Bonding
 - Tool: Hotplate at 150 $^{\circ}$ C, bonding frame (from WetChem)
 - Recipe:
 - Put glass carrier on hotplate at 150 $^{\circ}$ C
 - Apply bond wax evenly on glass carrier: 0CON-200-Quartz wax (Logitech Inc.)
 - Put wafer on melted wax, align and apply pressure using bonding frame
 - Wait for 20mins and put the frame on cooling station, until temp <60 $^{\circ}$ C
- Lapping
 - Tool: Lapper
 - Recipe: Grit size 9 μ m and 3 μ m
 - Removing rate: N/A
 - Time: Frequently check the wafer surface
- Polishing
 - Tool: CMP Strasbaugh 6EC
 - Recipe: Si-CMP
 - Polishing rate: N/A
 - Time: 9 mins
- Post CMP clean
 - Tool: SSEC Wafer Cleaner
 - Recipe: Oxide Clean 100mm Glass
- Releasing
 - Tool: Hotplate at 150 $^{\circ}$ C
 - Recipe:
 - Put the bonded wafer on hotplate
 - Wait for 1 min
 - Slowly slide the wafer out using swab
- Cleaning
 - Tool: Solvent bench, with Xylenes
 - Recipe:
 - Xylenes clean

- Acetone and IPA clean
 - N₂ gun blow dry (from a small angle with the wafer, starting at a far distance, then carefully move close to the wafer)
- Inspection & comments:

10.80 Backside thinning & CMP

Date:

- Wafer IDs:
- Bonding
 - Tool: Hotplate at 150°C, bonding frame (from WetChem)
 - Recipe:
 - Put glass carrier on hotplate at 150°C
 - Apply bond wax evenly on glass carrier: 0CON-200-Quartz wax (Logitech Inc.)
 - Put wafer on melted wax, align and apply pressure using bonding frame
 - Wait for 20mins and put the frame on cooling station, until temp <60°C
- Lapping
 - Tool: Lapper
 - Recipe: Grit size 20µm/9 µm/3 µm
 - Removing rate: N/A
 - Time: Frequently check the wafer surface
- Polishing
 - Tool: CMP Strasbaugh 6EC
 - Recipe: Si-CMP
 - Polishing rate: N/A
 - Time: 9 mins
- Post CMP clean
 - Tool: SSEC Wafer Cleaner
 - Recipe: Oxide Clean 100mm Glass
- Releasing
 - Tool: Hotplate at 150°C
 - Recipe:
 - Put the bonded wafer on hotplate
 - Wait for 1 min
 - Slowly slide the wafer out using swab
- Cleaning
 - Tool: Solvent bench, with Xylenes
 - Recipe:
 - Xylenes clean
 - Acetone and IPA clean
 - N₂ gun blow dry (from a small angle with the wafer, starting at a far distance, then carefully move close to the wafer)
- Inspection & comments:
 - After CMP, wafer becomes about 200 µm thick, which is determined by the depth of DRIE trenches. Handle carefully.

10.80 PECVD oxide double sides

Date:

- Wafer IDs:
- PECVD oxide
 - Tool: GSI PECVD
 - Recipe: Oxide 380
 - Thickness: 2000 Å front, and 30000 Å for backside (measured by Nanospec)

Photomask [20-Back vias]

20.10 Lithography

Date:

- Wafer IDs:
- Spin coat photoresist & soft bake
 - Tool: CEE 100CB Spinner
 - Photoresist: SPR220 3.0
 - Recipe:
 - #3, 3000 rpm, HMDS
 - #3, 3000 rpm, 2.6 μm
 - Soft bake: hotplate @115°C 90s
- Expose
 - Tool: MA/BA-6 contact aligner
 - Recipe: Hard contact, exposure time 7s
- Post exposure bake & Develop
 - Post exposure bake: hotplate @115°C 90s
 - Tool: CEE developer #2
 - Recipe: AZ-726 (300) MIF DP 40-40
 - Developer: AZ-726 (300) MIF, double puddle, 40s+40s
- Inspection & comments:

20.20 RIE back contact vias

Date:

- Wafer IDs:
- Wafer mounting
 - Tool: Vacuum hotplate @80°C
 - Bonding media: Santovac 5, 100 μL
 - Carrier: 6" silicon wafer
 - Time: 5 mins
- RIE

- Tool: LAM 9400
- Recipe: Oxynitride
 - Etch rate: measured $1850 \pm 50 \text{ \AA}/\text{min}$
- Etch time: $3 \text{ \mu m} / 0.185 \text{ \mu m}/\text{min} * 120\% = 1,168\text{s}$
- Wafer removing
 - Tool: Vacuum hotplate @80°C
 - Time: 30s
- Wafer cleaning
 - Acetone and IPA clean Santovac 5
 - SPR 2000, 15mins, DI rinsed 4 cycles, plasma stripper clean @150°C 3 mins
- Inspection & comments
 - Check etched contact vias under microscope. Fully etched holes look clear. Otherwise, remaining oxide will show light red or blue based on the remaining thickness. Then, more time should be added to run another etch process.
 - Etch rate can drift over time, do characterization on monitor wafer before process

Photomask [30-Ti/Al Pads]

30.10 Lithography (IR)

Date:

- Wafer IDs:
- Spin coat photoresist & soft bake
 - Tool: CEE 100CB Spinner
 - Photoresist: SPR220 3.0
 - Recipe:
 - #3, 3000 rpm, HMDS
 - #3, 3000 rpm, 2.6 μm
 - Soft bake: hotplate @115°C 90s
- 1st expose
 - Tool: MA/BA-6, contact aligner
 - Recipe: Hard contact, exposure time 7s
- 1st post exposure bake
 - Post exposure bake: hotplate @115°C 90s
- Image reversal
 - Tool: Image reversal oven
 - Recipe: #2
- Flood exposure

- Tool: MA6
- Recipe: Lamp test 14s
- 2nd post exposure bake
 - Post exposure bake: hotplate @115°C 90s
- Develop
 - Tool: CEE developer #2
 - Recipe: AZ-726 (300) MIF DP 40-40
 - Developer: AZ-726 (300) MIF, double puddle, 40s+40s
- Inspection & comments:

30.15 Plasma descum

Date:

- Wafer IDs:
- Tool: YES plasma stripper
- Recipe: #4, 20s
- Inspection & comments

30.20 Sputter Ti/Al

Date:

- Wafer IDs:
- Tool: Lab18_2
- Recipe: Ti2 and Al5
- Thickness: Ti 500 Å, Al 5000Å
- Deposit rate: Ti 1.5 Å/s, Al 2.5 Å/s
- Time: Ti 333s, Al 2000s
- Inspection & comments:

30.30 Lift-off

Date:

- Wafer IDs:
- Tool: Bench 84 or 14
- Recipe: Acetone in lift-off labeled beaker, put aluminum foil to cover the beaker
- Time: ~2h (over night if possible)
- Ultrasonic bath: gentle ultrasonic bath, strength level less than 2, >30mins
- Rinse: 4 cycles, and N₂ gun dry
- Inspection & comments:
 - Keep the wafer wet when transfer from the acetone beaker to the DI tank

Photomask [40-Front Vias]

40.10 Lithography

Date:

- Wafer IDs:
- Spin coat photoresist & soft bake
 - Tool: CEE 100CB Spinner
 - Photoresist: SPR220 3.0
 - Recipe:
 - #3, 3000 rpm, HMDS
 - #3, 3000 rpm, 2.6 μm
 - Soft bake: hotplate @115°C 90s
- Expose
 - Tool: GCA AS200 AutoStep
 - Recipe: Exposure time 0.32s
- Post exposure bake & Develop
 - Post exposure bake: hotplate @115°C 90s
 - Tool: CEE developer #2
 - Recipe: AZ-726 (300) MIF DP 40-40
 - Developer: AZ-726 (300) MIF, double puddle, 40s+40s
- Inspection & comments:

40.20 RIE front contact vias

Date:

- Wafer IDs:
- Wafer mounting
 - Tool: Vacuum hotplate @80°C
 - Bonding media: Santovac 5, 100 μL
 - Carrier: 6" silicon wafer
 - Time: 5 mins
- RIE
 - Tool: LAM 9400
 - Recipe: Oxynitride
 - Etch rate: measured 1850 \pm 50 $\text{\AA}/\text{min}$
 - Etch time: 0.2 $\mu\text{m}/0.185 \mu\text{m}/\text{min} * 120\% = 78\text{s}$
- Wafer removing
 - Tool: Vacuum hotplate @80°C
 - Time: 30s
- Wafer cleaning
 - Acetone and IPA clean Santovac 5
 - SPR 2000, 15mins, DI rinsed 4 cycles, plasma stripper clean @150°C 3 mins
- Inspection & comments

- Check etched contact vias under microscope. Fully etched holes look clear. Otherwise, remaining oxide will show light red or blue based on the remaining thickness. Then, more time should be added to run another etch process.

Photomask [50-Bot Ni]

50.10 Lithography (IR)

Date:

- Wafer IDs:
- Spin coat photoresist & soft bake
 - Tool: CEE 100CB Spinner
 - Photoresist: SPR220 3.0
 - Recipe:
 - #3, 3000 rpm, HMDS
 - #3, 3000 rpm, 2.6 μm
 - Soft bake: hotplate @115°C 90s
- 1st expose
 - Tool: GCA AS200 AutoStep
 - Recipe: Exposure time 0.32s
- 1st post exposure bake
 - Post exposure bake: hotplate @115°C 90s
- Image reversal
 - Tool: Image reversal oven
 - Recipe: #2
- Flood exposure
 - Tool: MA6
 - Recipe: Lamp test 14s
- 2nd post exposure bake
 - Post exposure bake: hotplate @115°C 90s
- Develop
 - Tool: CEE developer #1 or #2
 - Recipe: AZ-726 (300) MIF DP 40-40
 - Developer: AZ-726 (300) MIF, double puddle, 40s+40s
- Inspection & comments:

50.15 Plasma descum

Date:

- Wafer IDs:

- Tool: YES plasma stripper
- Recipe: #4, 20s
- Inspection & comments

50.20 Evaporation Ti/Ni

Date:

- Wafer IDs:
- Tool: SJ-20 Evaporator
- Recipe: Ti and Ni
- Thickness: Ti 2000 Å, Ni 500Å
- Deposit rate: Ti 5 Å/s, Ni 5 Å/s
- Time: Ti 400s, Ni 100s
- Inspection & comments:
 - Stress of Ni is large ≈ 1 GPa tensile, limit the maximum thickness $\leq 500\text{\AA}$.

50.30 Lift-off

Date:

- Wafer IDs:
- Tool: Bench 84 or 14
- Recipe: Acetone in lift-off labeled beaker, put aluminum foil to cover the beaker
- Time: ~ 2 h (over night if possible)
- Ultrasonic bath: gentle ultrasonic bath, strength level less than 2, >30 mins
- Rinse: 4 cycles, and N₂ gun dry
- Inspection & comments:
 - Keep the wafer wet when transfer from the acetone beaker to the DI tank.

Photomask [60-Sacrificial]

60.10 PECVD α -Si 240

Date:

- Wafer IDs:
- PECVD deposition
 - Tool: GSI PECVD
 - Recipe: Customized α -Si 240 low stress
 - SiH₄-90sccm_RF-100W_Temp-240°C_Pressure-3.5Torr
 - Deposit rate: 22.4 Å/s
 - Thickness: Maximum 15000 Å/run; two runs
- Inspection & comments:
 - Thickness measurement using Woollam M-2000 Ellipsometer

60.20 Lithography

Date:

- Wafer IDs:
- Spin coat photoresist & soft bake

- Tool: CEE 100CB Spinner
- Photoresist: SPR220 3.0
- Recipe:
 - #3, 3000 rpm, HMDS
 - #3, 3000 rpm, 2.6 μm
- Soft bake: hotplate @115°C 90s
- Expose
 - Tool: GCA AS200 AutoStep
 - Recipe: Exposure time 0.32s
- Post exposure bake & Develop
 - Post exposure bake: hotplate @115°C 90s
 - Tool: CEE developer #2
 - Recipe: AZ-726 (300) MIF DP 40-40
 - Developer: AZ-726 (300) MIF, double puddle, 40s+40s
- Inspection & comments:

60.30 RIE α -Si pattern

Date:

- Wafer IDs:
- RIE
 - Tool: PlasmaTherm 790
 - Recipe: CF₄/O₂ 42 sccm/4.7 sccm (10% of O₂), 150 mTorr
 - Etch time: 30–50 mins, loading dependent
 - Etch rate varies from chamber center (slow) to rim (fast), divided into multiple runs if possible, and rotate the sample accordingly
- Wafer cleaning
 - Acetone and IPA clean Santovac 5
 - SPR 2000, 15mins, DI rinsed 4 cycles, plasma stripper clean @150°C 3 mins
- Inspection & comments

Photomask [70-Top Ni]

70.10 Lithography

Date:

- Wafer IDs:
- Spin coat photoresist & soft bake
 - Tool: CEE 100CB Spinner
 - Photoresist: LOR10B+SPR220 3.0
 - Spin: #3, 3000 rpm, LOR10B \approx 0.75 μm

- Soft bake: hotplate @190°C 300s
- Spin: #2, 2000 rpm, SPR 220 3.0 ≈3.5 μm
- Soft bake: hotplate @115°C 360s
- Expose
 - Tool: GCA AS200 AutoStep
 - Recipe: Exposure time 0.7s
- Develop
 - Tool: Manual
 - Recipe: AZ-726 (300) MIF 35+5s
- Inspection & comments:

70.15 Plasma descum

Date:

- Wafer IDs:
- Tool: YES plasma stripper
- Recipe: #4, 480s
- Inspection & comments

70.20 Sputter Ni

Date:

- Wafer IDs:
- Tool: Lab18_2
- Recipe: Ni4 and Al5
- Thickness: Ni 500 Å, Al 2000Å
- Deposit rate: Ni 4 Å/s, Al 2.5 Å/s
- Time: Ni 125s, Al 800s
- Inspection & comments:

70.30 Lift-off

Date:

- Wafer IDs:
- Tool: Bench 84 or 14
- Recipe: Remover PG @85°C in lift-off labeled beaker, put aluminum foil to cover
- Time: ~30mins
- Ultrasonic bath: gentle ultrasonic bath, strength level less than 2, >30 mins
- Clean in IPA before rinse
- Rinse: 4 cycles, and N₂ gun dry
- Inspection & comments:
 - Keep the wafer wet when transfer from the Remover PG beaker to the IPA beaker

Photomask [80-Etch Hole]

80.10 PECVD ONO

Date:

- Wafer IDs:
- Tool: GSI PECVD
- Recipe: Oxide 380/customized Nitride 380
- Thickness: 0.15/0.8/0.15 μm
- Measure thickness and stress
 - Refer to the monitor wafer
- Inspection & comments:

80.20 Lithography

Date:

- Wafer IDs:
- Spin coat photoresist & soft bake
 - Tool: CEE 100CB Spinner
 - Photoresist: SPR220 3.0
 - Recipe:
 - #3, 3000 rpm, HMDS
 - #4, 4000 rpm, 2.1 μm
 - Soft bake: hotplate @115°C 90s
- Expose
 - Tool: GCA AS200 AutoStep
 - Recipe: Exposure time 0.4s
- Post exposure bake & Develop
 - Post exposure bake: hotplate @115°C 90s
 - Tool: CEE developer #2
 - Recipe: AZ-726 (300) MIF DP 40-40
 - Developer: AZ-726 (300) MIF, double puddle, 40s+40s
- Inspection & comments:

80.30 RIE etch slots

Date:

- Wafer IDs:
- Wafer mounting
 - Tool: Vacuum hotplate @80°C
 - Bonding media: Santovac 5, 100 μL
 - Carrier: 6" silicon wafer
 - Time: 5 mins
- RIE
 - Tool: LAM 9400
 - Recipe: Oxynitride
 - Oxide etch rate: measured 1850 \pm 50 $\text{\AA}/\text{min}$

- Nitride etch rate: measured $2700 \pm 100 \text{ \AA}/\text{min}$
 - Etch time: $0.3 \text{ \mu m}/0.185 \text{ \mu m}/\text{min} + 0.8 \text{ \mu m}/0.27 \text{ \mu m}/\text{min} * 120\% = 330\text{s}$
 - Wafer removing
 - Tool: Vacuum hotplate @ 80°C
 - Time: 30s
 - Wafer cleaning
 - Acetone and IPA clean Santovac 5
 - SPR 2000, 15mins, DI rinsed 4 cycles, plasma stripper clean @ 150°C 3 mins
 - Inspection & comments
 - Check etched etch slots under microscope. Fully etched holes look clear. Otherwise, remaining oxide will show light red or blue based on the remaining thickness. Then, more time should be added to run another etch process.
 - Over etch may damage the edge of sacrificial layer where PR may be thinner than elsewhere

80.35 Dicing

Date:

- Wafer IDs:
- Tool: ADT 7100 Dicing Saw
- Recipe: Si dicing
 - Mount wafer to carrier wafer first, using wax (for CMP)
 - Mount wafer to blue tape at 60°C
 - Cut into dies
- Inspection & comments

80.40 XeF₂ etch

Date:

- Wafer IDs:
- Tool: STS Xactix
- Recipe: 30 sec etch, 3 Torr XeF₂ pressure, 0 Torr N₂ pressure
- Etch cycle: ≈ 10
- Etch rate: 2–3 $\mu\text{m}/\text{s}$
- Inspection & comments:

80.50 PECVD 2nd nitride

Date:

- Wafer IDs:
- Tool: GSI PECVD
- Recipe: Custom low stress Nitride 330
 - Temp- 330°C _SiH₄-40sccm_NH₃_35sccm
- Thickness: 20,000–70,000 \AA (depends on designs)
- Measure thickness and stress
 - Refer to the monitor wafer
- Inspection & comments:

- Check sealing under SEM, if not sealed (gap >200nm), then more PECVD nitride may be needed.

80.60 ALD Al₂O₃ sealing

Date:

- Wafer IDs:
- Preparation: tape dies using Kapton tape on four sides, preventing backside deposition
- Tool: Oxford ALD
- Recipe: 150°C Al₂O₃ water
- Deposition Cycle: 1000
- Thickness: 100 nm
- Measure thickness and stress
 - Refer to the monitor wafer
- Inspection & comments:

APPENDIX D:

Process Characterization

This appendix provides further information on process characterization of selected fabrication steps for the second generation microdischarge-based pressure sensor described in chapter 3. Specific topics include stress tuning of the sacrificial layer and the diaphragm layer, control of the sloped sidewall profile of the sacrificial layer, and characterization of the image reversal lithography for metallization steps.

D.1. PECVD α -Si as Sacrificial Layer

The standard PECVD α -Si process on the tool GSI PECVD is characterized for the deposition of films with thickness up to $\approx 1,000$ Å. The residual stress, which is ≈ -900 MPa (compressive) in such films, is usually not a major concern. However, the second generation microdischarge-based pressure sensor requires a much thicker α -Si (3 μm) as the sacrificial layer. When the film is thick, the large residual stress can bend the wafer significantly and may even result in cracking of the film after deposition. This makes it impossible to use the standard process recipe to obtain the target thickness. Therefore, a well characterized low stress recipe is required.

In this effort, a deposited α -Si film with low tensile stress (≈ 80 MPa) was obtained by tuning the SiH_4 flow, RF power, deposition temperature, and pressure (Figure D.1). It is worth noting that the process conditions and results can drift over time, and performing a test run before the real process is necessary.

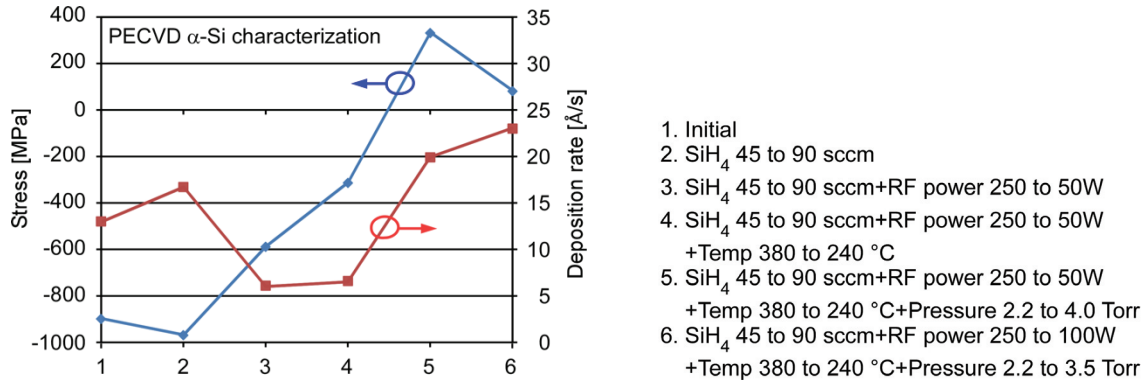


Figure D.1: Process characterization of the residual stress in PECVD α -Si.

D.2. Isotropic RIE α -Si Sacrificial Layer

Initially the α -Si layer was etched using the DRIE tool STS Pegasus because it provided a high α -Si to photoresist etch selectivity and a fast etch rate ($\approx 4.5 \mu\text{m}/\text{min}$). However, the sidewall of the etch profile (Figure D.2a) was almost vertical, which was not desirable for several reasons. First, the vertical sidewall may cause a disconnection problem for the metal feature across the sacrificial layer due to limited coverage on the sidewall during metal deposition. Second, the vertical sidewall tends to accumulate more photoresist at the bottom corner, which may also lead to the disconnection problem after the lift-off step and removal of undeveloped residual photoresist. Third, the vertical sidewall profile of the sacrificial layer directly leads to a vertical diaphragm sidewall, which is not desired for the device operation. A smoother transition at the corner from a sloped diaphragm sidewall would potentially reduce local stress concentration and avoid unnecessary crack or failure when the diaphragm is deformed during operation. Therefore, a sloped sidewall profile of the patterned sacrificial layer is desired.

For the RIE of silicon, F_2 generally results in a rough and pitted surface, and thus it is normally not directly used as a feedstock. Instead, common feedstock gases include CF_4 , SF_6 , and NF_3 , along with lower F composition (F/C) feedstock additions such as C_2F_6 [Lie05]. For a parallel plate RIE system with SF_6/O_2 gas mixture, it is found that the $O_2/(SF_6+O_2)$ gas flow ratio, chamber pressure, and electrode bias can affect both the sidewall profile and the etch rate [Fig05]. Particularly, the $O_2/(SF_6+O_2)$ ratio is the key parameter in determining the sidewall slope. To be specific, increasing the O_2 concentration can increase the sidewall slope, whereas the etch rate first increases and then decreases with the O_2 concentration increases. This is because the fluorine atom (etching species) concentration in the plasma first increases until it reaches a maximum due to the increased O_2 , and then it decreases because of a growing $Si_xO_yF_z$ film (inhibitor) and F atom dilution. Besides the impact from the $O_2/(SF_6+O_2)$ ratio, increasing the chamber pressure can also increase the slope with a more isotropic etch, because a higher pressure decreases the mean free path of the ions in the plasma and results in a loss of ion directionality. Although the feedstock gases for the tool PlasmaTherm 790 being used in this work are CF_4/O_2 , the fundamental etch mechanism and the tuning strategies are similar.

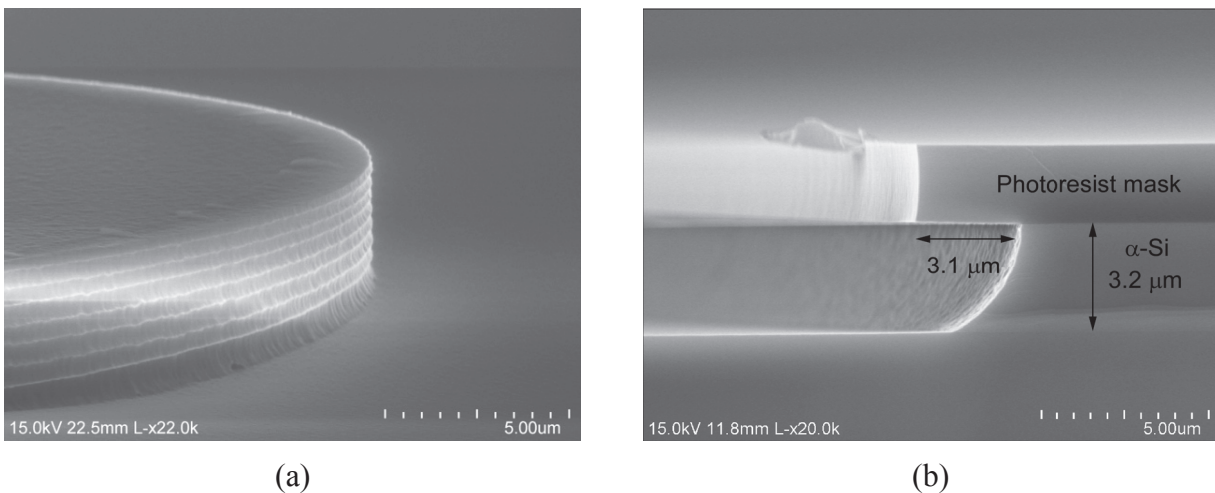


Figure D.2: Sidewall profiles of α -Si layer after RIE. (a) Initial profile with an anisotropic

etching by Pegasus. (b) A more isotropic profile, using the customized RIE.

The baseline parameters for the characterization were CF_4 40 sccm/ O_2 2 sccm, 80W and 100 mTorr. Because the CF_4/O_2 ratio appeared to be the most critical parameter for the sidewall slope according to the study of the SF_6/O_2 system, it was selected as the first tuning parameter in the experiment. For the CF_4/O_2 system, the maximum etch rate of silicon can be reached at 16% O_2 [Mog78]. However, with O_2 at this concentration, the etch rate of the photoresist mask was significantly increased. During the experiment, a 3.6 μm thick (of SPR 220 3.0) mask was completely etched before the process was finished. After a few characterization tests, the final parameters were selected at 10% O_2 (CF_4 42 sccm/ O_2 4.7 sccm), 150 mTorr and 80W. It was also found that the etch rate was load dependent and ranged from 60 nm/min to 100 nm/min. The final sidewall profile is shown in Figure D.2b, with an undercut that is similar to the thickness of the α -Si layer. It is noted that the undercut can result in shrinkage of the dimension from the targeted value, and a dimensional compensation is required in the layout design.

D.3. PECVD Silicon Nitride as Diaphragm Layer

The silicon nitride film for the diaphragm is also deposited by the tool GSI PECVD. The same stress issue as well as the similar characterization strategy applies to the PECVD nitride layer. The parameters in the baseline recipe include 380°C, SiH_4 99 sccm, NH_3 540 sccm, and 3.5 Torr. A number of experiments with modified parameters were performed, as summarized in Table D.1. The characterization was focused on tuning of the gas flow rates and the temperature, because the change of process pressure would adversely increase deposition non-uniformity and the change of RF power would have limited influence on the reduction of residual stress. In fact,

as it is known that “silicon rich” silicon nitride film would have lower stress, this work has primarily focused on the tuning of the flow rate ratio of SiH₄ to NH₃. As shown in Figure D.3, the residual stress of the PECVD nitride film reduces as the flow rate ratio of SiH₄ to NH₃ increases. However, when the ratio is increased over 0.35, the stability of deposition tends to be worse. With the consideration of both stress issue and repeatability, the final parameters were selected at 330°C and SiH₄/NH₃≈0.34 (SiH₄ 120 sccm, NH₃ 350 sccm). The average residual stress was about 130 MPa, with the deposition rate ≈30 Å/s.

As mentioned before, the process can drift over time and even from run to run, it is necessary to perform a test run before the real process to avoid any unnecessary deviation.

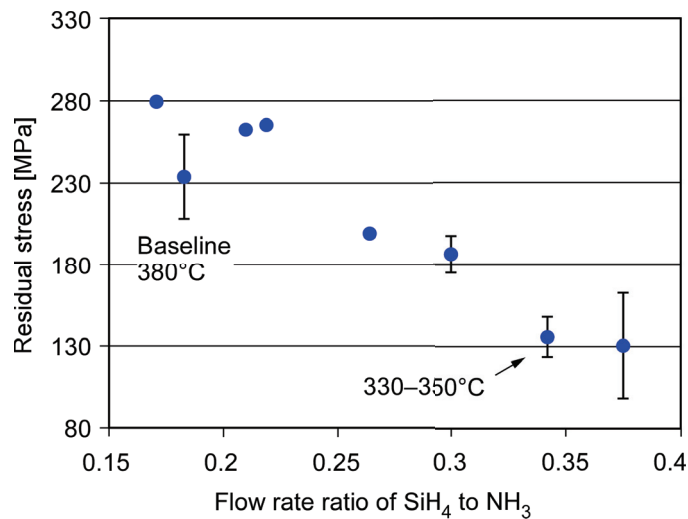


Figure D.3: Residual stress of PECVD nitride film against the flow rate ratio of SiH₄ to NH₃. Data points with no error bars indicate only one experiment was performed. The other data points are averaged values from ≈5 experiments. The deposition temperature was 380°C unless noted otherwise.

Table D.1: Experiments in characterization of PECVD nitride film stress.

Temp °C	SiH4 (%)	NH3 (%)	Pressure (Torr)	RF2 (W)	Dep. rate (Å/s)	Uniformity (%)	Stress (MPa)
	31	40	2.5		15.5	7.64	19
	31	52	3		18.8	6.05	-132
	31				19	1.3	279
380*	33	54	3.5	60	16.8	1.92	274
					19.3	1.86	204
					18.6	1.87	231
					16.3	4.02	225
		45			18.9	2.12	235
		45	3		17.1	6.44	366
	35	40			24.57	1.48	199
	38				17.1	1.78	262
		45	4		18.8	3.92	292
		45			17.6	1.95	210
		45		80	16	1.51	221
	50	40			35.3	1.97	91
	50	40			26.7	1.57	150
	50	40			22.9	1.93	175
	50	40			33.7	2.45	99
	50	40			23.9	1.73	159
	50	40			35.4	2.19	108
350	40	40			20.5	2.22	197
350	40	35			25.7	1.65	136
350	40	35			28.4	1.21	114
350	40	35			22.9	1.99	154
330	35	35			26.05	1.99	175
330	40	35			32.89	5.24	133
330	40	35			30.26	2.1	145
330	40	35			29.72	1.65	132

* Baseline (standard) recipe. Baseline parameters are not shown again in other results.

D.4. Image Reversal Lithography

Two metallization steps (bottom electrode and backside contacts) in the fabrication of the second generation microdischarge-based pressure sensor used image reversal (IR) lithography to

define the pattern. This was to obtain a negative sidewall profile in the developed photoresist to avoid unwanted residual metal sidewall or spikes after the lift-off step. The sidewall profile of the developed photoresist using IR lithography was characterized with respect to the exposure intensity. In the characterization, the photoresist SPR 220 3.0 was used. Detailed steps are provided in Table D.2.

Table D.2: Process steps of IR lithography characterization.

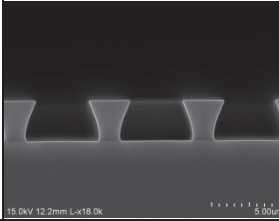
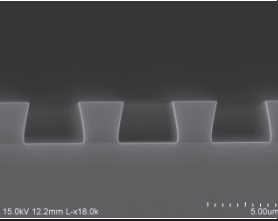
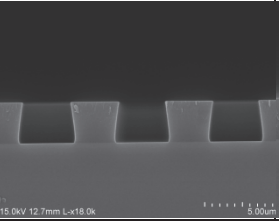
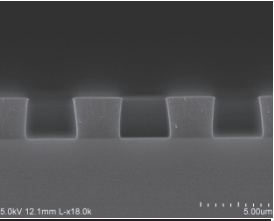
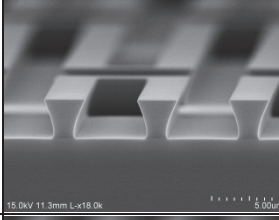
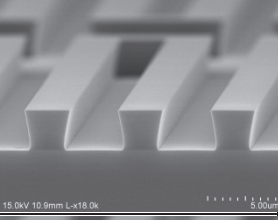
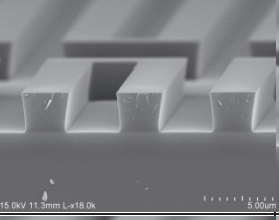
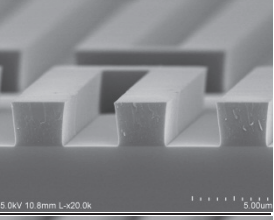
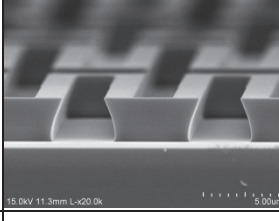
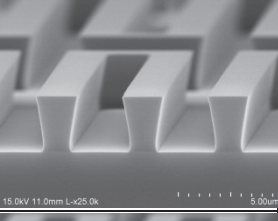
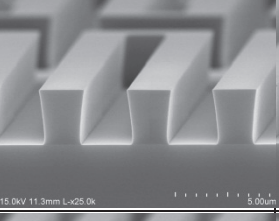
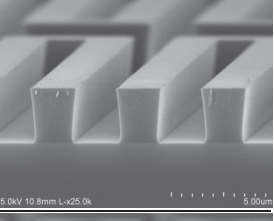
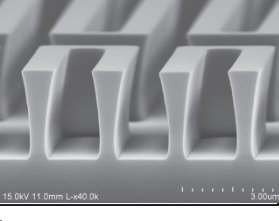
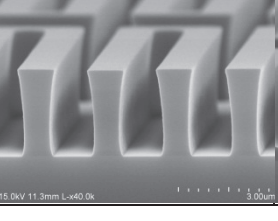
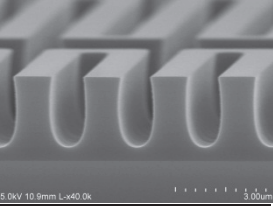
Steps	Tools	Recipe and conditions
HMDS coating & PR spinning	ACS 200	SPR 220 3.0 3 μ m. Vapor prime 90 °C, spin 3000 rpm
Soft bake	ACS 200	115 °C, 90s
First exposure	Stepper	Exposure matrix, from 0.05s to 0.52s, interval 0.01s
First post bake	ACS 200	115 °C, 90s; after exposure, wait for 10mins
Image reversal	IR oven	Recipe 2. 2700s in anhydrous ammonia gas at 90°C
Flood exposure	MA6	Lamp test button, 14s
Second post bake	ACS 200	115 °C, 90s; after flood exposure, wait for 10mins
Develop	ACS 200	AZ-300 MIF, 30s
SEM	SEM	Metal coating 10–15 nm

Notes: (1) A certain delay period before the post bakes may be required, especially for thick films, to outgas N₂. Otherwise, the N₂ will expand and increase the mechanical stress in the film; it will outgas during the bake process and destroy the resist profile. (2) The first exposure time and dose listed in this table is based on GCA AS200 AutoStep, which is a 5 \times reduction, i-line, step-and-repeat exposure tool used for patterning photoresist coated wafers. The light intensity for the GCA stepper is 300 mW/cm² at 365 nm. Although the stepper is calibrated at i-line, there are other wavelengths transmitted, just like the contact aligners. Therefore, the actual intensity as well as the total dose is higher than the listed value. (3) The flood exposure is performed using MA6 Mask Aligner. The light source is a 350 W multi-wavelength mercury UV arc lamp and is calibrated at 20 mW/cm² measured h-Line (405nm). Note that the lamp emits power at multiple wavelengths, thus exposure dose is not solely from the 20 mW/cm² output at h-Line. A very close estimate can be obtained by assuming about half as much i-Line (365nm) is added to h-Line dose. For this tool, a very close estimate would be 30 mW/cm² or 30 mJ/s.

Grating features with dimensions of 1 μ m, 2 μ m and 3 μ m were tested (Table D.3). It was found that the sidewall profile of the developed photoresist after IR lithography depended on the intensity of the first exposure. Less dose of the first exposure resulted in larger undercuts (Figure D.4a) and smaller sidewall angles (Figure D.4b). In addition, dimensions of slot features

were also enlarged. For example, the 3- μm wide slots were widened from 3 μm to $\approx 3.6 \mu\text{m}$ when the first exposure time decreased from 0.5s to 0.2s using the lithography tool GCA AS200 AutoStep (Figure D.4b). It was also noted that the sidewall was curved at the bottom. Therefore the maximum undercut was not located at the bottom of the slot features, as indicated in Figure D.4a.

Table D.3: Characterization results of IR lithography from grating features with dimensions from 1 μm to 3 μm .

1st exp.	0.2s (60 mJ/cm ²)	0.3s * (90 mJ/cm ²)	0.4s (120 mJ/cm ²)	0.5s (150 mJ/cm ²)
3 μm grating feature				
3 μm grating feature				
2 μm grating feature				
1 μm grating feature	N/A**			

* Normal exposure time is 0.32s.

** No remaining photoresist pattern exists at this condition for the 1- μm grating feature.

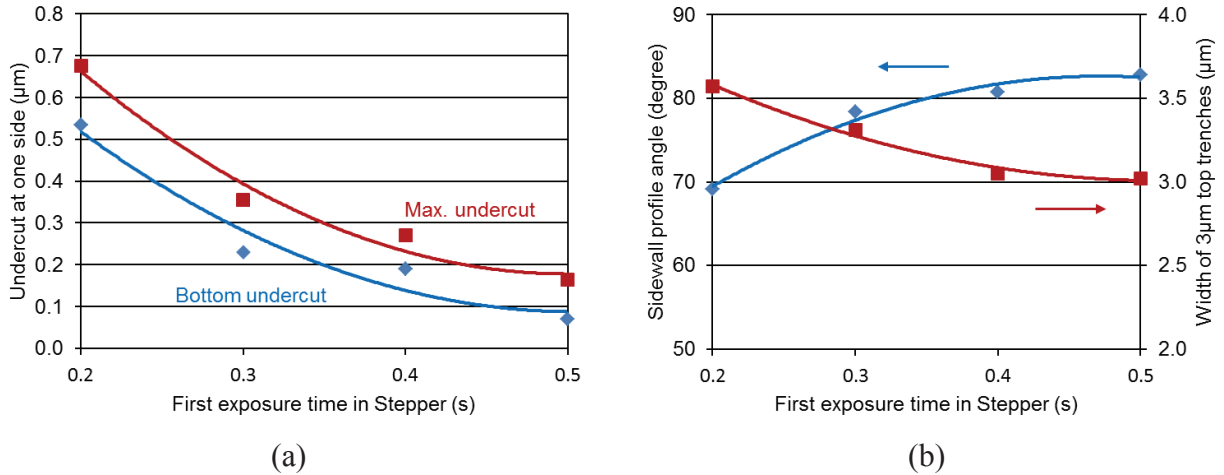


Figure D.4: (a) Undercut at one side, and (b) PR sidewall angle and width of 3 μm open features with increasing the does of first exposure.

For the metallization steps using the lift-off process, a smaller recessed sidewall angle or a larger undercut is desired to avoid unwanted residual metal sidewall or spikes. According to the characterization results, the first exposure with a normal dose (0.32s) can provide a good PR profile for the lift-off if the metal is deposited by evaporation (a more directional method); whereas less dose of the first exposure is highly recommended if sputtering is used to deposit the metal.

REFERENCES

- [Abe02] D. C. Abeysinghe, S. Dasgupta, H. E. Jackson, and J. T. Boyd, "Novel MEMS pressure and temperature sensors fabricated on optical fibers," *Journal of Micromechanics and Microengineering*, vol. 12, no. 3, pp. 229–235, Mar. 2002.
- [Aka01] O. Akar, T. Akin, and K. Najafi, "A wireless batch sealed absolute capacitive pressure sensor," *Sensors and Actuators a-Physical*, vol. 95, pp. 29-38, Dec 15 2001.
- [Akt09] E. E. Aktakka, H. Kim, and K. Najafi, "Wafer level fabrication of high performance MEMS using bonded and thinned bulk piezoelectric substrates," *IEEE International Conference on Solid-State Sensors, Actuators and Microsystems (Transducers)*, pp. 849-852, 21-25 June 2009.
- [Akt11] E. E. Aktakka, R. L. Peterson, and K. Najafi, "Thinned-PZT on SOI process and design optimization for piezoelectric inertial energy harvesting," in *Solid-State Sensors, Actuators and Microsystems Conference (Transducers), 2011 16th International*, 2011, pp. 1649-1652.
- [An13] S. An, N. Gupta, and Y. Gianchandani, "Vacuum sealing using atomic layer deposition of Al_2O_3 at 250°C ," *Journal of Vacuum Science & Technology A*, vol. 32, no. 1, pp. 01A101, Sep. 2013.
- [An14] S. An, N. K. Gupta, and Y. B. Gianchandani, "A Si-micromachined 162-stage two-part knudsen pump for on-chip vacuum," *Journal of Microelectromechanical Systems*, vol. 23, no. 2, pp. 406–416, Apr. 2014.
- [Ant81] T. R. Anthony, "Forming electrical interconnections through semiconductor wafers," *Journal of Applied Physics*, vol. 52, no. 8, pp. 5340–5349, Aug. 1981.
- [Ant07] S. R. Anton and H. A. Sodano, "A review of power harvesting using piezoelectric materials (2003-2006)," *Smart Materials & Structures*, vol. 16, pp. R1-R21, Jun 2007.
- [Ara08] S. Aravamudhan and S. Bhansali, "Reinforced piezoresistive pressure sensor for ocean depth measurements," *Sensors and Actuators a-Physical*, vol. 142, pp. 111-117, Mar 10 2008.
- [Ban06] A. Bansal, B. C. Paul, and K. Roy, "An analytical fringe capacitance model for interconnects using conformal mapping," *IEEE Transactions on Computer-Aided Design of Integrated Circuits and Systems*, vol. 25, pp. 2765-2774, Dec 2006.
- [Bar09] H. Bartzsch, D. Gloss, P. Frach, M. Gittner, E. Schultheiss, W. Brode, and J. Hartung, "Electrical insulation properties of sputter-deposited SiO_2 , Si_3N_4 and Al_2O_3 films at room

temperature and 400 degrees C," *Physica Status Solidi a-Applications and Materials Science*, vol. 206, pp. 514-519, Mar 2009.

[Ber59] D. Berlincourt and H. H. A. Krueger, "Domain Processes in Lead Titanate Zirconate and Barium Titanate Ceramics," *Journal of Applied Physics*, vol. 30, pp. 1804-1810, 1959.

[Ber92] D. Berlincourt, "Piezoelectric Ceramic Compositional Development," *Journal of the Acoustical Society of America*, vol. 91, pp. 3034-3040, May 1992.

[Cha87a] H. Chau, K. D. Wise, "Noise due to Brownian motion in ultrasensitive solid-state pressure sensors," *IEEE Transactions on Electron Devices*, vol. ED-34, no. 4, pp. 859-865, Apr. 1987.

[Cha87b] H. Chau, K. D. Wise, "Scaling limits in batch-fabricated silicon pressure sensors," *IEEE Transactions on Electron Devices*, vol. ED-34, no. 4, pp. 850-858, Apr. 1987.

[Cha01] A. V. Chavan and K. D. Wise, "Batch-processed vacuum-sealed capacitive pressure sensors," *Journal of Microelectromechanical Systems*, vol. 10, pp. 580-588, Dec 2001.

[Cho92] S. T. Cho, K. Najafi, C. E. Lowman, and K. D. Wise, "An ultrasensitive silicon pressure-based microflow sensor," *IEEE Transactions on Electron Devices*, vol. 39, no. 4, pp. 825-835, Apr. 1992.

[Dam96a] D. Damjanovic and M. Demartin, "The Rayleigh law in piezoelectric ceramics," *Journal of Physics D-Applied Physics*, vol. 29, pp. 2057-2060, Jul 14 1996.

[Dam96b] D. Damjanovic, M. Demartin, H. S. Shulman, M. Testorf, and N. Setter, "Instabilities in the piezoelectric properties of ferroelectric ceramics," *Sensors and Actuators A-Physical*, vol. 53, pp. 353-360, May 1996.

[Dam97a] D. Damjanovic, "Stress and frequency dependence of the direct piezoelectric effect in ferroelectric ceramics," *Journal of Applied Physics*, vol. 82, pp. 1788-1797, Aug 15 1997.

[Dam97b] D. Damjanovic and M. Demartin, "Contribution of the irreversible displacement of domain walls to the piezoelectric effect in barium titanate and lead zirconate titanate ceramics," *Journal of Physics-Condensed Matter*, vol. 9, pp. 4943-4953, Jun 9 1997.

[Dem96] M. Demartin and D. Damjanovic, "Dependence of the direct piezoelectric effect in coarse and fine grain barium titanate ceramics on dynamic and static pressure," *Applied Physics Letters*, vol. 68, pp. 3046-3048, May 20 1996.

[Dha00] R. S. Dhariwal, J-M. Torres, and M. P. Y. Desmulliez, "Electric field breakdown at micrometer separations in air and nitrogen at atmospheric pressure," *IEE Proceedings: Science, Measurement and Technology*, vol. 147, no. 5, pp. 261-265, Sep. 2000.

[Eij00] J. C. T. Eijkel, H. Stoeri, and A. Manz, "A dc microplasma on a chip employed as an optical emission detector for gas chromatography," *Analytical Chemistry*, vol. 72, pp. 2547-2552, Jun 1 2000.

- [Eun12] C. K. Eun and Y. B. Gianchandani, "Microdischarge-Based Sensors and Actuators for Portable Microsystems: Selected Examples," *IEEE Journal of Quantum Electronics*, vol. 48, pp. 814-826, Jun 2012.
- [Eun14] C. Eun, X. Luo, J-C. Wang, Z. Xiong, M. Kushner, and Y. Gianchandani, "A Microdischarge-Based Monolithic Pressure Sensor," *Journal of Microelectromechanical Systems*, vol. 23, no. 6, pp. 1300–1310, Dec. 2014.
- [Fig05] R. Figueroa, S. Spiesshoefer, S. Burkett, and L. Schaper, "Control of sidewall slope in silicon vias using SF₆/O₂ plasma etching in a conventional reactive ion etching tool," *Journal of Vacuum Science & Technology B: Microelectronics and Nanometer Structures*, vol. 23, no. 5, pp. 2226-2231, 2005.
- [Foe06] R. Foest, M. Schmidt, and K. Becker, "Microplasmas, an emerging field of low-temperature plasma science and technology," *International Journal of Mass Spectrometry*, vol. 248, pp. 87–102, Feb 15 2006.
- [Gad06] M. Gad-el-Hak, "The MEMS Handbook, CRC," ed: Taylor & Francis: Florida, 2006.
- [Gal11] T. Galchev, H. Kim, and K. Najafi, "Micro Power Generator for Harvesting Low-Frequency and Nonperiodic Vibrations," *Journal of Microelectromechanical Systems*, vol. 20, pp. 852–866, Aug 2011.
- [Gay96] R. Gayet, C. Harel, T. Josso, and H. Jouin, "A simple model for cathodic electronic emission enhanced by low-energy ions in high-pressure arcs," *Journal of Physics D: Applied Physics*, vol. 29, no. 12, pp. 3063–3070, Dec. 1996.
- [Ger59] L. H. Germer, "Electrical breakdown between close electrodes in air," *Journal of Applied Physics*, vol. 10, no. 1, pp. 46–51, Jan. 1959.
- [Gia06] Y. B. Gianchandani, C. Wilson, and J-S. Park, "Micromachined Pressure Sensors: Devices, Interface Circuits, and Performance Limits," in *The MEMS Handbook*, ed: M. Gad-el-Hak, CRC Press, 2006, pp. 3.1–3.44.
- [Gia83] J. M. Giachino, R. J. Haeberle, and J. W. Crow, "Method for manufacturing variable capacitance pressure transducers," U. S. Patent 4,386,453, Jun. 7, 1983.
- [Go10] D. B. Go and D. A. Pohlman, "A mathematical model of the modified Paschen's curve for breakdown in microscale gaps," *Journal of Applied Physics*, vol. 107, pp. 103303-(1–9), May 2010.
- [Gu09] C. D. Gu, H. Xu, and T. Y. Zhang, "Fabrication of high aspect ratio through-wafer copper interconnects by reverse pulse electroplating," *Journal of Micromechanics and Microengineering*, vol. 19, Jun 2009.
- [Gue12] R. Gueye, T. Akiyama, D. Briand, and N. de Rooij, "Fabrication and formation of Ta/Pt-Si ohmic contacts applied to high-temperature Through Silicon Vias (TSVs)," *Sensors and Actuators A: Physical*, 2012.

- [Guo00] S. Guo, J. Guo, and W. H. Ko, "A monolithically integrated surface micromachined touch mode capacitive pressure sensor," *Sensors and Actuators A: Physical*, vol. 80, no. 3, pp. 224–232, Mar. 2000.
- [Guo08] S. Guo, H. Eriksen, K. Childress, A. Fink, and M. Hoffman, "High temperature high accuracy piezoresistive pressure sensor based on smart-cut SOI," *Proc. IEEE Int. Conf. Micro Electro Mech. Syst.*, Tucson, AZ, 2008, pp. 892–895.
- [Hal01] D. A. Hall, "Review nonlinearity in piezoelectric ceramics," *Journal of Materials Science*, vol. 36, pp. 4575–4601, 2001.
- [He07] F. He, Q. Huang, and M. Qin, "A silicon directly bonded capacitive absolute pressure sensor," *Sensors and Actuators A: Physical*, vol. 135, no. 2, pp. 507–514, Apr. 2007.
- [Hou06] E. Hourdakis, G. W. Bryant, and N. M. Zimmerman, "Electrical breakdown in the microscale: testing the standard theory," *Journal of Applied Physics*, vol. 100, pp. 123306-(1–6), Dec. 2006.
- [How76] A. M. Howatson, *An introduction to gas discharges*, Second ed.: Pergamon press Oxford, 1976.
- [Hua06] H. Huang, K. J. Winchester, A. Suvorova, B. R. Lawn, Y. Liu, X. Z. Hu, J. M. Dell, L. Faraone, "Effect of deposition conditions on mechanical properties of low-temperature PECVD silicon nitride films," *Material Science and Engineering A*, vol. 435–436, pp. 453–459, Nov. 2006.
- [Hua11] B. X. Huang, C. Y. Liu, J. H. Fu, and H. Guan, "Hydraulic fracturing after water pressure control blasting for increased fracturing," *International Journal of Rock Mechanics and Mining Sciences*, vol. 48, pp. 976–983, Sep 2011.
- [Hun72] F B. Hunt, "Propagation of sound in fluids," *American Institute of Physics Handbook*, 3rd ed. New York: McGraw-Hill, 1972, pp. 3–67.
- [Jos98] T. Josso, H. Jouin, C. Harel, and R. Gayet, "Enhancement of cathodic electronic emission by slow positive ions in high-pressure arcs," *Journal of Physics D: Applied Physics*, vol. 31, no. 8, pp. 996–1008, Apr. 1998.
- [Kar04] V. Karanassios, "Microplasmas for chemical analysis: analytical tools or research toys?," *Spectrochimica Acta Part B-Atomic Spectroscopy*, vol. 59, pp. 909–928, Jul 30 2004.
- [Kim03] D-J. Kim, J.-P. Maria, A. I. Kingon, and S. K. Streiffer, "Evaluation of intrinsic and extrinsic contributions to the piezoelectric properties of $\text{Pb}(\text{Zr}_{1-X}\text{T}_X)\text{O}_3$ thin films as a function of composition," *Journal of Applied Physics*, vol. 93, pp. 5568–5575, 2003.
- [Kob10] T. Kobayashi, H. Okada, T. Masuda, R. Maeda, and T. Itoh, "A Digital Output Piezoelectric Accelerometer Using a $\text{Pb}(\text{Zr}, \text{Ti})\text{O}_3$ Thin Film Array Electrically Connected in Series," *Smart Materials and Structures*, vol. 19, Oct 2010.

- [Koy09] M. Koyanagi, T. Fukushima, and T. Tanaka, "High-density through silicon vias for 3-D LSI," *Proceedings of the IEEE*, vol. 97, no. 1, pp. 49–59, Jan. 2009.
- [Kue08] I. Kuehne, D. Marinkovic, G. Eckstein, and H. Seidel, "A new approach for MEMS power generation based on a piezoelectric diaphragm," *Sensors and Actuators A-Physical*, vol. 142, pp. 292-297, Mar 10 2008.
- [Kus05] M. J. Kushner, "Modelling of microdischarge devices: plasma and gas dynamics," *Journal of Physics D-Applied Physics*, vol. 38, pp. 1633-1643, Jun 7 2005.
- [Kym98] J. Kymissis, C. Kendall, J. Paradiso, and N. Gershenfeld, "Parasitic power harvesting in shoes," *Second International Symposium on Wearable Computers - Digest of Papers*, pp. 132-139, 1998.
- [Lae96] F. Laermer and A. Schilp, "Method of anisotropically etching silicon," U.S. Patent 5,501,893, Mar. 26, 1996.
- [Lee93] C. C. Lee, C. Y. Wang, and G. Matijasevic, "Au-in Bonding Below the Eutectic Temperature," *IEEE Transactions on Components Hybrids and Manufacturing Technology*, vol. 16, pp. 311-316, May 1993.
- [Lee05] C. S. Lee, J. Joo, S. Han, J. H. Lee, and S. K. Koh, "Poly (vinylidene fluoride) transducers with highly conducting poly (3,4-ethylenedioxythiophene) electrodes," *Synthetic Metals*, vol. 152, pp. 49-52, Sep 20 2005.
- [Lee09] S. Lee, B. D. Youn, and B. C. Jung, "Robust segment-type energy harvester and its application to a wireless sensor," *Smart Materials & Structures*, vol. 18, Sep 2009.
- [Lel06] E. S. Leland and P. K. Wright, "Resonance tuning of piezoelectric vibration energy scavenging generators using compressive axial preload," *Smart Materials & Structures*, vol. 15, pp. 1413-1420, Oct 2006.
- [Li02] X. G. Li, T. Abe, Y. X. Liu, and M. Esashi, "Fabrication of high-density electrical feed-throughs by deep-reactive-ion etching of Pyrex glass," *Journal of Microelectromechanical Systems*, vol. 11, pp. 625-630, Dec 2002.
- [Li06] T. Li and Y. B. Gianchandani, "A micromachining process for die-scale pattern transfer in ceramics and its application to bulk piezoelectric actuators," *Journal of Microelectromechanical Systems*, vol. 15, pp. 605-612, Jun 2006.
- [Li12] X. Li, Q. Liu, S. X. Pang, K. X. Xu, H. Tang, and C. S. Sun, "High-temperature piezoresistive pressure sensor based on implantation of oxygen into silicon wafer," *Sensors and Actuators a-Physical*, vol. 179, pp. 277-282, Jun 2012.
- [Lie05] M. A. Lieberman and A. J. Lichtenberg, *Principles of Plasma Discharges and Materials Processing, 2nd Edition*, 2005.

- [Luo11] X. Luo, W. Zhu, B. Mitra, J. Liu, T. Liu, X. Fan, and Y. B. Gianchandani, "A Chemical Detector for Gas Chromatography Using Pulsed Discharge Emission Spectroscopy on a Microchip," *American Geophysical Union, Fall Meeting*, Dec. 2011.
- [Luo12] X. Luo and Y. B. Gianchandani, "A High Voltage Generator Utilizing a Single PZT Element with Series-Connected Electrodes," in *Proc. of IEEE Sensors*, Taipei, Oct. 2012, pp. 993-996.
- [Luo13] X. Luo, Y. Gianchandani, "A Pulsed High-Voltage Generator Utilizing a Monolithic PZT Element and Evaluation of Nonlinear Piezoelectric Behavior in Transient Mode," *Journal of Microelectromechanical System*, vol. 22, no. 4, pp. 930–937, Aug. 2013.
- [Luo14] X. Luo, C. K. Eun, and Y. B. Gianchandani, "Fabrication of a monolithic microdischarge-based pressure sensor for harsh environments," *IEEE/ASME International Conference on Micro Electro Mechanical Systems (MEMS '14)*, San Francisco, Jan. 2014.
- [Ma14] Y. Ma, Y. Sui, T. Li, and Y. B. Gianchandani, "A submillimeter package for microsystems in high-pressure and high-salinity downhole environments," *Journal of Microelectromechanical Systems*, pp. 1–9, Sep. 2014.
- [Mas96] C. H. Mastrangelo, X. Zhang, and W. C. Tang, "Surface-micromachined capacitive differential pressure sensor with lithographically defined silicon diaphragm," *Journal of Microelectromechanical Systems*, vol. 5, no. 2, pp. 98-105, June 1996.
- [Mel52] R. H. Mellen, "The thermal-noise limit in the detection of underwater acoustic signals," *Journal of the Acoustical Society of America*, vol. 24, no. 5, pp. 478–480, Sep. 1952.
- [Mel01] P. Melvas, E. Kalvesten, and G. Stemme, "A surface-micromachined resonant-beam pressure-sensing structure," *Journal of Microelectromechanical Systems*, vol. 10, no. 4, pp. 498–502, Dec. 2001.
- [Mit08a] B. Mitra and Y. B. Gianchandani, "The detection of chemical vapors in air using optical emission spectroscopy of pulsed microdischarges from two- and three-electrode microstructures," *IEEE Sensors Journal*, vol. 8, pp. 1445-1454, Jul-Aug 2008.
- [Mit08b] B. Mitra, B. Levey, and Y. B. Gianchandani, "Hybrid arc/glow microdischarges at atmospheric pressure and their use in portable systems for liquid and gas sensing," *IEEE Transactions on Plasma Science*, vol. 36, pp. 1913-1924, Aug 2008.
- [Mog78] C. J. Mogab, A. C. Adams, and D. L. Flamm, "Plasma etching of Si and SiO₂ – the effect of oxygen additions to CF₄ plasmas," *Journal of Applied Physics*, vol. 49, no. 7, pp. 3796–3803, July 1978.
- [Moh03] F. Mohammadi, A. Khan, and R. B. Cass, "Power generation from piezoelectric lead zirconate titanate fiber composites," *Electronics on Unconventional Substrates-Electrotextiles and Giant-Area Flexible Circuits*, vol. 736, pp. 263-268, 2003.

- [Mor05] M. Morozov, D. Damjanovic, and N. Setter, "The nonlinearity and subswitching hysteresis in hard and soft PZT," *Journal of the European Ceramic Society*, vol. 25, pp. 2483-2486, 2005.
- [Nah07] S. K. Nah and Z. W. Zhong, "A microgripper using piezoelectric actuation for micro-object manipulation," *Sensors and Actuators A-Physical*, vol. 133, pp. 218-224, Jan 8 2007.
- [Nar13] M. Narducci, L. Yu-Chia, W. Fang, and J. Tsai, "CMOS MEMS capacitive absolute pressure sensor," *Journal of Micromechanics and Microengineering*, vol. 23, no. 5, pp. 055007, May 2013.
- [Nas71] E. Nasser, *Fundamentals of Gaseous Ionization and Plasma Electronics*, New York: Wiley, 1971.
- [Ned98] A. Ned, R. Okojie, and A. Kurtz, "6H-SiC pressure sensor operation at 600 °C," *Proc. Int. High Temperature Electron. Conf.*, Albuquerque, NM, 1998, pp. 257–260.
- [Ngu02] N. T. Nguyen, E. Boellaard, N. P. Pham, V. G. Kutchoukov, G. Craciun, and P. M. Sarro, "Through-wafer copper electroplating for three-dimensional interconnects," *Journal of Micromechanics and Microengineering*, vol. 12, pp. 395-399, Jul 2002.
- [Ort10] M. P. Orthner, S. Buetefisch, J. Magda, L. W. Rieth, and F. Solzbacher, "Development, fabrication, and characterization of hydrogel based piezoresistive pressure sensors with perforated diaphragms," *Sensors and Actuators a-Physical*, vol. 161, pp. 29-38, Jun 2010.
- [Owe12] K. J. Owen, B. VanDerElzen, R.L. Peterson and K. Najafi, "High aspect ratio deep silicon etching," *IEEE/ASME International Conference on Micro Electro Mechanical Systems (MEMS '12)*, Paris, France, Jan. 2012, pp. 251–254.
- [Par03] J. Park, and Y. B. Gianchandani, "A servo-controlled capacitive pressure sensor using a capped-cylinder structure microfabricated by a three-mask process," *Journal of Microelectromechanical Systems*, vol. 12, no. 2, pp. 209–220, Apr. 2003.
- [Pea50] R. W. B. Pearse and A. G. Gaydon, *The identification of molecular spectra*: Chapman & Hall, 1950.
- [Per04] R. Perez, A. Albareda, J. E. Garcia, J. Tiana, E. Ringgaard, and W. W. Wolny, "Extrinsic contribution to the non-linearity in a PZT disc," *Journal of Physics D-Applied Physics*, vol. 37, pp. 2648-2654, Oct 7 2004.
- [Rie88] W. Riethmuller and W. Benecke, "Thermally excited silicon microactuators," *IEEE Trans. Electron Devices*, vol. 35, no. 6, pp. 758-762, June 1988.
- [Rou03] S. Roundy, P. K. Wright, and J. Rabaey, "A study of low level vibrations as a power source for wireless sensor nodes," *Computer Communications*, vol. 26, pp. 1131-1144, Jul 1 2003.

- [Sam73] Samaun, K. D. Wise, and J. B. Angell, "An IC piezoresistive pressure sensor for biomedical instrumentation," *IEEE Transaction on Biomedical Engineering*, vol. BME-20, no. 2, pp. 101–109, Mar. 1973.
- [Shi11] J. H. Shin, H. G. Moon, and S. E. Chae, "Effect of blast-induced vibration on existing tunnels in soft rocks," *Tunnelling and Underground Space Technology*, vol. 26, pp. 51-61, Jan 2011.
- [Sla02] P. G. Slade and E. D. Taylor, "Electrical breakdown in atmospheric air between closely spaced (0.2 μm –40 μm) electrical contacts," *IEEE Transactions on Components and Packaging Technologies*, vol. 25, no. 3, pp. 390–396, Sep. 2002.
- [So00] W. W. So and C. C. Lee, "Fluxless process of fabricating In-Au joints on copper substrates," *IEEE Transactions on Components and Packaging Technologies*, vol. 23, pp. 377-382, Jun 2000.
- [Soh07] Y. C. Sohn, Q. Wang, S. J. Ham, B. G. Jeong, K. D. Jung, M. S. Choi, W. B. Kim, and C. Y. Moon, "Wafer-level low temperature bonding with Au-In system," *57th Electronic Components and Technology Conference*, pp. 633-637, 2007.
- [Son08] C. S. Song, Z. Y. Wang, Q. W. Chen, J. Cai, and L. T. Liu, "High aspect ratio copper through-silicon-vias for 3D integration," *Microelectronic Engineering*, vol. 85, pp. 1952-1956, Oct 2008.
- [Son09] H. C. Song, H. C. Kim, C. Y. Kang, H. J. Kim, S. J. Yoon, and D. Y. Jeong, "Multilayer piezoelectric energy scavenger for large current generation," *Journal of Electroceramics*, vol. 23, pp. 301-304, Oct 2009.
- [Spa97] C. Spataru, D. Teillet-Billy, J. P. Gauyacq, P. Teste and J. P. Chabrierie, "Ion-assisted electron emission from a cathode in an electric arc," *Journal of Physics D: Applied Physics*, vol. 30, no. 7, pp. 1135–1145, Jan. 1997.
- [Spi05] S. Spiesshoefer, Z. Rahman, G. Vangara, S. Polamreddy, S. Burkett, and L. Schaper, "Process integration for thorough-silicon vias," *Journal of Vacuum Science & Technology A*, vol. 23, no. 4, pp. 824–829, 2005.
- [Str11] R. Straessle, Y. Petremand, D. Briand, and N. F. de Rooij, "Evaluation of Thin Film Indium Bonding at Wafer Level," *Eurosensors XXV*, vol. 25, 2011.
- [Suk12] V. Sukumaran, T. Bandyopadhyay, V. Sundaram, and R. Tummala, "Low-Cost Thin Glass Interposers as a Superior Alternative to Silicon and Organic Interposers for Packaging of 3-D ICs," *IEEE Transactions on Components Packaging and Manufacturing Technology*, vol. 2, pp. 1426-1433, Sep 2012.
- [Sum07] H. Sumali, J. E. Massad, D. A. Czaplewski, and C. W. Dyck, "Waveform design for pulse-and-hold electrostatic actuation in MEMS," *Sensors and Actuators A-Physical*, vol. 134, pp. 213-220, Feb 28 2007.

- [Tam72] M. Tamura and H. Sunami, "Generation of dislocations induced by chemical vapor deposited Si₃N₄ films on silicon," *Japan J. Appl. Phys.*, vol. 11, no. 8, pp. 1097-1105, Aug. 1972.
- [Tay97] J. R. Taylor, "Propagation of uncertainties," in *An introduction to error analysis: the study of uncertainties in physical measurements*, 2nd ed. Sausalito, CA: University Science Books, 1997, ch. 3, pp. 45–92.
- [Tow15] J. Townsend, *Electricity in Gases*, Oxford, England: Oxford University Press, 1915.
- [Tes96] P. Teste and J-P. Chabrierie, "Some improvements concerning the modeling of the cathodic zone of an electric arc (ion incidence on electron emission and the 'cooling effect')," *Journal of Physics D: Applied physics*, vol. 29, no. 3, pp. 697–705, Mar. 1996.
- [Wal03] A. Wallsh and L. Levit, "Electrical breakdown and ESD phenomena for devices with nanometer-to-micro gaps," *Proceedings of SPIE, Reliability, Testing, and Characterization of MEMS/MOEMS II*, vol. 4980, pp. 87–96, Jan. 2003.
- [Wan97] Y. Wang, and M. Esashi, "A novel electrostatic servo capacitive vacuum sensor," *International Conference on Solid-State Sensors, Actuators, and Microsystems (Transducers)*, Chicago, June 1997, pp. 1457–1460.
- [Wan99] Q. Wang and W. H. Ko, "Modeling of touch mode capacitive sensors and diaphragms," *Sensors and Actuators A: Physical*, vol. 75, no. 3, pp. 230–241, June 1999.
- [Wik09] Wikipedia, "Electric glow discharge schematic," [Online]. Available: http://en.wikipedia.org/wiki/File:Electric_glow_discharge_schematic.png, accessed Apr. 2, 2015.
- [Wil02] C. G. Wilson and Y. B. Gianchandani, "Spectral detection of metal contaminants in water using an on-chip microglow discharge," *IEEE Transactions on Electron Devices*, vol. 49, pp. 2317-2322, Dec 2002.
- [Wil03] C. G. Wilson, Y. B. Gianchandani, R. R. Arslanbekov, V. Kolobov, and A. E. Wendt, "Profiling and modeling of dc nitrogen microplasmas," *Journal of Applied Physics*, vol. 94, pp. 2845-2851, Sep 1 2003.
- [Wri09a] S. A. Wright and Y. B. Gianchandani, "Discharge-Based Pressure Sensors for High-Temperature Applications Using Three-Dimensional and Planar Microstructures," *Journal of Microelectromechanical Systems*, vol. 18, pp. 736-743, Jun 2009.
- [Wri09b] S. A. Wright and Y. B. Gianchandani, "Contaminant gas removal using thin-film Ti electrode microdischarges," *Applied Physics Letters*, vol. 95, Sep 14 2009.
- [Wri13] S. A. Wright, H. Z. Harvey, and Y. B. Gianchandani, "A Microdischarge-Based Deflecting-Cathode Pressure Sensor in a Ceramic Package," *Journal of Microelectromechanical Systems*, vol. 22, pp. 80-86, 2013.

[Yol14] Yole Développement. (2014, July 30). "Status of MEMS industry 2014," [Online]. Available: <http://www.i-micronews.com/mems-sensors-report/product/status-of-the-mems-industry-2014.html>, accessed Jan. 20, 2015.

[You04] D. J. Young, J. G. Du, C. A. Zorman, and W. H. Ko, "High-temperature single-crystal 3C-SiC capacitive pressure sensor," *IEEE Sensors Journal*, vol. 4, pp. 464-470, Aug 2004.

[Zho05] M. X. Zhou, Q. A. Huang, M. Qin, and W. Zhou, "A novel capacitive pressure sensor based on sandwich structures," *Journal of Microelectromechanical Systems*, vol. 14, pp. 1272-1282, Dec 2005.

[Zha12] J. H. Zhao, X. J. Zheng, L. Zhou, Y. Zhang, J. Sun, W. J. Dong, S. F. Deng, and S. T. Peng, "Investigation of a d(15) mode PZT-51 piezoelectric energy harvester with a series connection structure," *Smart Materials and Structures*, vol. 21, Oct 2012.